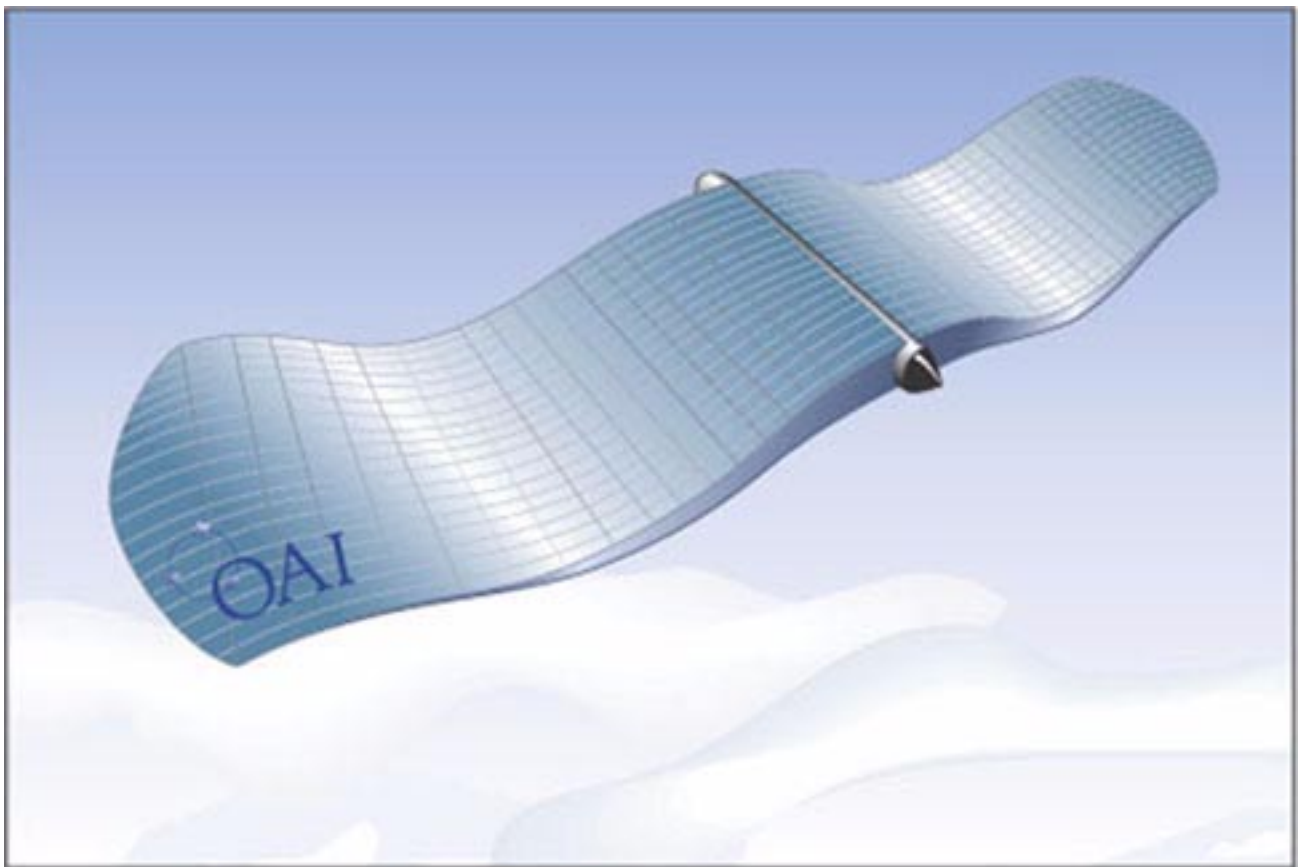


Solid State Aircraft

Phase I Project NAS5-98051

Final Report



**Prepared for:
Robert A. Cassanova, Director
NASA Institute for Advanced Concepts**

November 30, 2002

Table of Contents

List of Tables	iii
List of Figures	v
List of Contributors	xi
Chapter 1.0 Introduction	1
1.1 Concept Description	1
1.2 Vehicle Operation	3
Chapter 2.0 Component Technologies	7
2.1 Solar Cell Technology	7
2.2 Energy Storage	7
2.3 IPMC Material	8
2.3.1 Ionic Polymer Metal Composites--In General	8
2.3.2 Manufacturing Techniques	12
2.3.3 Phenomenological Law	15
2.3.4 Characteristics	16
2.3.5 Cryogenic Properties of IPMC Artificial Muscles	26
2.3.6 Current-Voltage Data for IPMCs	30
Chapter 3.0 Aerodynamics	35
3.1 Introduction	35
3.2 CFD Calculations: WIND	37
Chapter 4.0 Environment	43
4.1 Proposed Operational Environments	43
4.2 Environmental Conditions for Flight on Venus	43
4.2.1 Physical Properties of Venus	46
4.2.2 Atmospheric Conditions of Venus	46
4.3 Environmental Conditions for Flight on Earth	51
4.3.1 Physical Properties of Earth	51
4.3.2 Atmospheric Conditions of Earth	52
4.3.3 Earth Standard Atmosphere	55
4.4 Environmental Conditions for Flight on Mars	58
4.4.1 Physical Properties on Mars	61
4.4.2 Atmospheric Conditions on Mars	61
4.4.3 Dust Storms and Wind	64
4.4.4 Mars Atmosphere Data	66
Chapter 5.0 Feasibility Analysis	81
5.1 Solar Array Power Production	81
5.2 Vehicle-Sizing Analysis	88
5.2.1 Airfoil Properties	88
5.2.2 Power and Energy Required	92
5.2.3 Lift Generation	98
5.2.4 Results	101
5.3 Example Design	111
Appendix A List of References	A-1

List of Tables

Table 2-1: Current capabilities of IPMC materials	23
Table 4-1: Physical properties of Venus	46
Table 4-2: Venus atmospheric composition	47
Table 4-3: Venus atmospheric properties with altitude	47
Table 4-4: Physical properties of Earth	51
Table 4-5: Major gas components of Earth's atmosphere	54
Table 4-6: Earth standard atmosphere	55
Table 4-7: Physical properties of Mars	61
Table 4-8: Mars atmospheric composition	61
Table 4-9: JPL reference Mars atmosphere for -20° latitude	66
Table 4-10: General Mars atmosphere model (NASA Langley)	68
Table 4-11: Mars-GRAM generated atmosphere profile for -25o latitude, 11o longitude	73
Table 4-12: Mars-GRAM generated atmosphere profile for 57o latitude, 2.35o longitude	75
Table 5-1: Solar array output parameters	81
Table 5-2: Analysis baseline assumptions	101
Table 5-3: Altitude ranges in which results were produced for the various planets	102

List of Figures

Figure 1-1: Solid State Aircraft (SSA) concept	1
Figure 1-2: Component layout of the SSA wing	2
Figure 1-3: Flap-to-glide cycle flight profile	3
Figure 1-4: Examples of flap-to-glide time ratios	4
Figure 1-5: Wing forces on upstroke and downstroke	4
Figure 1-6: Wing-control grid and material composition	5
Figure 2-1: Flexible amorphous silicon solar array	7
Figure 2-2: Successive photographs of an IPMC strip that shows very large deformation (up to 4 cm) in the presence of low voltage. Note that $Dt = 0.5$ sec, 2 V applied. The sample is 1 cm wide, 4 cm long, and 0.2 mm thick.	9
Figure 2-3: A typical sensing response of an IPMC. It shows dynamic sensing response of a strip of an IPMC (40 mm x 10 mm x 0.2 mm thickness) subject to a dynamic impact loading in a cantilever configuration. A damped electric response is highly repeatable with a high bandwidth of up to 100 Hz. Such direct mechano-electric behaviors are related to the endo-ionic mobility caused by imposed stresses. This implies that, if we impose a finite solvent (=water) flux, $ Q $, not allowing a current flux, $J=0$, a certain conjugate electric field, E , is produced that can be dynamically monitored, as discussed later in Section 2.3.3.	9
Figure 2-4: A mode of operation of IPMC in flapping and aerofoil gliding maneuvering configuration. Electrodes 175 and 180 can be further printed on the upper 170, 171, or lower 172 wing surfaces, while edges 173 and 174 can perform edge maneuvering and leads 180a and 181a power the wing through circuitry 191 and 192 and controlled switching 195 and oscillatory signal source 190.	10
Figure 2-5: IPMC strip in wing-flapping configuration	10
Figure 2-6: Perfluorinated sulfonic acid polymers	11
Figure 2-7: IPMC strip after being composited with metal electrodes	11
Figure 2-8: Typical amplitude of flapping under oscillatory voltage for small samples of 25.4 mm x 12.7 mm x 0.3mm, (top), 37.9 mm x 12.7 mm x 0.3 mm, (bottom)	12
Figure 2-9: Two schematic diagrams showing different preparation processes:	13
Figure 2-10: Two SEM micrographs (top) showing the cross-section (left) and close-up (right) of a typical IPMC. The bottom graph shows an x-ray line scan of Pt. As can be noticed, Pt is dense at the surface.	14
Figure 2-11: An atomic force microscopy (ATM) surface-analysis image taken on the surface electrode of a typical muscle as shown in Figure 2-5 (bottom-right). The scanned area is 1 mm ² . The brighter/darker area corresponds to a peak/valley depth of 50 nm. The surface-analysis image has a view angle set at 22°. Digital Instruments' AFM NanoScope IIIa was used. A tip (ultra levers) from Park Scientific Instrument was utilized in an air-contact mode under low voltage.	15
Figure 2-12: A TEM micrograph of the IPMC. It is on the penetrating edge of the IPMC. The sample was carefully prepared in a small piece and ion-beam treated.	15
Figure 2-13: A schematic of the typical IPMC artificial muscle and its actuation principle. ...	16
Figure 2-14: Tensile testing results	17
Figure 2-15: A cantilever configuration of the IPMC (a) and an illustration of positive/negative strains experienced in the operation mode of the IPMC. Bottom graphs show the ef-	

fect of swelling (c) and stiffening behavior under electric activation (d). Swelling is also an important parameter to affect the mechanical property. Indicatively speaking, swelling causes mechanical weakening. Electric activation has a tendency to stiffen the material due to redistributed ions within the IPMC. 19

Figure 2-16: The measured AC impedance characteristics of an IPMC sample (the wet IPMC sample is 5 mm x 20 mm x 0.2 mm) 20

Figure 2-17: A possible electric circuit equivalent to the typical IPMC (left) and measured surface resistance, R_s , as a function of platinum penetration depth (right). Note that SEM was used to estimate the penetration depth of platinum into the membrane. The four-probe method was used to measure the surface resistance, R_s , of the IPMCs. Obviously, the deeper the penetration, the lower the surface resistance. 20

Figure 2-18: I/V curves for a typical IPMC. (NafionTM-117-based IPMC) 21

Figure 2-19: Frequency dependency of the IPMC in terms of the normal stress, sN , vs. the normal strain, eN , under an imposed step voltage of 1 V. This NafionTM-117 IPMC has a cation of Li^+ and a size of 5 mm x 20 mm. 22

Figure 2-20: Longevity testing of flapping IPMC strips under 1 V square wave and 0.5 Hz. .. 22

Figure 2-21: Blocking forces measured at the tip of the IPMCs (sinusoidal input @ 0.5 Hz) .. 23

Figure 2-22: A blocking force measurement configuration for undulating IPMC fin actuators 23

Figure 2-23: Specific energy as a function of frequency for typical IPMC samples. The sample dimensions are 20 mm x 5 mm x 1.6 mm thickness. A maximum square-wave voltage input @ 16 V and Cation = Li^+ 24

Figure 2-24: Power output as a function of frequencies 25

Figure 2-25: Potentio-static coulometric analysis for the additive-treated IPMC and the conventional IPMC. This graph may be interpreted as a statement that an increased current passage (Faraday approach) can contribute the observed improvement in the force characteristics (see Figure 2-18) but not so significant meaning that larger contribution from sandbagging effect. 26

Figure 2-26: Deflection characteristics of IPMC as a function of time and temperature 27

Figure 2-27: Power consumption of the IPMC strip-bending actuator as a function of activation voltage 27

Figure 2-28: Deflection of the bending IPMC strip as a function of voltage 27

Figure 2-29: Deflection vs. power and current under a constant voltage of 3 V and a frequency of 0.1 Hz For two different pressures 28

Figure 2-30: Effect of temperature on electrical resistance. 28

Figure 2-31: Relationship between current and deflection for an IPMC strip exposed to room temperature and $-100^{\circ}C$ 29

Figure 2-32: Relationship between power and deflection for an IPMC strip exposed to room temperature and $-100^{\circ}C$ 29

Figure 2-33: Deflection and power consumption of the IPMC muscle as a function of temperature with pressure as a parameter, $V_{peak} = 3 V$, $Freq = 0.1 Hz$ 29

Figure 2-34: Schematic design of the I-V electrical measurement setup 30

Figure 2-35: Resulting data from typical I-V loops 30

Figure 2-36: Current response of typical IPMC membrane to a sinusoidal voltage of 2.2 V and 0.5 Hz 31

Figure 2-37: Current response of typical IPMC membrane to a square wave step voltage of 2.2 V and frequency of 0.5 Hz. 31

Figure 2-38: Variation of input power response of typical IPMC membranes to a sinusoidal voltage of 2.2 V and a frequency of 0.5 Hz 32

Figure 2-39: Current response of typical IPMC membrane to a sinusoidal voltage of 2.2 V and a frequency of 0.5 Hz 32

Figure 2-40: Current response of typical IPMC membrane to a square wave step voltage of 2.2 V and frequency of 0.5 Hz 33

Figure 2-41: Current response of typical IPMC muscles to a voltage of 2.2 V and a frequency of 0.5 Hz 33

Figure 3-1: NASA Pathfinder high altitude aircraft 35

Figure 3-2: Pterosaur 35

Figure 3-3: Wing planform of pterosaur and various aspect ratios of other birds. 36

Figure 3-4: Mach number contours around the Selig 1091 airfoil at Reynolds number 100,000, mach number 0.19, and 6° angle of attack 38

Figure 3-5: Status pressure contours around the Selig 1091 airfoil at Reynolds number 100,000, mach number 0.19, and 6° angle of attack 39

Figure 3-6: Lift coefficient vs. angle of attack for WIND and XFOIL computations 39

Figure 3-7: 299 x 100 grid used for the CFD calculations 40

Figure 3-8: Streamlines around the Selig 1091 airfoil at Reynolds number 100,000, mach number 0.19, and 18° angle of attack 41

Figure 3-9: Drag coefficient vs. angle of attack for WIND and XFOIL computations 42

Figure 4-1: Venus 43

Figure 4-2: Temperature profile of Venus’s atmosphere 44

Figure 4-3: Temperature profile within Venus’s atmosphere 45

Figure 4-4: Earth 51

Figure 4-5: Profile of Earth’s atmosphere 52

Figure 4-6: Troposphere 52

Figure 4-7: Mean wind speeds for Albuquerque, New Mexico 53

Figure 4-8: Mean wind speeds for Cape Kennedy, Florida 54

Figure 4-9: Mars 58

Figure 4-10: Image of Mars atmosphere taken from Pathfinder Lander 59

Figure 4-11: Orbital image of surface features on Mars 60

Figure 4-12: Image of Mars surface from Pathfinder Lander 60

Figure 4-13: Daily pressure variation (Pathfinder data) 63

Figure 4-14: Pressure variation over a one-month period (Pathfinder data) 63

Figure 4-15: Atmospheric temperature variation throughout a day (Pathfinder data) 64

Figure 4-16: Wind direction throughout the day (Pathfinder data) 65

Figure 4-17: Measurements taken during a dust devil (Pathfinder data) 66

Figure 5-1: Venus: Available power throughout a day at various latitudes 83

Figure 5-2: Earth: Available power throughout the day at 0° latitude 83

Figure 5-3: Earth: Available power throughout the day at 20° latitude 84

Figure 5-4: Earth: Available power throughout the day at 40° latitude 84

Figure 5-5: Earth: Available power throughout the day at 60° latitude 85

Figure 5-6: Earth: Available power throughout the day at 80° latitude 85

Figure 5-7: Mars: Available power throughout the day at 0° latitude 86

Figure 5-8: Mars: Available power throughout the day at 20° latitude 86

Figure 5-9: Mars: Available power throughout the day at 40° latitude 87

Figure 5-10: Mars: Available power throughout the day at 60° latitude	87
Figure 5-11: Mars: Available power throughout the day at 80° latitude	88
Figure 5-12: Cruise-flight speed as a function of atmospheric density	89
Figure 5-13: Cruise Reynolds number per chord length vs. atmospheric density	90
Figure 5-14: Lift coefficient vs. angle of attack for a curved flat plate at various low Reynolds numbers	90
Figure 5-15: Lift coefficient vs. drag coefficient for a curved flat plate at various low Reynolds numbers	91
Figure 5-16: Examples of potential flap/glide combinations	93
Figure 5-17: Wing motion and geometry	94
Figure 5-18: Force and mass distribution along a wing section (for a 5-m wingspan and 1 Hz flapping rate)	95
Figure 5-19: Acceleration force diagram	96
Figure 5-20: Force along the wing as a function of distance traveled by each segment of the wing section	97
Figure 5-21: Lift force generation due to flapping	99
Figure 5-22: Lift/glide cycle for the SSA operation	100
Figure 5-23: Lift force along the wing for various flap rates	101
Figure 5-24: Specific power vs. flap duration for a 3-m wingspan vehicle at various altitudes	103
Figure 5-25: Specific power vs. flap duration for a 6-m wingspan vehicle at various altitudes	103
Figure 5-26: Specific power vs. flap duration for a 12-m wingspan vehicle at various altitudes	104
Figure 5-27: Specific power vs. flap duration for a 25-m wingspan vehicle at various altitudes	104
Figure 5-28: Specific power vs. flap duration for a 50-m wingspan vehicle at various altitudes	105
Figure 5-29: Specific power vs. flap duration for a 100-m wingspan vehicle at various altitudes	105
Figure 5-30: Glide duration vs. flap duration for a 3-m wingspan vehicle at various altitudes	106
Figure 5-31: Glide duration vs. flap duration for a 6-m wingspan vehicle at various altitudes	106
Figure 5-32: Glide duration vs. flap duration for a 12-m wingspan vehicle at various altitudes	107
Figure 5-33: Glide duration vs. flap duration for a 25-m wingspan vehicle at various altitudes	107
Figure 5-34: Glide duration vs. flap duration for a 50-m wingspan vehicle at various altitudes	108
Figure 5-35: Glide duration vs. flap duration for a 100-m wingspan vehicle at various altitudes	108
Figure 5-36: Minimum required power for various altitude-wingspan combinations	109
Figure 5-37: Flap duration for minimum required power at various altitudes and wingspans	109
Figure 5-38: Glide duration for minimum required power at various altitudes	

and wingspans 110
Figure 5-39: Power required and maximum available power at each planetary location 111

List of Contributors

Northland Scientific

Mr. Anthony Colozza (PI)

OAI

Ms. Laurie Beringer

Ms. Terri Deacey

Mr. Phillip Jenkins

Mr. Franklin Porath

Mr. Curtis Smith

University of New Mexico

Dr. Mohsen Shahinpoor

Independent Consultants

Mr. Teryn DalBello

Abstract

A revolutionary type of unmanned aircraft may now be feasible, due to recent advances in polymers, photovoltaics (PV), and batteries. This aircraft is a “solid state” aircraft, with no conventional mechanical moving parts. Airfoil, propulsion, energy production, energy storage, and control are combined in an integrated structure for the first time.

The most innovative aspect of this concept is the use of an ionic polymeric metal composite (IPMC) as the source of control and propulsion. This material has the unique capability of deforming in an electric field like an artificial muscle and returning to its original shape when the field is removed. Combining the IPMC with emerging thin film batteries and thin film PVs provides both energy source and storage in the same structure.

Combining the unique characteristics of the materials enables flapping motion of the wing to be used to generate the main propulsive force. With a flight profile similar to that of a hawk or eagle, the Solid State Aircraft (SSA) will be able to soar for long periods of time and then flap to regain lost altitude. By analyzing the glide duration, flap duration, wing length, and wing motion of travel, it has been determined that a number of design configurations can enable flight over a range of latitudes and times of the year on Earth, Venus, and Mars.

Recent discoveries and developments in these materials have indicated that this concept, on a preliminary level, may provide a robust advanced aeronautical architecture suitable for both terrestrial and planetary missions.

Chapter 1.0 Introduction

1.1 Concept Description

Due to recent advancements in PVs, batteries, and polymer materials, a unique type of unmanned aircraft may be feasible. This aircraft is a “solid state” aircraft with no moving parts. An artist’s rendering of the concept is shown in Figure 1-1.

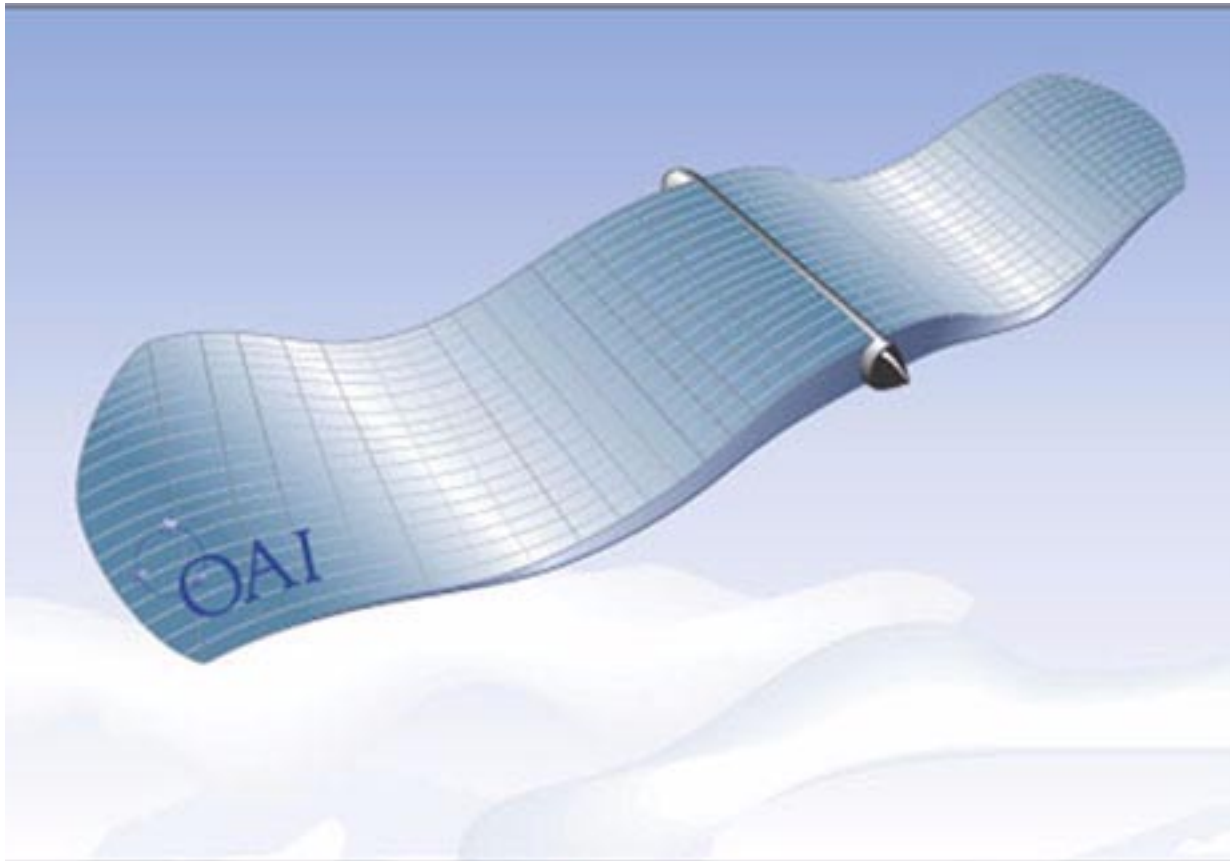


Figure 1-1: Solid State Aircraft (SSA) concept

Its unique structure combines aerodynamic lift, propulsion, energy collection, energy storage, and control. Thin film solar arrays collect sunlight and produce power that is stored in a thin film lithium battery. This power is used to fly the aircraft by setting up an electromagnetic field (EMF) along the wing of the vehicle. The wing, made with ionic polymeric metal composite (IPMC) synthetic muscles, bends in the presence of this EMF, producing the desired flapping motion. This layering of the various component materials is shown in Figure 1-2.

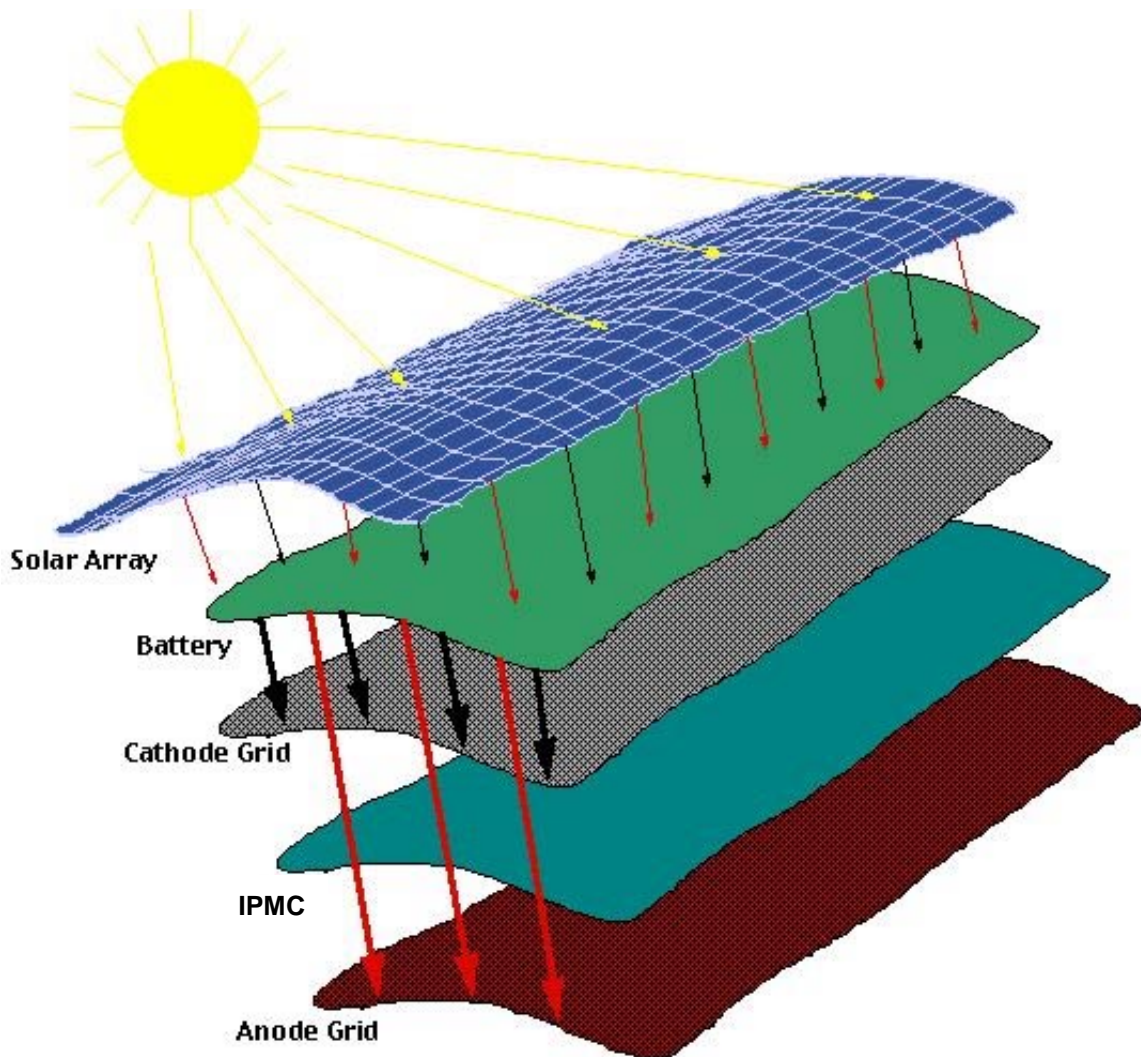


Figure 1-2: Component layout of the SSA wing

This aircraft would fly like a hawk or eagle, gliding for long distances and flapping infrequently to regain altitude. The solid state nature of the aircraft allows it to be very robust, extremely lightweight, and capable of flight unlike any other present day air vehicle.

This type of air vehicle has a number of potential applications as a research platform on Earth and other planetary bodies. Because of its relatively small projected mass and flexibility, the aircraft is ideal for planetary exploration. Its characteristics allow the aircraft to be easily stowed and launched at minimal cost. Potentially, a fleet of these aircraft could be deployed within a planet's atmosphere and used for comprehensive scientific data gathering and observation or as communications platforms. A whole planetary science-gathering or communications/navigation architecture can be built around these lightweight, easily deployed, robust aircraft.

The technology to produce this type of aircraft is presently available. There have been great advances in recent years in each of the three main component areas that make up the aircraft

(thin film PV arrays, thin film batteries, and polymer composites). Because of these advances, this type of aircraft may now be possible.

1.2 Vehicle Operation

The unique material composition of the aircraft enables flapping motion of the wing to be used as the main means of propulsion, thereby eliminating the need for a more conventional propulsion system. Its flight motion will consist of intermittent flapping and periods of gliding. During the flapping portion of the flight, the aircraft will gain altitude. Then, during the gliding portion, it will glide back down to the starting altitude. This cycle is shown in Figure 1-3.

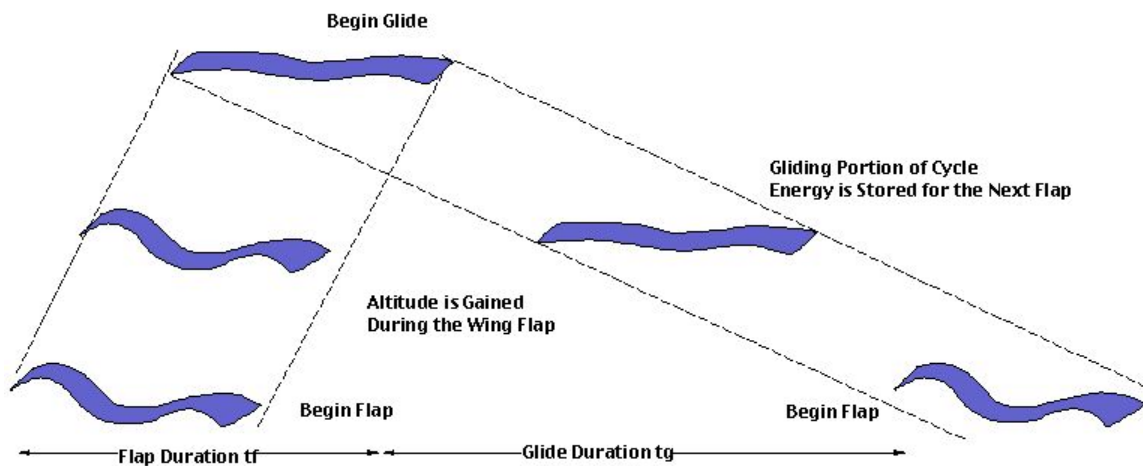


Figure 1-3: Flap-to-glide cycle flight profile

With its estimated low wing loading, it will be able to soar for periods of time and use wing flapping to regain lost altitude. The ratio of flapping time to gliding time will depend on the available power, power-consumption rate, and flight conditions. The flap-to-glide ratio is a critical aspect of vehicle optimization. Various combinations of glide times to flap times can be used. Examples of these combinations are shown in Figure 1-4.

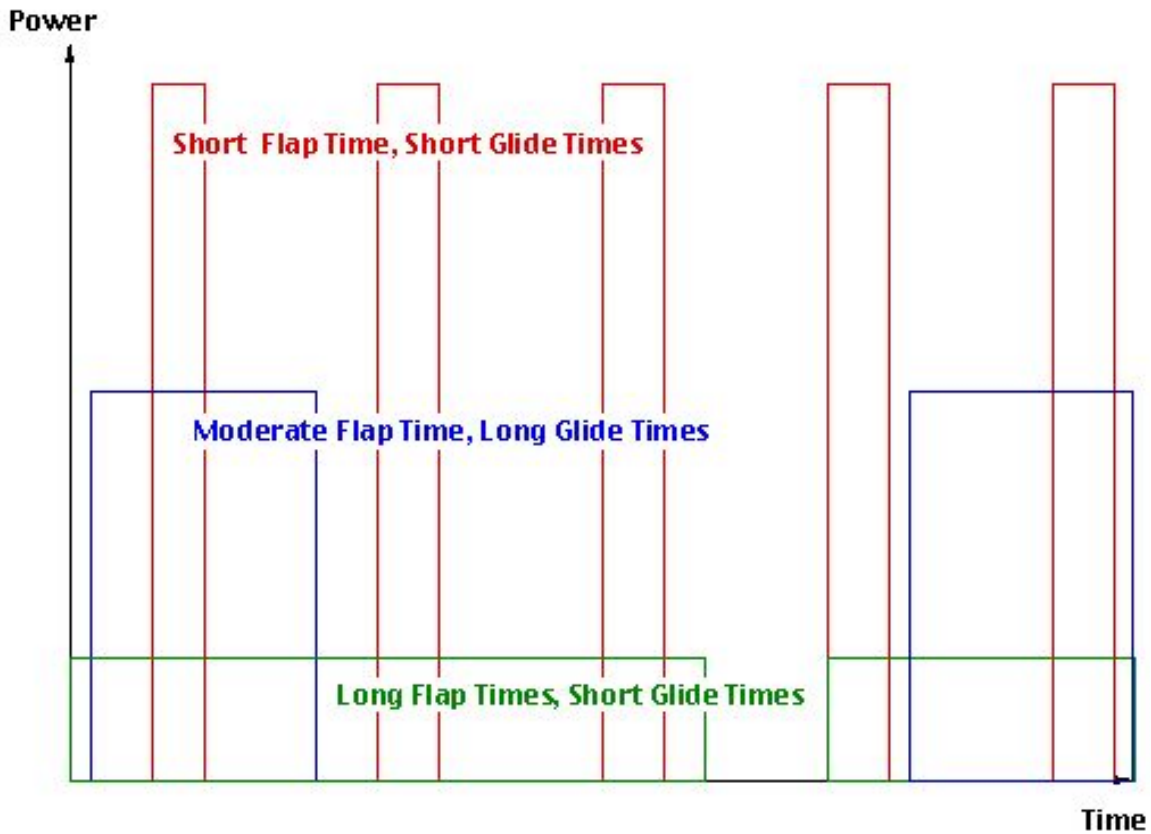


Figure 1-4: Examples of flap-to-glide time ratios

During gliding, the wing shape can be altered to enable steering and control of the aircraft. This control mechanism is similar to that of gliding birds, changing the angle of attack and/or wing shape to produce directional lift on a given wing. This variation in shape can be achieved through a grid of computer-controlled electrodes. The voltage potential can be varied over the grid to tailor the electric field generated to produce non-uniform bending in the wing. This variation in lift can be used to steer and control the aircraft. The force vectors generated by the wing are shown in Figure 1-5 for the upstroke and downstroke.

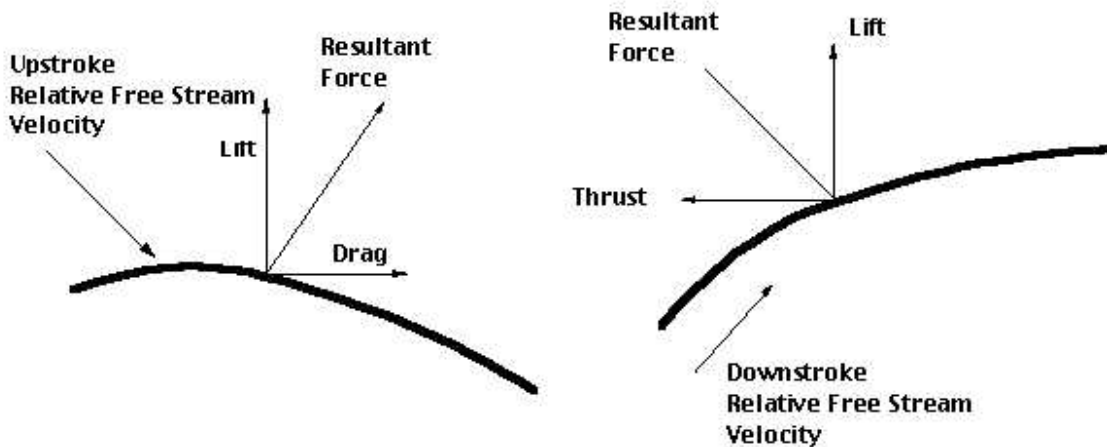


Figure 1-5: Wing forces on upstroke and downstroke

A control grid will be used to control the motion of the wing. This grid will enable various voltages to be sent to different sections of the wing, thereby causing varying degrees of motion along the wing surface. The amount of control of the wing will depend on the fineness of this control grid. A central processor will control the potential of each of the sections to produce the correct motion of the wings to sustain biomimetic flight. Figure 1-6 shows this grid-control concept and the material layers of the wing.

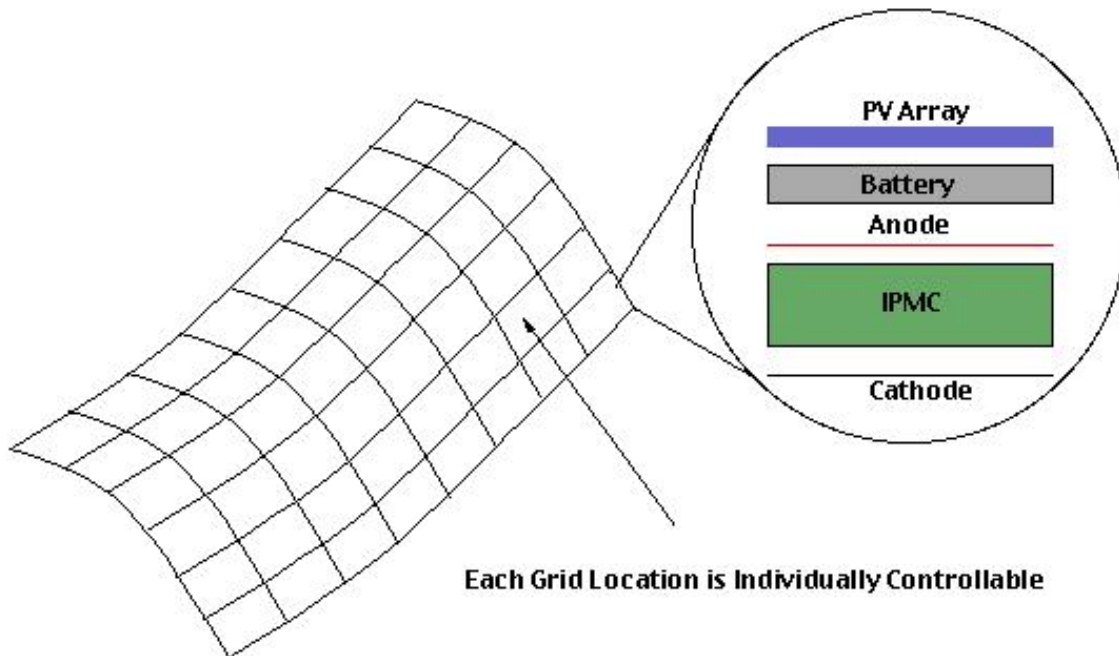


Figure 1-6: Wing-control grid and material composition

The use of solar arrays as the power source requires the aircraft to be used where there is sufficient sunlight. However, because the sun is the main power source and the other systems are sealed and self-contained, oxygen is not required. This is a large benefit, compared to conventionally powered aircraft, when applied to other planets' atmospheres. Potentially, the inner planets of our solar system that have atmospheres (Venus, Earth, and Mars), would be where this type of aircraft could be used.

Chapter 2.0 Component Technologies

2.1 Solar Cell Technology

The nature of the SSA design requires light-weight, thin film, flexible PV arrays for power.

There is a considerable effort in the space PV community to develop thin film PV technology. The requirements for the SSA are not significantly different from those of space satellites. The SSA can easily take advantage of the current development efforts for space thin film PV. Thin film solar cells of sufficient efficiency and specific power (W/Kg) already exist and will enable the SSA to be a prototype operating on

Earth. We need to improve the interconnect technology to turn individual thin film solar cells into an array, but this effort is also being addressed by the space PV community.

The most mature thin film technology is triple junction amorphous silicon cells produced on 0.0005" stainless steel substrates. Figure 2-1 shows a commercially available flexible thin film array for terrestrial use made by Uni-Solar Corporation.

Cells of a similar design have also been produced on 0.001" thick Kapton[®] films and have demonstrated specific power greater than 1,000 W/Kg and efficiencies of 8% to 10%. The projected efficiency for thin film solar cells in 10 to 20 years is 20%. Other solar cell materials, such as the II-VI materials, CuInGaSe, and CdTe, have considerable promise in the long term for high efficiency thin film solar cells.

2.2 Energy Storage

Lightweight energy storage is critical for the operation of an SSA. Environmental conditions imposed on energy storage will be a considerable challenge for most electrical storage technologies. There are three types of energy storage required for an SSA:



Figure 2-1: Flexible amorphous silicon solar array
(Photo courtesy of Uni-Solar Corporation)

1. Low capacity, high impulse power required to manage the loads associated with alternately gliding and flapping wings.
2. High capacity energy storage for nighttime operations.
3. Low capacity energy storage for balance of system requirements, such as control and payload operations.

The importance of each energy-storage need listed above will depend on the specific mission profile. The best candidate technology for Type 1 energy storage is supercapacitors. These devices have very high peak-power capabilities and can withstand the millions of charge/discharge cycles needed for a flapping wing. With current technology, supercapacitors with a specific power of nearly 10 KW/Kg are available.

Type 2 storage is the most challenging. It requires a large amount of stored energy capable of keeping an SSA flying during extended periods of no sunlight. Furthermore, a conventional chemical battery would have to be greatly oversized for a discharge rate low enough to allow for multiple charge/discharge cycles. Typically, batteries discharge at a rate less than 1/5 the charging rate. Therefore, a battery will need to have five times the capacity required, based on a 12-hour charge/12-hour discharge day/night cycle. This leads to an unacceptable mass penalty. Under the most favorable conditions, current thin film batteries would require a battery mass four times greater than the assumption made for the aerodynamic model. Thin film batteries are a rapidly evolving technology, however, and may meet the performance requirements in the future. The most elegant solution for Type 2 energy storage is to store energy as altitude: allow the SSA to climb during the day to store energy and then let it glide down during the night, using minimal power to maintain level flight. Energy storage as altitude has the advantage of a low mass penalty and is insensitive to temperature fluctuations. Drawbacks include less control of the desired operating altitude and weather-related obstacles to gaining or losing altitude.

Type 3 storage needs have considerably more options, including lithium-ion batteries, regenerative fuel cells, and thin film battery technology, such as lithium-polymer batteries. The choice of technology will depend on a combination of environmental constraints as well as system architecture. For example, thin film batteries can be used either as a flexible wing covering or laminated to the structural members, forming a battery skin on the airframe.

2.3 IPMC Material

2.3.1 Ionic Polymer Metal Composites--In General

It is now well documented [2, 1, 13, 20, 16, 5] that ionic polymers in a composite form with a conductive medium such as ionic polymer metal composites, (IPMCs) can exhibit large dynamic deformation if suitably electroded and placed in a time-varying electric field (see Figure 2-2) [2, 1, 13, 20, 16]. Conversely, dynamic deformation of such ionic polymers produces dynamic electric fields across their electrodes as shown in Figure 2-3. A recently presented model by de Gennes, Okumura, Shahinpoor, and Kim [5] describes the underlying principle of electro-thermodynamics in such ionic polymers based upon internal transport phenomena and electrophoresis. It is obvious that IPMCs show great potential as soft robotic actuators, artificial muscles, and dynamic/static sensors in micro- to macro-size scales. This document represents the fundamen-

tals of IPMC manufacturing techniques, phenomenological law, and electronic and electromechanical characteristics.

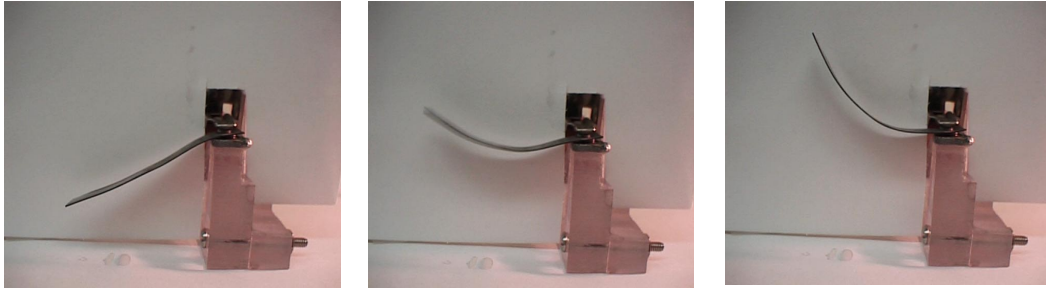


Figure 2-2: Successive photographs of an IPMC strip that shows very large deformation (up to 4 cm) in the presence of low voltage. Note that $\Delta t = 0.5$ sec, 2 V applied. The sample is 1 cm wide, 4 cm long, and 0.2 mm thick.

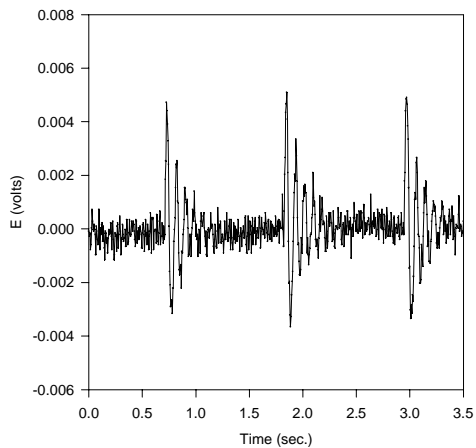


Figure 2-3: A typical sensing response of an IPMC. It shows dynamic sensing response of a strip of an IPMC (40 mm x 10 mm x 0.2 mm thickness) subject to a dynamic impact loading in a cantilever configuration. A damped electric response is highly repeatable with a high bandwidth of up to 100 Hz. Such direct mechano-electric behaviors are related to the endo-ionic mobility caused by imposed stresses. This implies that, if we impose a finite solvent (=water) flux, $|Q|$, not allowing a current flux, $J=0$, a certain conjugate electric field, E , is produced that can be dynamically monitored, as discussed later in Section 2.3.3.

IPMCs can be used in a flapping and aerofoil-maneuvering-and-gliding mode under low voltage, as shown in Figures 2-4 and 2-5.

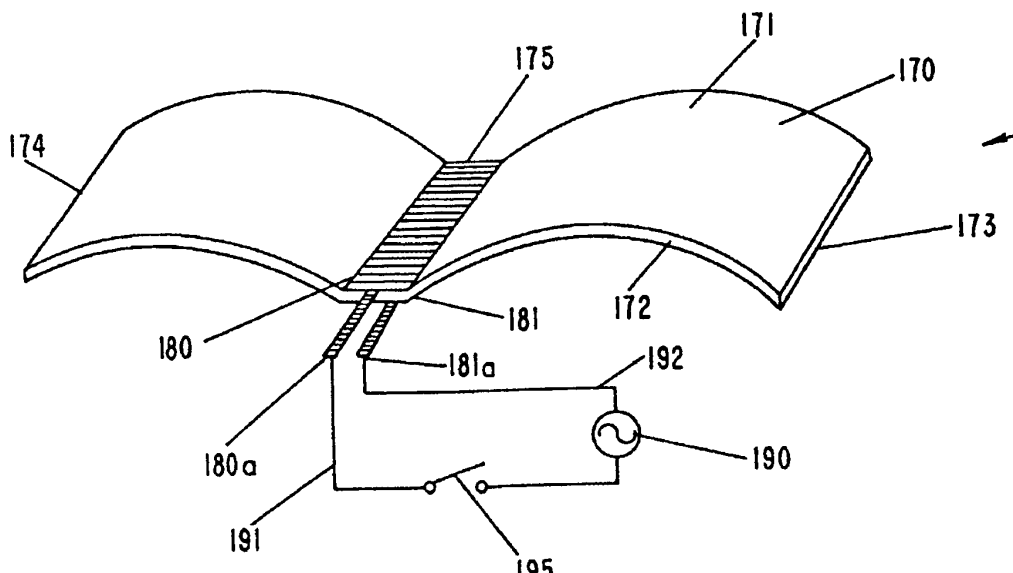


Figure 2-4: A mode of operation of IPMC in flapping and aerofoil gliding maneuvering configuration. Electrodes 175 and 180 can be further printed on the upper 170, 171, or lower 172 wing surfaces, while edges 173 and 174 can perform edge maneuvering and leads 180a and 181a power the wing through circuitry 191 and 192 and controlled switching 195 and oscillatory signal source 190.

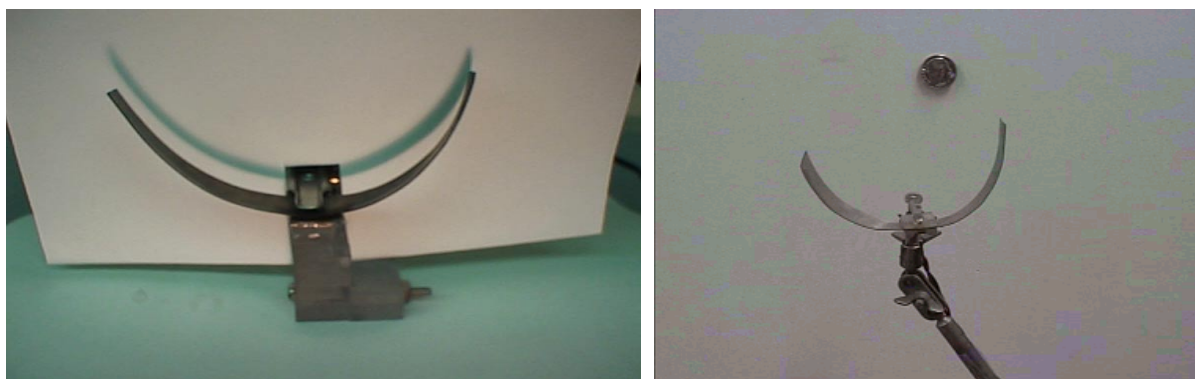


Figure 2-5: IPMC strip in wing-flapping configuration

Manufacturing of an IPMC starts with ion exchange membranes (IEM) via metal compositing by means of chemical reduction processes. The term *ion exchange membranes* refers to materials designed to selectively pass through ions of a single charge (either cations or anions). They are often manufactured from polymers that consist of fixed covalent ionic groups. Currently available IEMs are as follows:

1. Perfluorinated alkenes with short side chains terminated by ionic groups (typically sulfonate or carboxylate (SO_3^- or COO^-) for cation exchange or ammonium cations for anion exchange.) See Figure 2-6. The large polymer backbones determine their mechanical strength. Short side chains provide ionic groups that interact with water and the passage of appropriate ions.

2. Styrene/divinylbenzene-based polymers in which the ionic groups have been substituted from the phenyl rings where the nitrogen atom is fixed to an ionic group. These polymers are highly cross-linked and rigid. Ionic groups are high and analogous to gels.

There are relatively few fixed ionic groups in perfluorinated sulfonic ionic polymers. They are located at the end of side chains to position themselves in their preferred orientation to some extent. Therefore, they can create hydrophilic nano-channels, or so-called *cluster networks*. Such configurations are completely different in other ionic polymers such as styrene/divinylbenzene families that are primarily limited by cross-linking in their ability to expand, due to their hydrophilic nature.

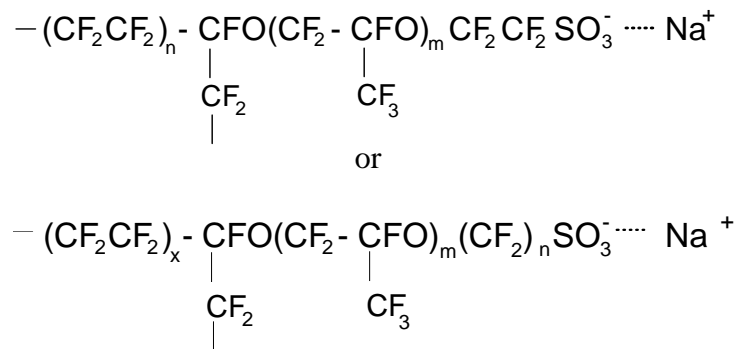


Figure 2-6: Perfluorinated sulfonic acid polymers
The counter ion, Na⁺ in this case, can simply be replaced by other ions.

The final product has a well-defined internal structure as shown in Figure 2-7.

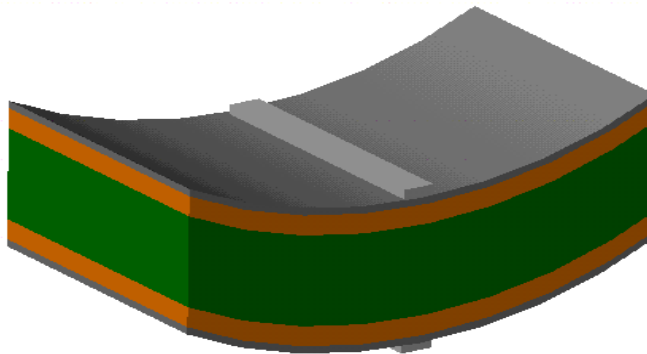


Figure 2-7: IPMC strip after being composited with metal electrodes

2.3.1.1 Dynamic Response of Hydrated Sample

The IPMC sample (25.4 mm x 12.7 mm x 0.3 mm, top, 37.9 mm x 12.7 mm x 0.3 mm, bottom) in a cantilever form was subjected to various AC voltage and kept hydrated by sprayed water. The graphs in Figure 2-8 display the results.

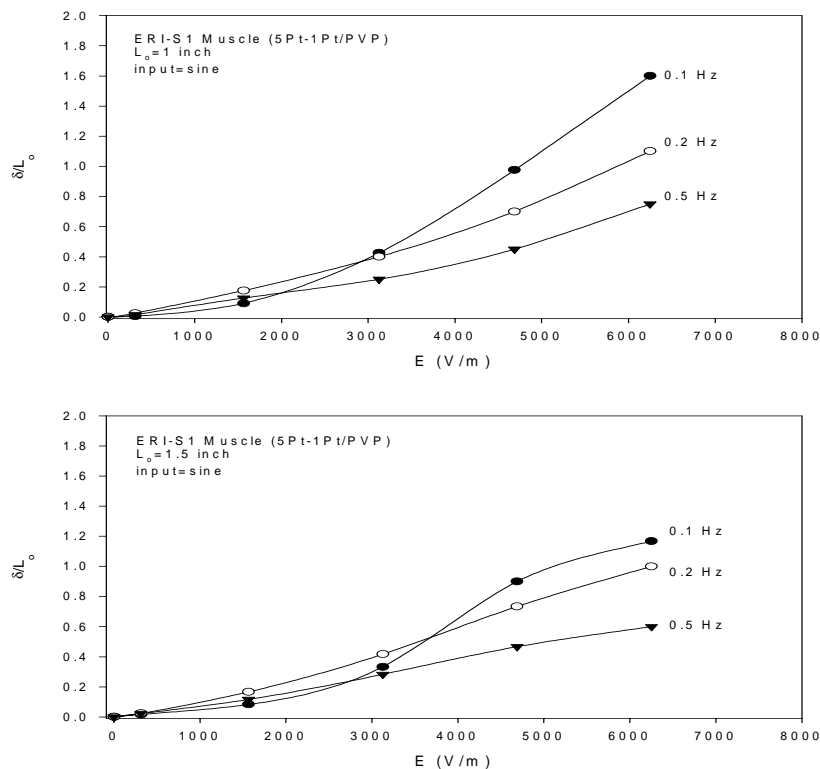


Figure 2-8: Typical amplitude of flapping under oscillatory voltage for small samples of 25.4 mm x 12.7 mm x 0.3mm, (top), 37.9 mm x 12.7 mm x 0.3 mm, (bottom)

2.3.2 Manufacturing Techniques

The preparation of IPMC requires elaborate and extensive laboratory work. The state-of-the-art IPMC-manufacturing technique [20, 16] incorporates two distinct processes: *initial compositing process* and *surface electroding process*. Due to different preparation processes, the morphologies of precipitated platinum are significantly different. Figure 2-9 shows illustrative schematics of two different preparation processes (top-left and bottom-left) and two top-view scanning electron microscope (SEM) micrographs for the platinum surface-electrode (top-right and bottom-right).

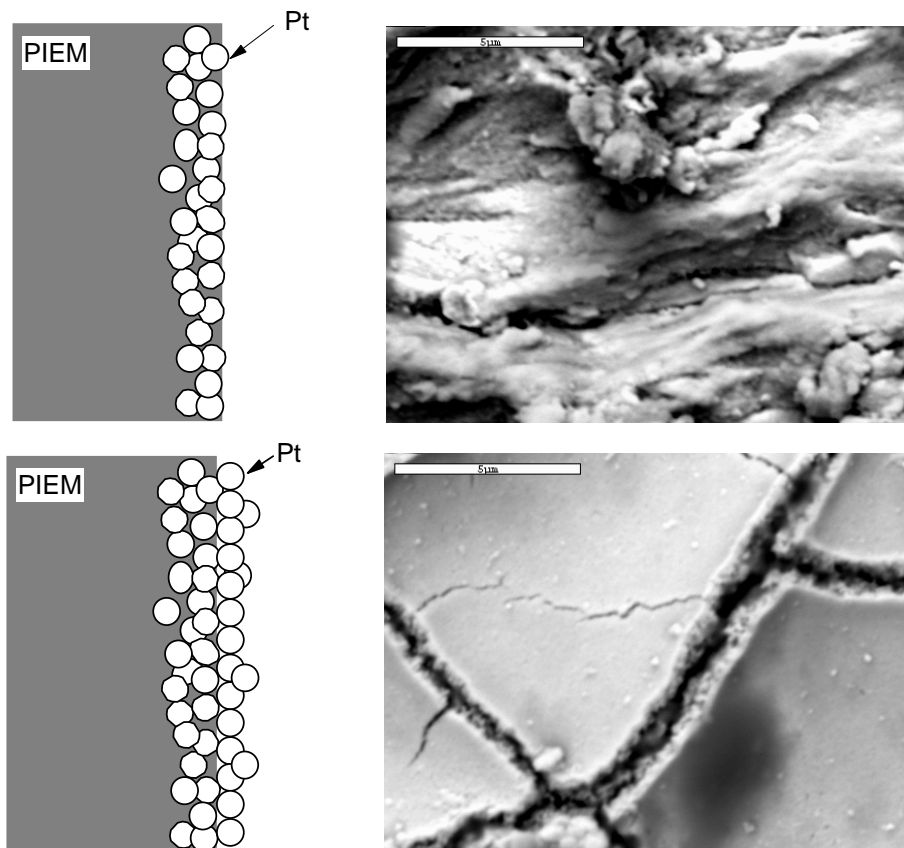
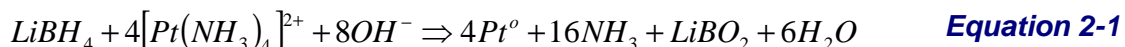


Figure 2-9: Two schematic diagrams showing different preparation processes:
 (top-left): a schematic shows initial compositing process,
 (top-right): its top-view SEM micrograph,
 (bottom-left): a schematic shows surface electroding process, and
 (bottom-right): its top-view SEM micrograph where platinum deposited predominately on top of the initial Pt layer.
 Note that PIEM stands for perfluorinated ion exchange membrane.

The initial compositing process requires an appropriate platinum salt, such as $\text{Pt}(\text{NH}_3)_4\text{HCl}$, in the context of chemical reduction processes similar to the processes evaluated by a number of investigators, including Takenaka [24] and Millet [10]. The principle of the compositing process is to metalize the inner surface of the membrane by a chemical-reduction means, such as LiBH_4 or NaBH_4 . The ionic polymer is soaked in a salt solution to allow platinum-containing cations to diffuse through via the ion-exchange process. Later, a proper reducing agent, such as LiBH_4 or NaBH_4 , is introduced to platinize the membrane. As can be seen in Figure 2-10, the metallic platinum particles are not homogeneously formed across the membrane but concentrate predominantly near the interface boundaries. It has been experimentally observed that the platinum particulate layer is buried a few microns deep (typically 1 mm to 20 mm) within the IPMC surface and is highly dispersed. The fabricated IPMCs can be optimized for producing a maximum force density by changing multiple process parameters, including time-dependent concentrations of the salt and reducing agents (applying the Taguchi technique to identify the optimum process parameters seems quite attractive [16]). The primary reaction is



In the subsequent surface electroding process, multiple reducing agents are introduced (under optimized concentrations) to carry out the reducing reaction similar to Equation 2-1, in addition to the initial platinum layer formed by the initial compositing process. This is clearly shown in Figure 2-5 (bottom-right), where the roughened surface disappears. In general, the majority of platinum salts stays in solution and precedes the reducing reactions and production of platinum metal. Other successfully used metals (or conducting mediums) include palladium, silver, gold, carbon, graphite, and nanotubes.

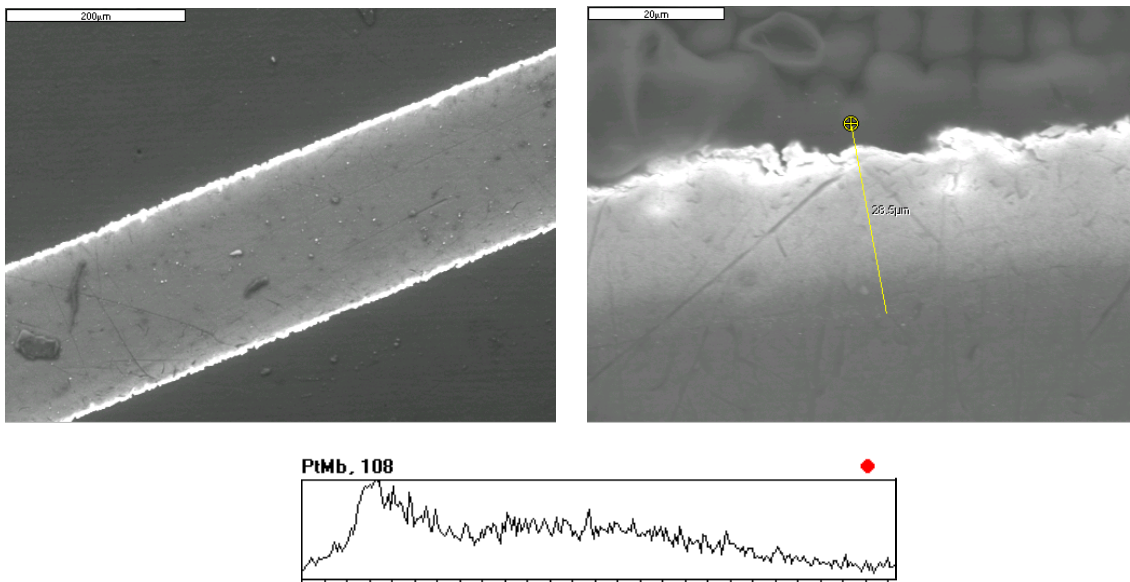


Figure 2-10: Two SEM micrographs (top) showing the cross-section (left) and close-up (right) of a typical IPMC. The bottom graph shows an x-ray line scan of Pt. As can be noticed, Pt is dense at the surface.

To characterize the surface morphology of the IPMC, the atomic force microscopy (AFM) can be used. Its capability to directly image the surface of the IPMC can provide detailed information with a resolution of a few nanometers. In Figure 2-11, we present a representative AFM image (its surface analysis) that reveals the surface morphology of the IPMC. As can be seen, the surface is characterized by the granular appearance of platinum metal with a peak/valley depth of approximately 50 nm. This granular nano-roughness seems to be responsible for producing a high level of electric resistance, yet with a porous nature that allows water movement in and out of the membrane. During the AFM study, it was also found that platinum particles are dense and, to some extent, possess coagulated shapes. Therefore, the study was extended to utilize transmission electron microscope (TEM), to determine the size of the deposited platinum particles.

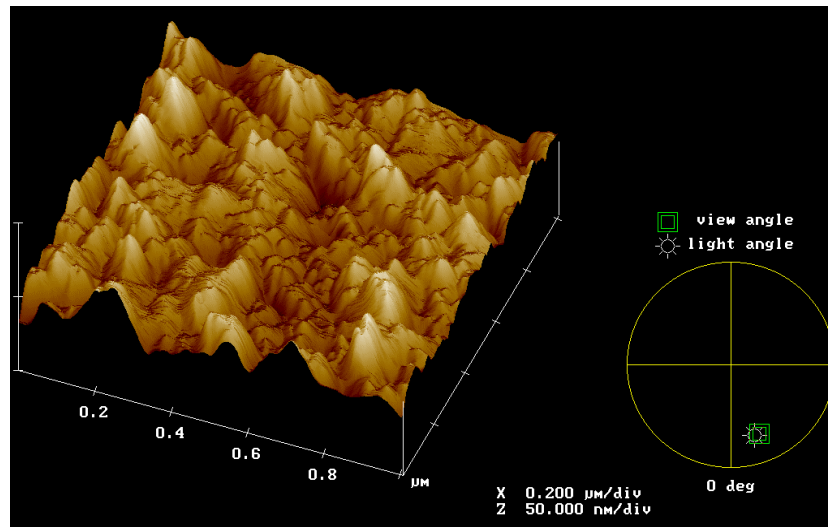


Figure 2-11: An atomic force microscopy (AFM) surface-analysis image taken on the surface electrode of a typical muscle as shown in Figure 2-5 (bottom-right). The scanned area is $1 \mu\text{m}^2$. The brighter/darker area corresponds to a peak/valley depth of 50 nm. The surface-analysis image has a view angle set at 22° . Digital Instruments' AFM NanoScope IIIa was used. A tip (ultra levers) from Park Scientific Instrument was utilized in an air-contact mode under low voltage.

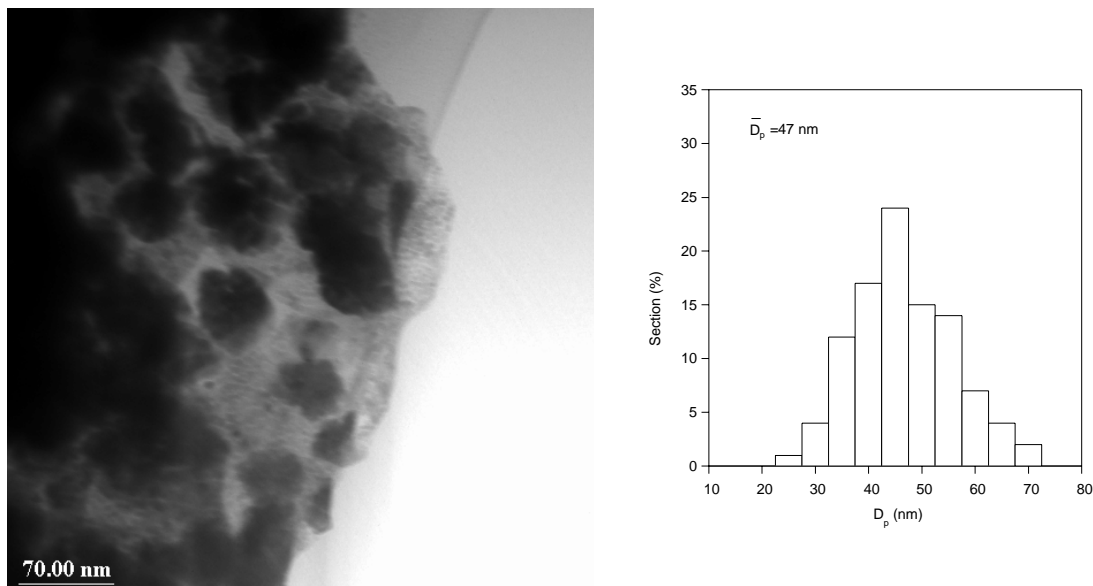


Figure 2-12: A TEM micrograph of the IPMC. It is on the penetrating edge of the IPMC. The sample was carefully prepared in a small piece and ion-beam treated.

2.3.3 Phenomenological Law

A recent study by de Gennes, Okumura, Shahinpoor, and Kim [20] has presented the standard Onsager formulation on the underlining principle of IPMC actuation/sensing phenomena using linear irreversible thermodynamics. When static conditions are imposed, a simple description of *mechano-electric effect* is possible based upon two forms of transport: *ion transport* (with a cur-

rent density, J , normal to the material) and *electrophoretic solvent transport* (with a flux, Q . We can assume that this term is water flux). The conjugate forces include the electric field, \vec{E} , and the pressure gradient, $-\nabla p$. The resulting equations have this concise form:

$$J = \sigma \vec{E} - L_{12} \nabla p \quad \text{Equation 2-2}$$

$$Q = L_{21} \vec{E} - K \nabla p \quad \text{Equation 2-3}$$

where σ and K are the membrane conductance and the Darcy permeability, respectively. A cross-coefficient is usually $L_{12} = L_{21} = L$, experimentally measured to be of the order of 10^{-8} ($\text{ms}^{-1})/(\text{V}\cdot\text{m}^{-1})$. The simplicity of the above equations provides a compact view of underlining principles of both actuation and sensing of IPMC. We can illustrate it simply in Figure 2-13.

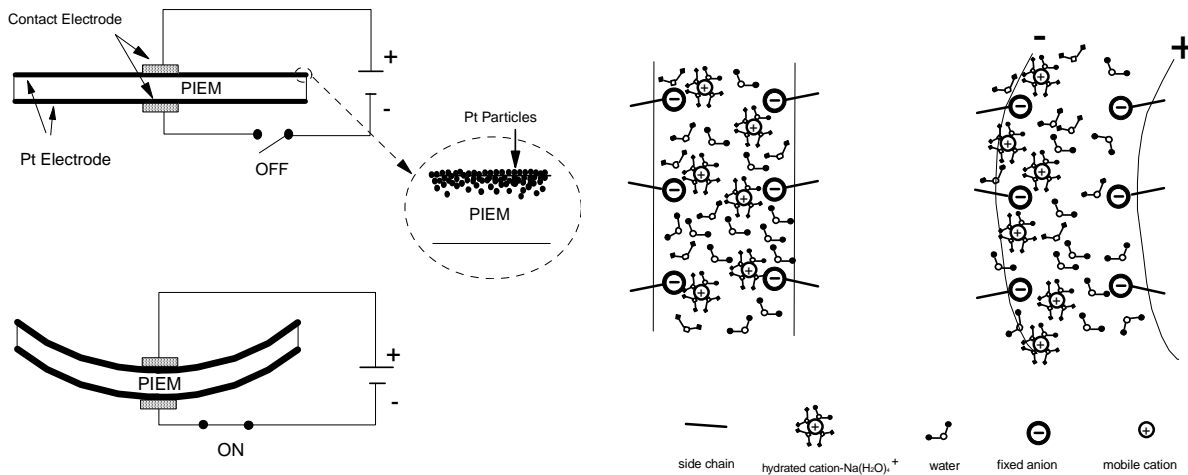


Figure 2-13: A schematic of the typical IPMC artificial muscle and its actuation principle.

The IPMC is composed of a PIEM, chemically surface-composited with a conductive medium such as platinum. A porous platinum layer is formed submicron deep within the PIEM. Typically, the strip of PIEM bends toward the anode (in case of cation-exchange membranes) under the influence of an electric potential. Also, the appearance of water on the surface of the expansion side and the disappearance of water on the contraction side occur near the electrodes. This electrophoresis-like internal water movement is responsible for creating effective strains for actuation. A significant problem often arises from water leakage through the porous Pt-electrode, reducing efficiency.

2.3.4 Characteristics

2.3.4.1 Mechanical

Figure 2-14 shows tensile testing results, in terms of normal stress versus normal strain, on a typical IPMC (H^+ form) relative to NafionTM-117 (H^+ form). Recognizing that NafionTM-117 is the adopted starting material for this IPMC, this comparison is useful. There is a little increase in mechanical strength of IPMC (both stiffness and the modulus of elasticity), but it still follows the intrinsic nature of NafionTM itself. This means that in the tensile (positive) strain, stress/strain

behavior is dominated by the polymer material rather than metallic powders (composited electrode materials).

Although tensile testing results show the intrinsic nature of the IPMC, a problem arises when the IPMC operates in a bending mode. Dissimilar mechanical properties of the metal particles (the electrode) and polymer network seem to affect each other.

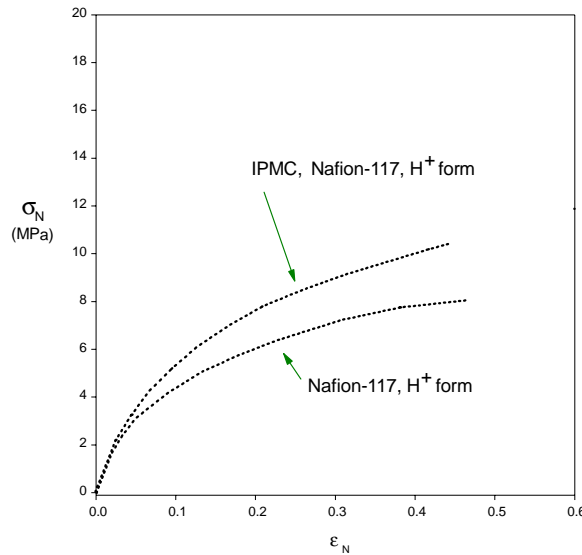


Figure 2-14: Tensile testing results

It shows normal stress, ϵ_N ; IPMC and Nafion-117TM. Note that both samples were fully hydrated when tested.

To construct effective stress-strain curves for IPMCs, therefore, strips of IPMCs are suitably cut and tested in a cantilever configuration. See Figure 2-15(a). In a cantilever configuration, the end deflection δ due to a distributed load $w(s,t)$, where s is the arc length of a beam of length L and t is the time, can be related approximately to the radius of the curvature ρ of the cantilever beam, i.e.,

$$\rho \cong \frac{L^2 + \delta^2}{2\delta} \quad \text{Equation 2-4}$$

Note that the radius of curvature ρ is in turn related to the maximum tensile (positive) or compressive (negative) strains in the beam:

$$\epsilon \cong \frac{h}{2\rho} \quad \text{Equation 2-5}$$

where h is the thickness of the beam at the built-in end. Note that in the actuation mode of the IPMC, the tensile strain can be simply realized but difficult to isolate. In the negative strain (material compression) illustrated in Figure 2-15(b), the metal particles become predominant and so experience much higher stiffness and modulus of elasticity than those in the positive

strain regime. Thus, the mathematical description regarding the physics of the cantilever beam of the IPMC is somewhat challenging and should be addressed carefully. Obviously, experimental approaches are available and should be pursued.

The stress σ can be related to the strain ϵ by simply using Hooke's law, assuming linear elasticity (one can also consider other constitutive equations in which the stress σ can be related to the strain ϵ in a nonlinear fashion i.e., rubber elasticity, a possible future study)). It leads to,

$$\sigma = \frac{Mh}{2I} \quad \text{Equation 2-6}$$

where σ is the stress tensor, M is the maximum moment at the built-in end, and I is the moment of inertia of the cross-section of the beam. Thus, the moment M can be calculated based on the distributed load on the beam or the applied electrical activation of the IPMC beam. Having also calculated the moment of inertia I , which for a rectangular cross-section of width b will be $I = bh^3/12$, the stress σ can be related to the strain ϵ . Representative results are plotted in Figure 2-15(c) and (d). These figures include the effect of swelling (c) and stiffening behavior under electric activation (d). Here, electric activation refers the IPMC in the electromechanical mode exhibiting increased stiffness due to redistributed hydrated ions or nonlinear characteristics of electromechanical properties of the IPMC. A further investigation of such observed findings is currently under way.

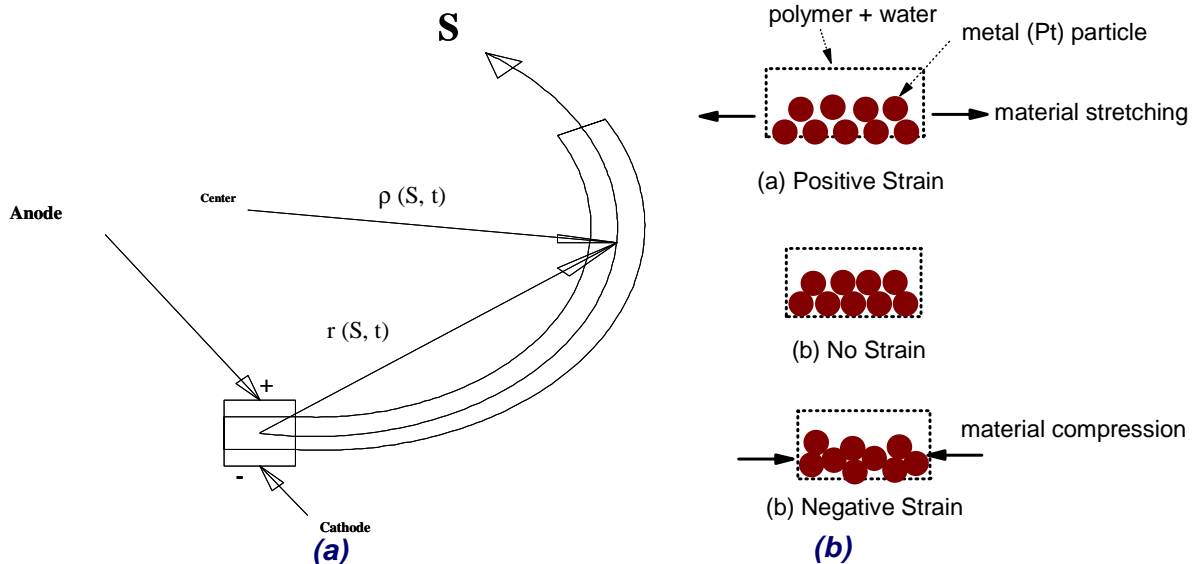


Figure 2-15(a) and (b)

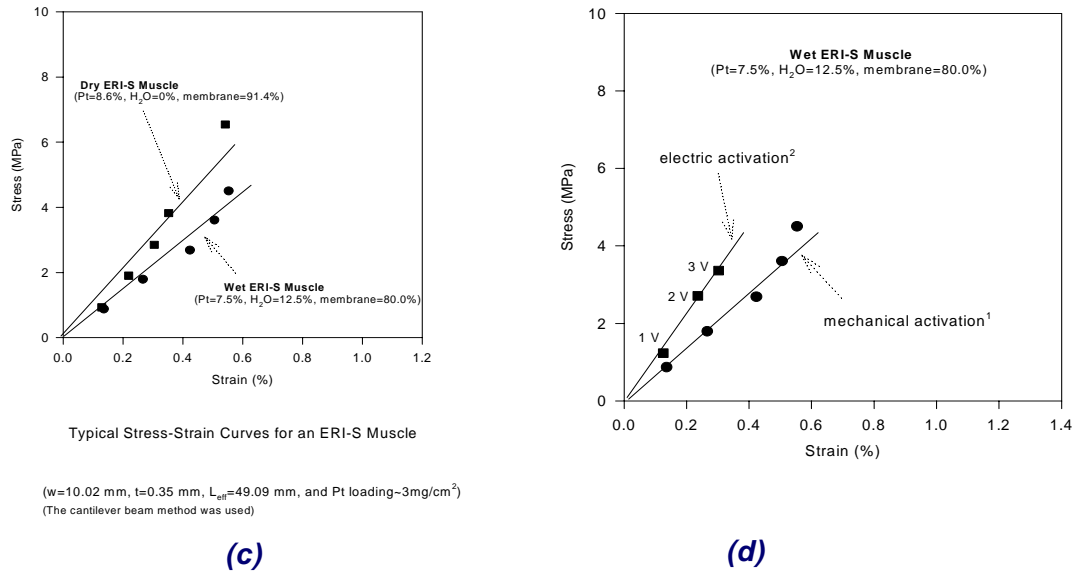


Figure 2-15: A cantilever configuration of the IPMC (a) and an illustration of positive/negative strains experienced in the operation mode of the IPMC. Bottom graphs show the effect of swelling (c) and stiffening behavior under electric activation (d). Swelling is also an important parameter to affect the mechanical property. Indicatively speaking, swelling causes mechanical weakening. Electric activation has a tendency to stiffen the material due to redistributed ions within the IPMC.

2.3.4.2 Electrical

To assess the electrical properties of the IPMC, the standard AC impedance method, which can reveal the equivalent electric circuit, has been adopted. A typical measured impedance plot, provided in Figure 2-16, shows the frequency dependency of impedance of the IPMC. Overall, it is interesting to note that the IPMC is nearly resistive ($> 50 \Omega$) in the high frequency range and fairly capacitive ($> 100 \mu\text{F}$) in the low frequency range.

Based upon the above findings, we consider a simplified equivalent electric circuit of the typical IPMC such as the one shown in Figure 2-17 [16]. In this approach, each single unit circuit (i) is assumed to be connected in a series of arbitrary surface resistances (R_{ss}). This approach is based upon the experimental observation of the considerable surface-electrode resistance (see Figure 2-17). We assume that there are four components to each single-unit circuit: the surface-electrode resistance (R_s), the polymer resistance (R_p), the capacitance related to the ionic polymer and the double layer at the surface-electrode/electrolyte interface (C_d), and an intricate impedance (Z_w) due to a charge-transfer resistance near the surface electrode.

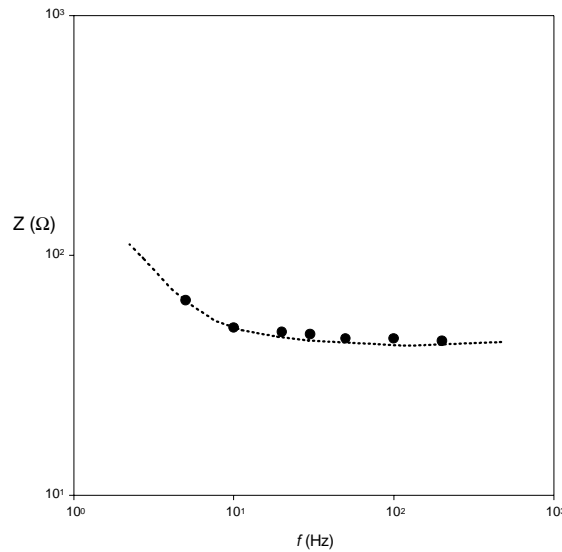


Figure 2-16: The measured AC impedance characteristics of an IPMC sample (the wet IPMC sample is 5 mm x 20 mm x 0.2 mm)

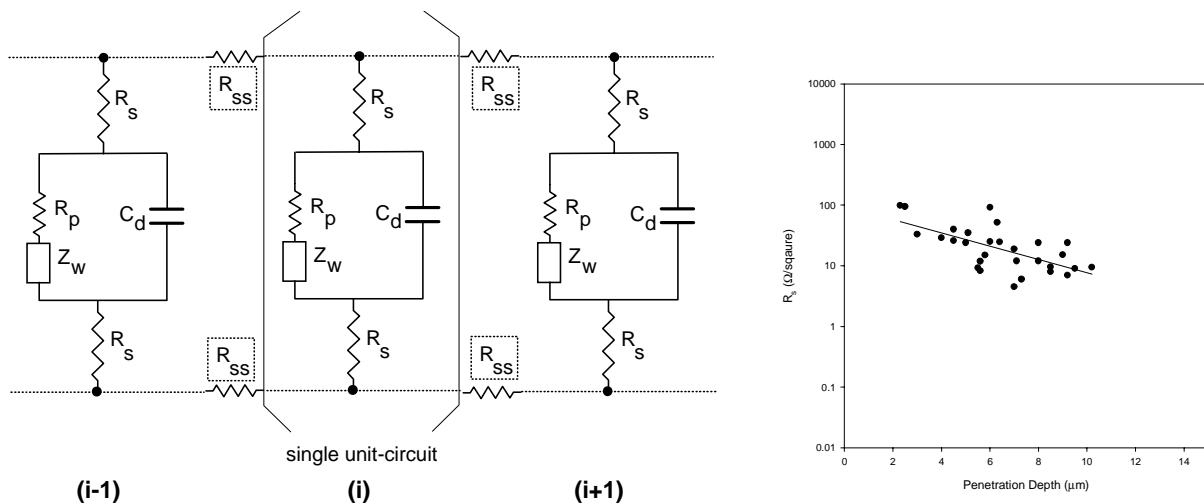


Figure 2-17: A possible electric circuit equivalent to the typical IPMC (left) and measured surface resistance, R_s , as a function of platinum penetration depth (right). Note that SEM was used to estimate the penetration depth of platinum into the membrane. The four-probe method was used to measure the surface resistance, R_s , of the IPMCs. Obviously, the deeper the penetration, the lower the surface resistance.

For the typical IPMC, the importance of R_{ss} relative to R_s may be interpreted from $\Sigma R_{ss} / R_s \sim L/t \gg 1$, where notations L and t are the length and thickness of the electrode (therefore, it becomes two dimensional, therefore, considering that the typical values of t is $\sim 1 \mu\text{m}$ to $10 \mu\text{m}$, so this statement is valid). So, a significant overpotential is required to maintain the effective voltage condition along the surface of the typical IPMC. An effective technique to solve this problem is to overlay a thin layer of a highly conductive metal (such as gold) on top of the platinum surface electrode [16].

Figure 2-18 depicts measured cyclic current/voltage responses of a typical IPMC (the scan rate of 100 mV/sec). As can be seen, a rather simple behavior with a small hysteresis is obtained. Note that the reactivity of the IPMC is mild, such that it does not show any distinct reduction or re-oxidation peaks within ± 4 V, except for a decomposition behavior at $\sim \pm 1.5$ V where the extra current consumption is apparently due to electrolysis. Overall behavior of the IPMC shows a simple behavior of ionic motions caused under an imposed electric field.

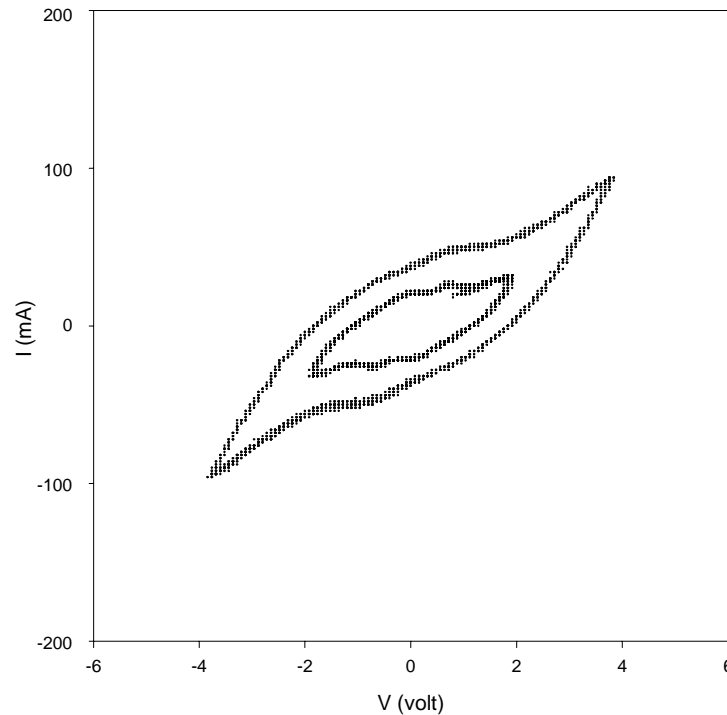


Figure 2-18: I/V curves for a typical IPMC. (NafionTM-117-based IPMC)

In Figure 2-19, frequency dependency of the IPMC is expressed in terms of the normal stress versus the normal strain. Its frequency dependency follows the fact that as frequency increases the beam displacement decreases. However, a careful observation must be given to realize that, at low frequencies (0.1 Hz to 1 Hz), the effective modulus by the IPMC under an imposed voltage seems to be rather small, indicating that water transport is so high that it gushes out of the porous surface electrode, mainly platinum particles (one can routinely observe this effect in the laboratory), and does not return to the polymer network (this causes large irreversibility). On the other hand, at high frequencies (5 Hz to 20 Hz) such an effect is mild so that most water transport phenomena occur within the polymer network, because it does not have enough time to gush out of the surface electrode. Therefore, water transport within the IPMC can experience larger modulus than at low frequencies. This is of interest in a similar analogy to hydraulic actuators. Obviously, water leakage is a definite disadvantage in achieving high efficiency for the IPMC. This issue should be resolved to obtain much higher efficiency and specific power of the IPMC.

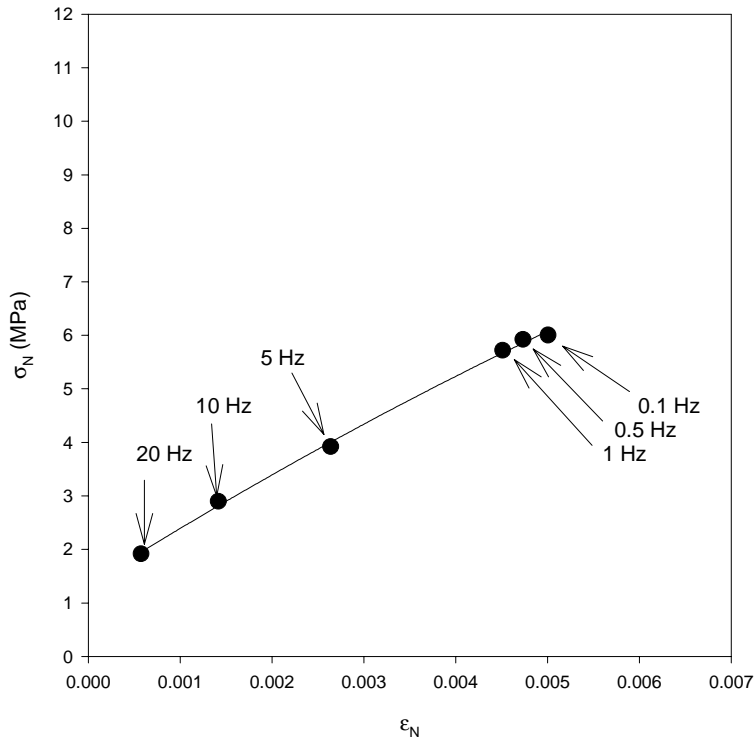


Figure 2-19: Frequency dependency of the IPMC in terms of the normal stress, σ_N , vs. the normal strain, ϵ_N , under an imposed step voltage of 1 V. This Nafion™-117 IPMC has a cation of Li^+ and a size of 5 mm x 20 mm.

The results of longevity testing of flapping IPMC wings are depicted in Figure 2-21 for more than 10 million cycles of flapping (The environmental chamber was maintained at $T=25\text{ }^\circ\text{C}$ and $RH=50-55\%$.)

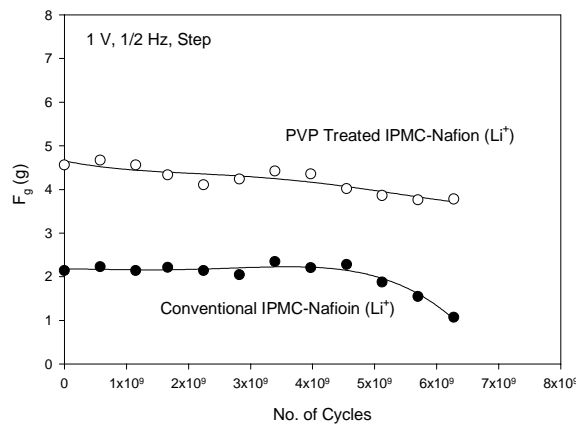


Figure 2-20: Longevity testing of flapping IPMC strips under 1 V square wave and 0.5 Hz.

Figure 2-21 shows the measured blocking forces (typically, 12.7 mm x 5 mm x .2 mm samples in cantilever from Figure 2-22) as a function of electric potential imposed across the IPMCs. Overall, the blocking forces are fairly large (up to 10 g) for both sinusoidal and step inputs at 0.5 Hz. These force measurements clearly indicate the power of IPMCs in undulation as fish fin

actuators. A ballpark figure is that the tip-blocking force of IPMCs in a cantilever mode, which resembles a fish fin in action, is more than 20 times the weight of the fin itself.

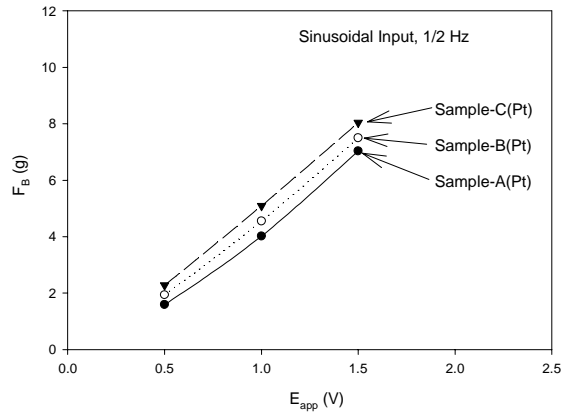


Figure 2-21: Blocking forces measured at the tip of the IPMCs (sinusoidal input @ 0.5 Hz)

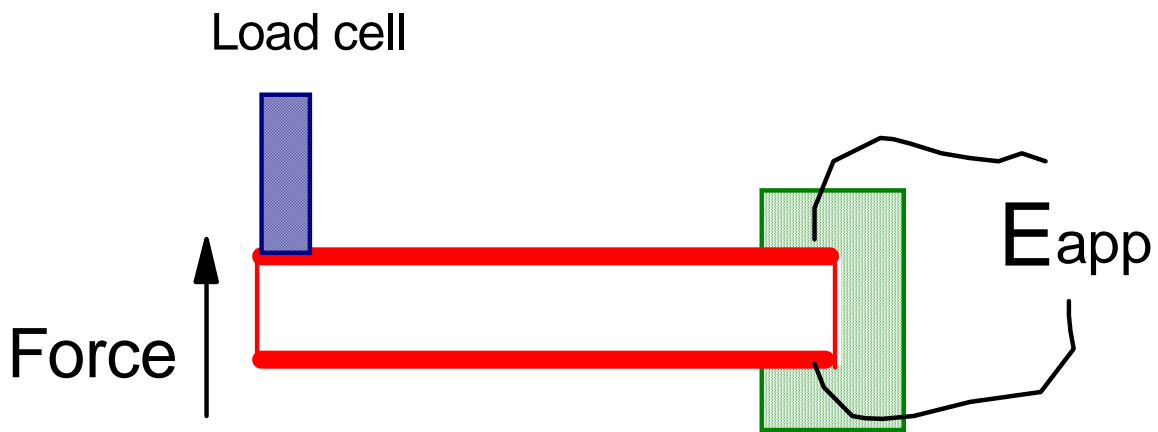


Figure 2-22: A blocking force measurement configuration for undulating IPMC fin actuators

The current properties of IPMCs have been improved as depicted in Table 2-1.

Table 2-1: Current capabilities of IPMC materials

Young's Modulus, E	Up to 2 GPa
Shear Modulus, G	Up to 1 GPa
Poisson's ratio, ν	Typical: 0.3 - 0.4
Power density (W/mass)	Up to 100 J/kg
Maximum force density (cantilever mode)	Up to 40 Kg/Kg
Maximum displacement/strain	Up to 4% linear strain
Bandwidth (speed)	Up to 1 kHz in cantilever vibratory mode for actuations up to 1 MHz for sensing
Resolution (force and displacement control)	Displacement accuracy down to 1 micron, force resolution down to 1 mg

Table 2-1: Current capabilities of IPMC materials (Continued)

Efficiency (electromechanical)	Up to 6% (frequency dependent) for actuation, up to 90% for sensing
Density	Down to 1.8 g/cm ³

Typical specific energy and power density characteristics of IPMC strips are depicted in Figures 2-23 and 2-24. As shown below, IPMCs have a broad frequency spectrum and excellent force and power densities.

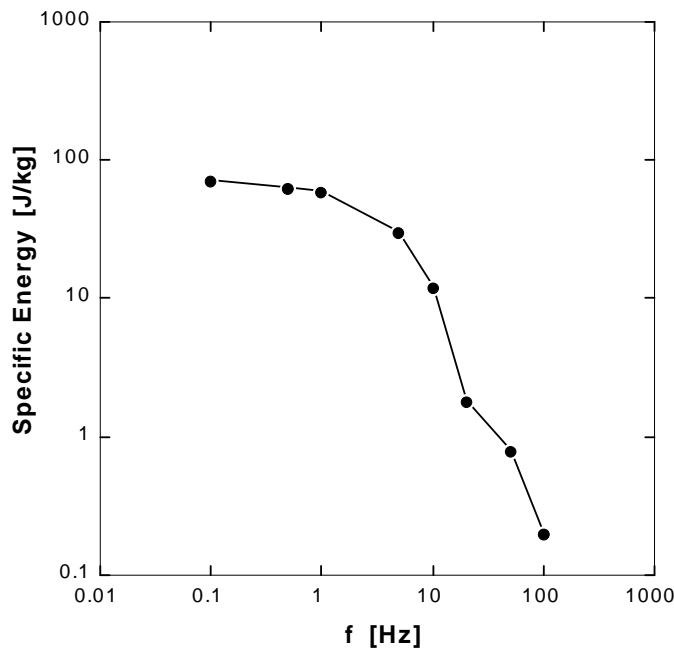


Figure 2-23: Specific energy as a function of frequency for typical IPMC samples. The sample dimensions are 20 mm x 5 mm x 1.6 mm thickness. A maximum square-wave voltage input @ 16 V and Cation = Li+.

Figure 2-24 depicts the variation of power output as a function of frequency of excitation for the same sample described in Figure 2-23.

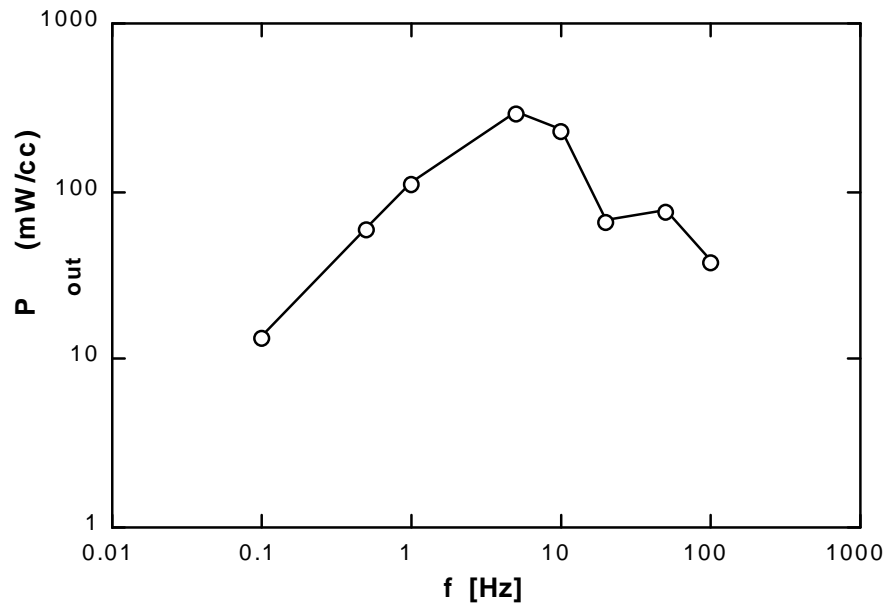


Figure 2-24: Power output as a function of frequencies

In Figure 2-25, the results of potentiostatic analysis are presented. The current passed following the application of an electric potential to the IPMCs (both the poly vinyl pyrrolidone (PVP)-treated IPMC and the conventional IPMC) is shown. The current decays exponentially. The charge passed after time t (Q_t) is:

$$Q_t = \int_0^t I_t dt$$

It is useful to make a direct comparison between $Q_{t,PVP}$ (for the PVP-treated IPMC) and Q_t (for the conventional IPMC). The data shown in Figure 2-25 gives:

$$Q_{t,PVP}/Q_t \cong 1.1$$

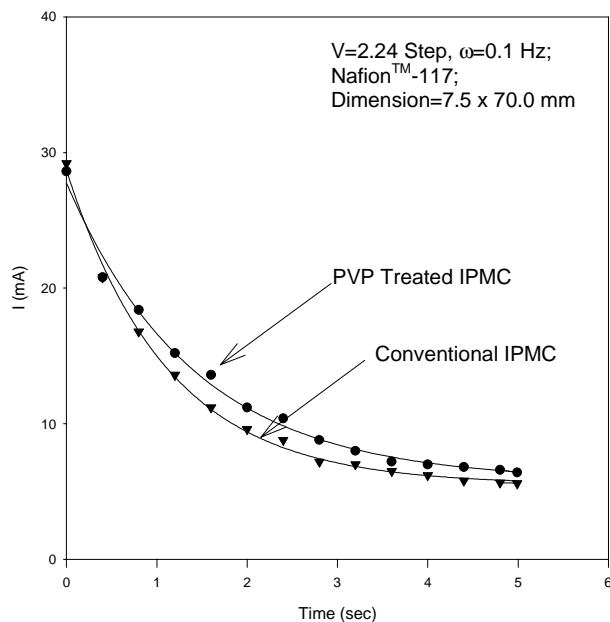


Figure 2-25: Potentio-static coulometric analysis for the additive-treated IPMC and the conventional IPMC. This graph may be interpreted as a statement that an increased current passage (Faraday approach) can contribute the observed improvement in the force characteristics (see Figure 2-18) but not so significant meaning that larger contribution from sandbagging effect.

2.3.5 Cryogenic Properties of IPMC Artificial Muscles

This section reports a number of experimental results pertaining to the behavior of IPMCs under low pressure (few Torrs) and low temperature (-140°C). These experimental results have been obtained in a cryogenic chamber at NASA as well as a cryogenic chamber at the Artificial Muscles Research Institute at the University of New Mexico (UNM) for typical samples of 40 mm x 10 mm x 0.2 mm. The interest was to study the actuation properties of these muscles in a harsh space environment, such as 1 Torr of pressure and -140°C .

In general, the results show that these materials are still capable of sensing and actuating in such harsh conditions as Figures 2-26 through 2-33 display.

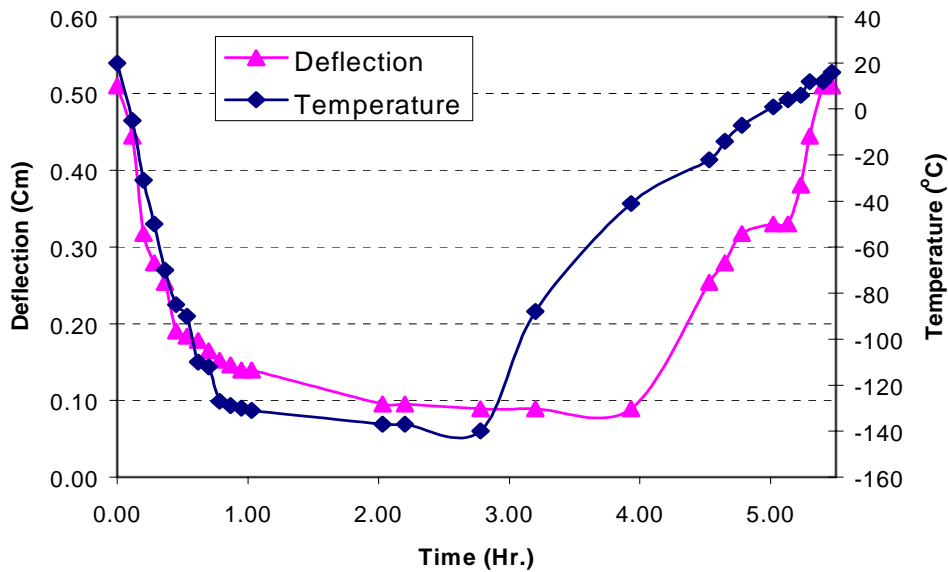


Figure 2-26: Deflection characteristics of IPMC as a function of time and temperature

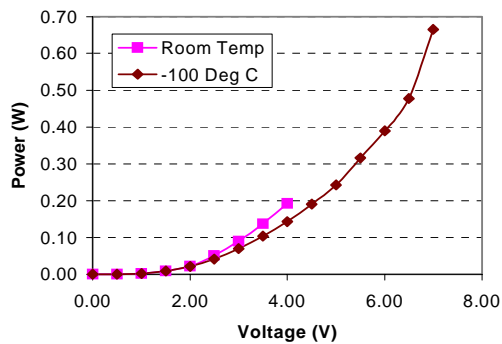


Figure 2-27: Power consumption of the IPMC strip-bending actuator as a function of activation voltage

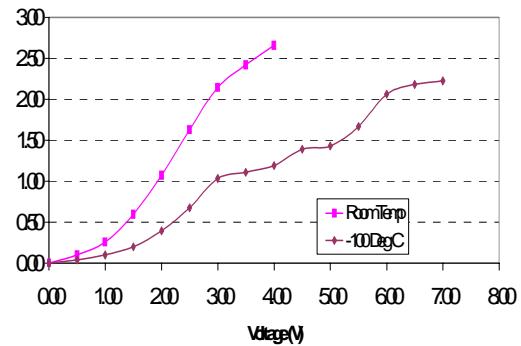
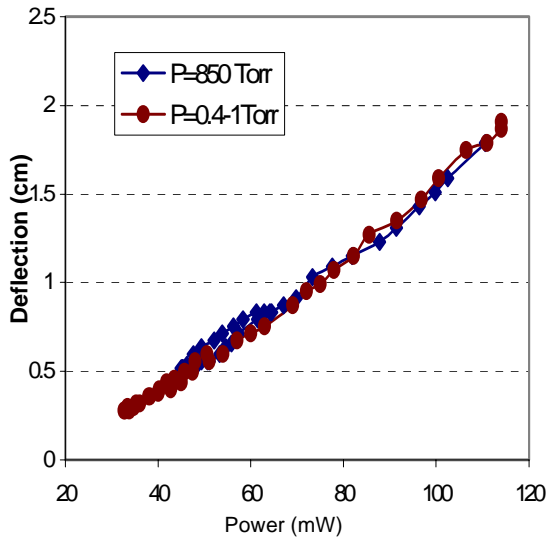
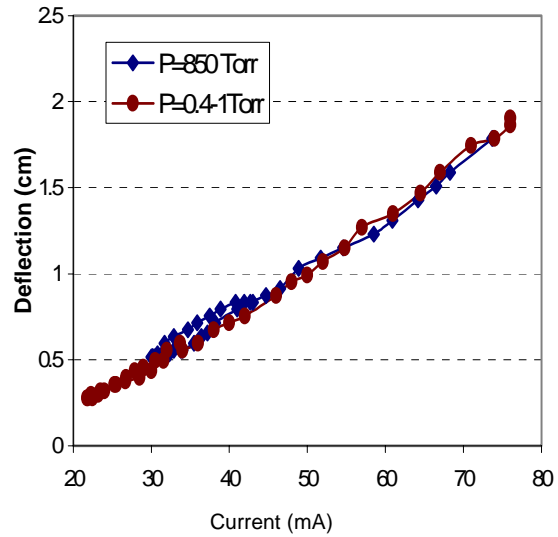


Figure 2-28: Deflection of the bending IPMC strip as a function of voltage

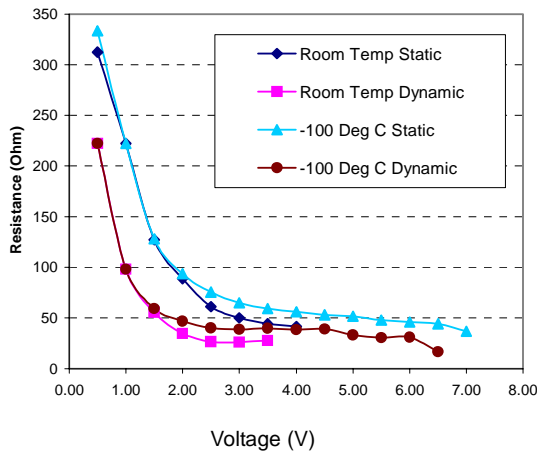


(a) View of the deflection vs. power

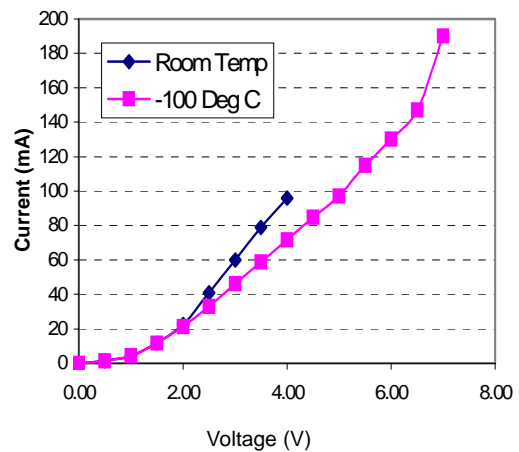


(b) View of the deflection vs. current

Figure 2-29: Deflection vs. power and current under a constant voltage of 3 V and a frequency of 0.1 Hz For two different pressures



(a) IPMC strip static (V/I) and dynamic (V/I) resistance at various temperatures



(b) Relationship between voltage and current for an IPMC strip exposed to RT and to -100° C

Figure 2-30: Effect of temperature on electrical resistance.

Figures 2-31 through 2-33 show the relationships among temperature, voltage, current, power, and displacement in a typical IPMC strips (40 mm x 10 mm x 0.2 mm). Note that the behavior of

this material at low temperatures resembles a semiconductor-type response to colder temperatures more than a typical metallic conductor.

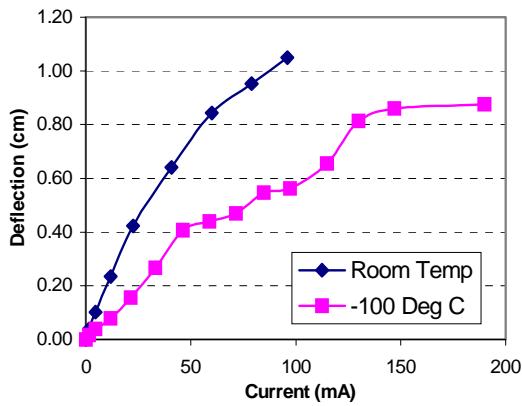


Figure 2-31: Relationship between current and deflection for an IPMC strip exposed to room temperature and -100°C

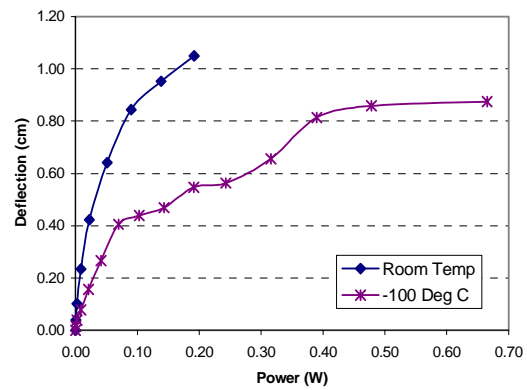


Figure 2-32: Relationship between power and deflection for an IPMC strip exposed to room temperature and -100°C

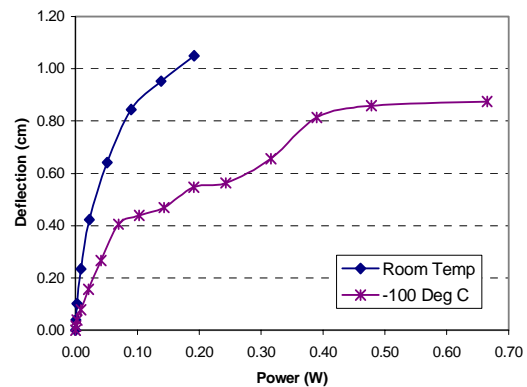
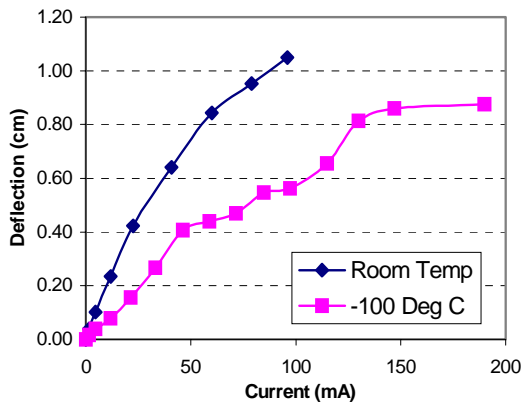


Figure 2-33: Deflection and power consumption of the IPMC muscle as a function of temperature with pressure as a parameter, $V_{peak} = 3\text{ V}$, $Freq = 0.1\text{ Hz}$

2.3.6 Current-Voltage Data for IPMCs

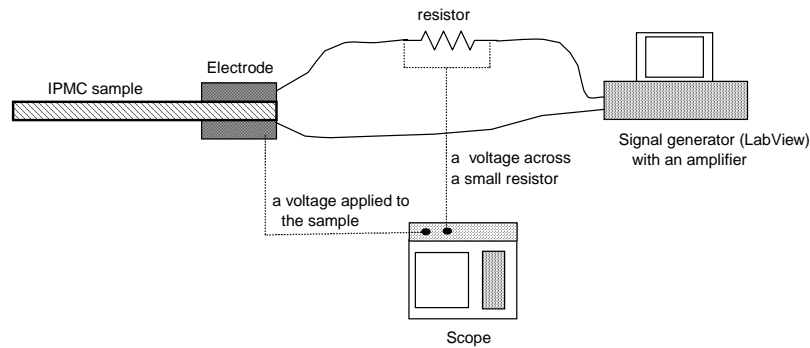
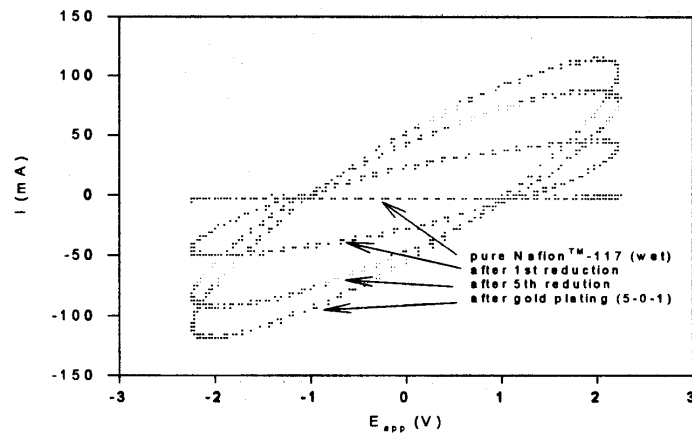


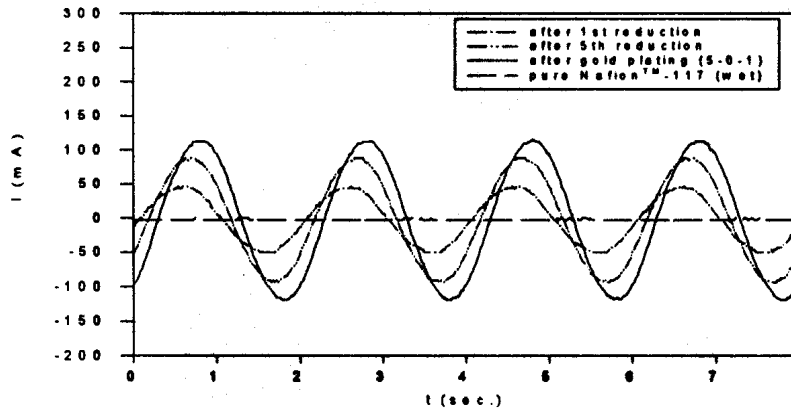
Figure 2-34: Schematic design of the I-V electrical measurement setup



The Current-Voltage Response to Sine Voltages of 2.2 V

Nafion™-117 (Pt), #051199
 E_{app} = 2.2 volts (LabView scale = 1.2), 1/2 Hz,
 Air contact, L = 2", W = 1/2"

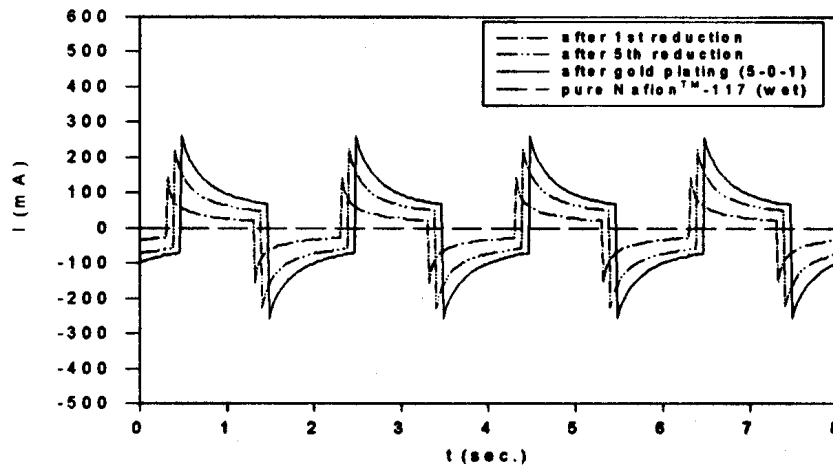
Figure 2-35: Resulting data from typical I-V loops



The Current Response to Sine Voltages of 2.2 V

Nafion™-117 (Pt), #051199
 $E_{app} = 2.2$ volts (LabView scale=1.2), 1/2 Hz.
 Air contact, L=2", W=1/2"

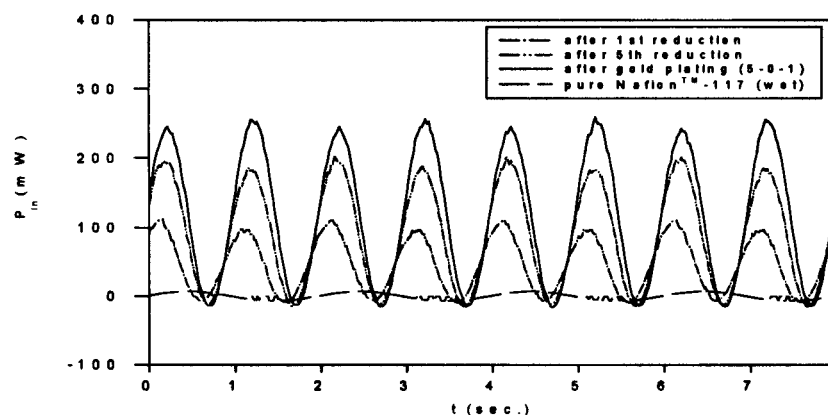
Figure 2-36: Current response of typical IPMC membrane to a sinusoidal voltage of 2.2 V and 0.5 Hz



The Current Response to Step Voltages of 2.2 V

Nafion™-117 (Pt), #051199
 $E_{app} = 2.2$ volts (LabView scale=1.2), 1/2 Hz.
 Air contact, L=2", W=1/2"

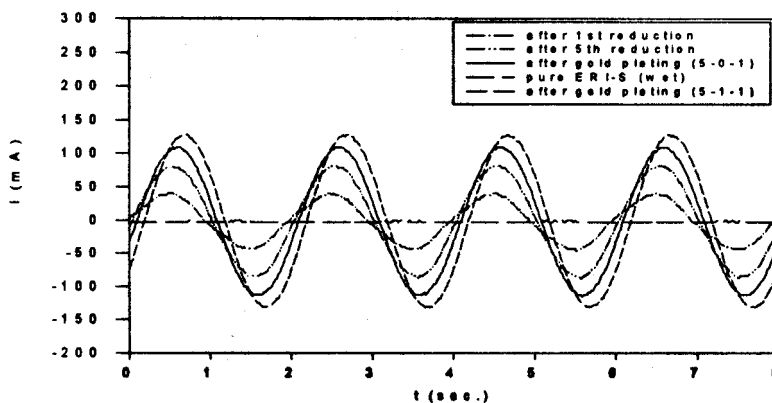
Figure 2-37: Current response of typical IPMC membrane to a square wave step voltage of 2.2 V and frequency of 0.5 Hz.



The Input Power Response to Sine Voltages of 2.2 V

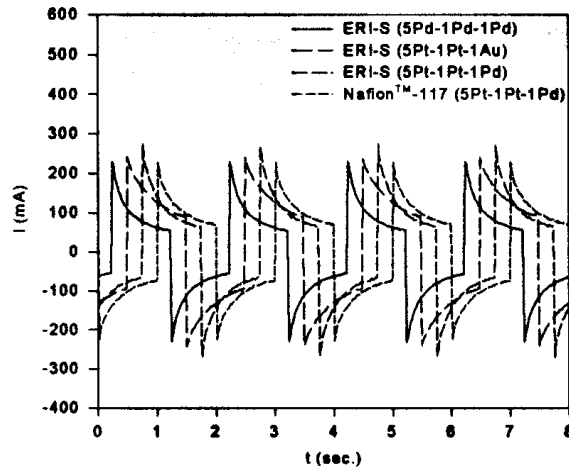
Nafion™-117 (PI), #051199
 $E_{app} = 2.2$ Volts (LabView scale=1.2), 1/2 Hz.
 Air contact, L=2", W=1/2"

Figure 2-38: Variation of input power response of typical IPMC membranes to a sinusoidal voltage of 2.2 V and a frequency of 0.5 Hz



ER I-S (PI), #051489(052889)
 E_{app}
 Air contact, L=2", W=1/2"

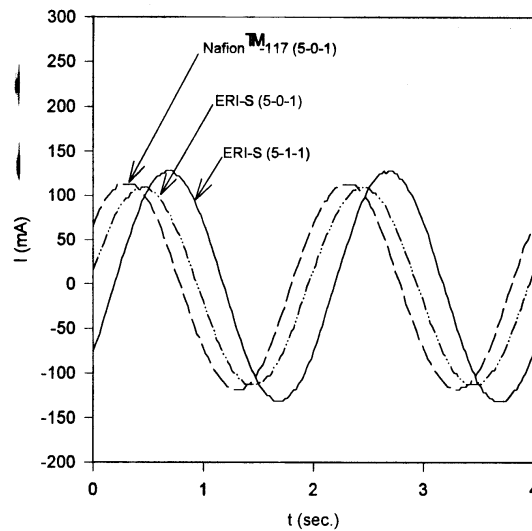
Figure 2-39: Current response of typical IPMC membrane to a sinusoidal voltage of 2.2 V and a frequency of 0.5 Hz



The Current Response to Step Voltages of 2.2 V.

ERI-S, $E_{app}=2.2$ volts, 1/2 Hz, Air contact
(the Cantilever Beam of $L=2''$ and $W=1/2''$)

Figure 2-40: Current response of typical IPMC membrane to a square wave step voltage of 2.2 V and frequency of 0.5 Hz



The Current Response to Sine Voltages of 2.2 V (Nafion™-117 and ERI-S)

$E_{app}=2.2$ volts (LabView scale ~ 1.2), 1/2 Hz,
Air contact, $L=2''$, $W=1/2''$

Figure 2-41: Current response of typical IPMC muscles to a voltage of 2.2 V and a frequency of 0.5 Hz

Chapter 3.0 Aerodynamics

3.1 Introduction

The SSA is an unmanned, high altitude vehicle operating in very low dynamic pressures and relying on flapping flight for propulsion. The SSA does not contain a fuselage, and is basically one continuous sheet of super-capacitor, a thin film PV cell, and an IPMC that deforms under an electric current. The IPMC permits the aircraft to change its shape continuously across its surface and create a surface that provides aerodynamic control, lift, and propulsion in one integrated package. A concept similar to the SSA is shown in Figure 3-1.



Figure 3-1: NASA Pathfinder high altitude aircraft

The Pathfinder vehicle relies on traditional propellers for propulsion. Because the SSA will flap its wing for propulsion like a bird, animal flight will be used as a basis for its design. The aircraft will operate in a very thin atmosphere and depend on very low wing loading to help it glide and stay aloft during the night. It would then flap itself to higher altitudes during the day as its solar cells generate power. High wing aspect ratios would be necessary to reduce induced drag and increase its lift/drag (L/D).



Figure 3-2: Pterosaur

Birds and insects are the biggest groups of animals today that use flapping flight for propulsion. The pterosaurs of the dinosaur era (see Figure 3-2) also used flapping flight for lift and propulsion, and, more importantly, these animals had characteristics more similar to the SSA in terms of their wing spans, Reynolds numbers, aspect ratios, and flight profiles. Thus, the pterosaur's wing planform and aspect ratio are used as a basis for the SSA wing design. Shown in Figure 3-3 are the aspect ratios for two other birds and the pterosaur.

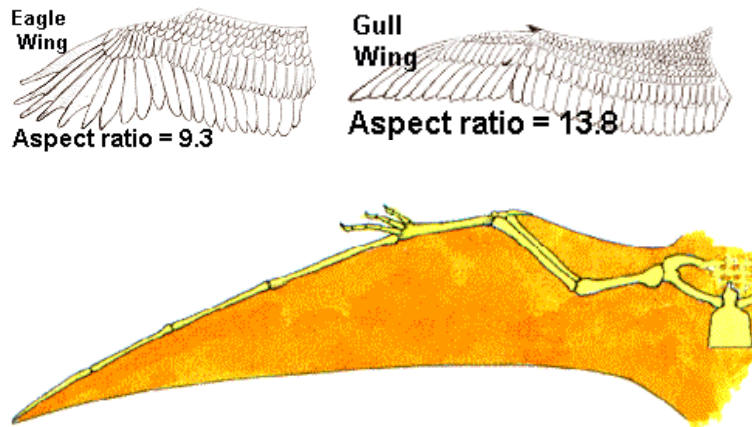


Figure 3-3: Wing planform of pterosaur and various aspect ratios of other birds.

It is well known that higher aspect ratio wings (such as pterosaurs) have less induced drag than shorter wings. Designing airplanes with long wings will benefit their aerodynamics, but weight issues from increased structural requirements start coming into play. An optimum, therefore, must be reached. Archeological findings for the pterosaur indicate flapping frequency of 1.2 Hz, flapping angle of 35° to 40° , a pitch angle of flapping axis with respect to free stream of 7.5° , and a dynamic twist of 4.2° to 5.0° per foot. The pterosaur's long wing has excellent glide characteristics with an L/D of approximately 28:1. Wing camber is similar to Selig's S1223 but with a thinner airfoil section. Zero lift occurred at about -8° to -10.5° , with a quarter chord pitching moment of about -0.3° . The SSA will use a slightly cambered, thin airfoil similar to the Selig 1091.

The overall goal of flapping is the production of a propulsive force. Flapping does not hold the animal or vehicle up by pushing the air down, but rather generates thrust forces (force in the horizontal direction), which manifests itself from the downward movement of the tips of the wings. This thrust force can be generated because of the complex dynamic shape change of the wing through the flapping cycle. Flapping frequencies for insects are very high and their Reynolds numbers very low, and they can benefit from unsteady lift mechanisms, such as vortex shedding over the wing and interaction of air between the wings. This occurs only at certain low Reynolds numbers and flapping frequencies. Birds and pterosaurs, on the other hand, operate at higher Reynolds numbers and do not benefit from the unsteady flow effects. They merely rely on the lift generated by the acceleration of air as it moves over the top of the wing, analogous to the lift generation of an airplane wing. The flapping motion merely produces the propulsive force. This explains why a bumblebee cannot stop its wings in flight like a hawk and glide for long distances before flapping again.

When an animal flaps its wings, the inner part of the wing (near the body) produces lift, and the outer part produces thrust. As the wing sweeps down and forward in the downstroke, the wing near the root experiences a relative wind mostly from the animal's forward flight. The tip, however, experiences a relative wind caused by a combination of the forward flight speed and the

wing's flapping motion. Because of these differences in the direction of the relative wind along the span, the resultant forces near the wing root is nearly vertical (as it would be in a glide), but the resultant force is tilted forward near the tip. Thus the inner part of the wing produces mostly upward force and no thrust, and the outer part provides most of the thrust. The outer part of the wing, though, also may produce plenty of upward force. Generally, the upward component of the force near the tip will be several times larger than the thrust component. A more accurate general statement would be that the upward force (lift) is produced along the whole span of a flapping wing, but thrust is mostly produced on the outer portion of the wing. Factors governing flapping flight are as follows:

- Gait selection
- Flapping frequency
- Wingbeat amplitude
- Stroke angle
- Wing planform
- Angle of attack
- Twist
- Camber

Two different designs will drive the SSA layout, driven by the need to stabilize the wing-pitching moment. According to von Mises' *Theory of Flight*, [25] a cambered, reflexed wing without a tail can be designed to null out the nose-down pitching moment. Due to the high flexibility of this highly adaptive wing structure we are proposing, a properly shaped reflexed wing adapted to the local flow conditions is a possibility. The NASA Pathfinder-Plus aircraft, which operates on a mission similar to the SSA's, demonstrates that nonswept wing aircraft can be flown without a tail (although it has some kind of elevator on the trailing edge of the wing). The yaw and roll modes would be controlled by changing the wing shape evenly across the entire span. This is a direct contrast to the more traditional methods of producing asymmetric lift via ailerons, which act only over the outer portions of the wing and modify the lift distribution only over the span over which they are connected.

The other layout would incorporate a short, coupled, horizontal tail, much like that of a hawk or airplane, in which the tail generates negative lift to compensate for the pitching moment.

Yet another possibility would be to combine the two models (a small elevator and wing twist).

3.2 CFD Calculations: WIND

Two-dimensional computational fluid dynamics (CFD) calculations were completed with the WIND code, a CFD code that solves Reynolds-averaged Navier-Stokes equations. These calculations were completed on the Selig 1091 airfoil, a generic low speed airfoil representative of something that could be used for the SSA application. These were completed at mach number 0.19, and Reynolds number of 100,000 to ascertain the lift and drag at high altitudes and low mach numbers. The Selig 1091 cases were run two-dimensionally, steady state, turbulent, representing the SSA in gliding or soaring flight (see Figures 3-4, 3-5, and 3-8). The computational grid (Figure 3-7) created with GRIDGEN, contains 299 points chordwise and 100 points normal

to the airfoil. Points were clustered close to the airfoil surface to capture the boundary-layer effects. Lift coefficient (C_l) and drag coefficient (C_d) values were tabulated for various angles of attack up to 24° . The XFOIL program, a panel method code for quickly analyzing airfoils written by Mark Drela at MIT, was used to verify the values from WIND for the Reynolds number = 100,000 case. They are shown in Figures 3-6 and 3-9. XFOIL can simulate viscous effects in the boundary layer but becomes unreliable at high angles of attack due to separation. Additional C_l and C_d values were found for the Reynolds number = 200,000, 300,000, 400,000, and 500,000 cases using only XFOIL for mach number 0.19. XFOIL showed very slight differences between lift and drag for the different Reynolds numbers, although experimental data shows larger differences. This discrepancy could be a result of coarse gridding and unsteady viscous effects that are neglected in XFOIL.

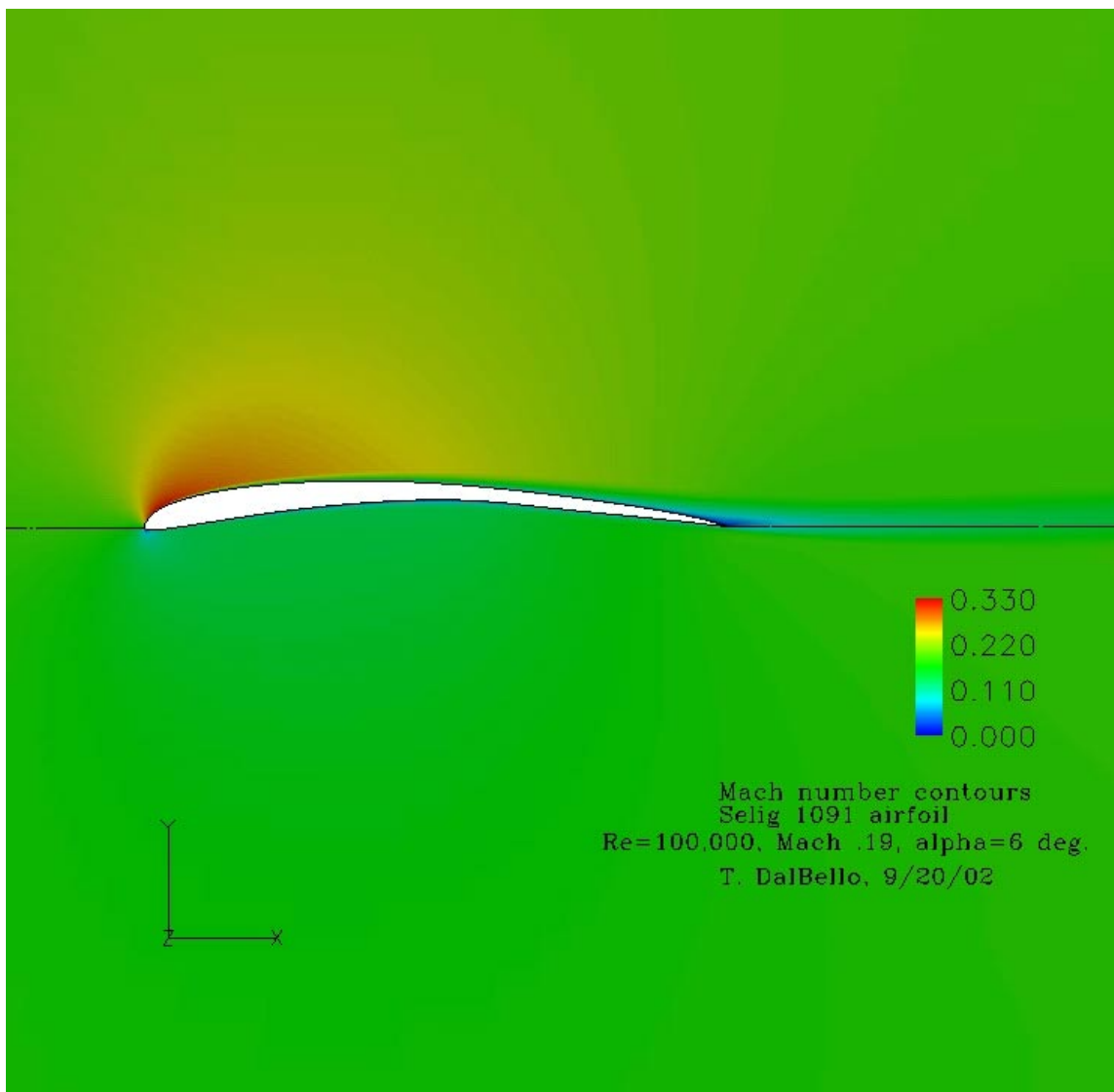


Figure 3-4: Mach number contours around the Selig 1091 airfoil at Reynolds number 100,000, mach number 0.19, and 6° angle of attack

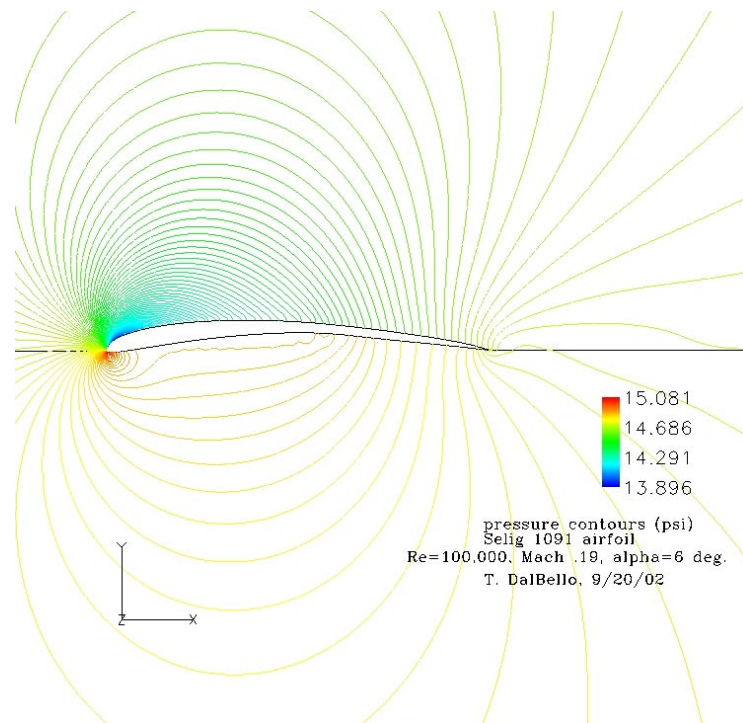


Figure 3-5: Status pressure contours around the Selig 1091 airfoil at Reynolds number 100,000, mach number 0.19, and 6° angle of attack

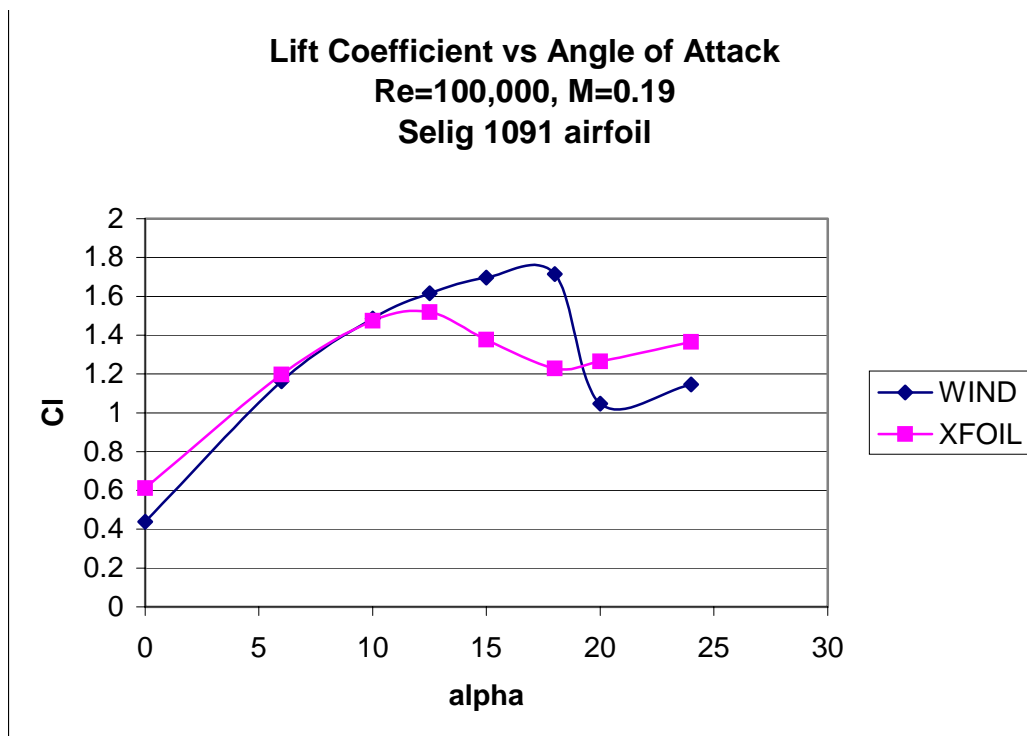


Figure 3-6: Lift coefficient vs. angle of attack for WIND and XFOIL computations

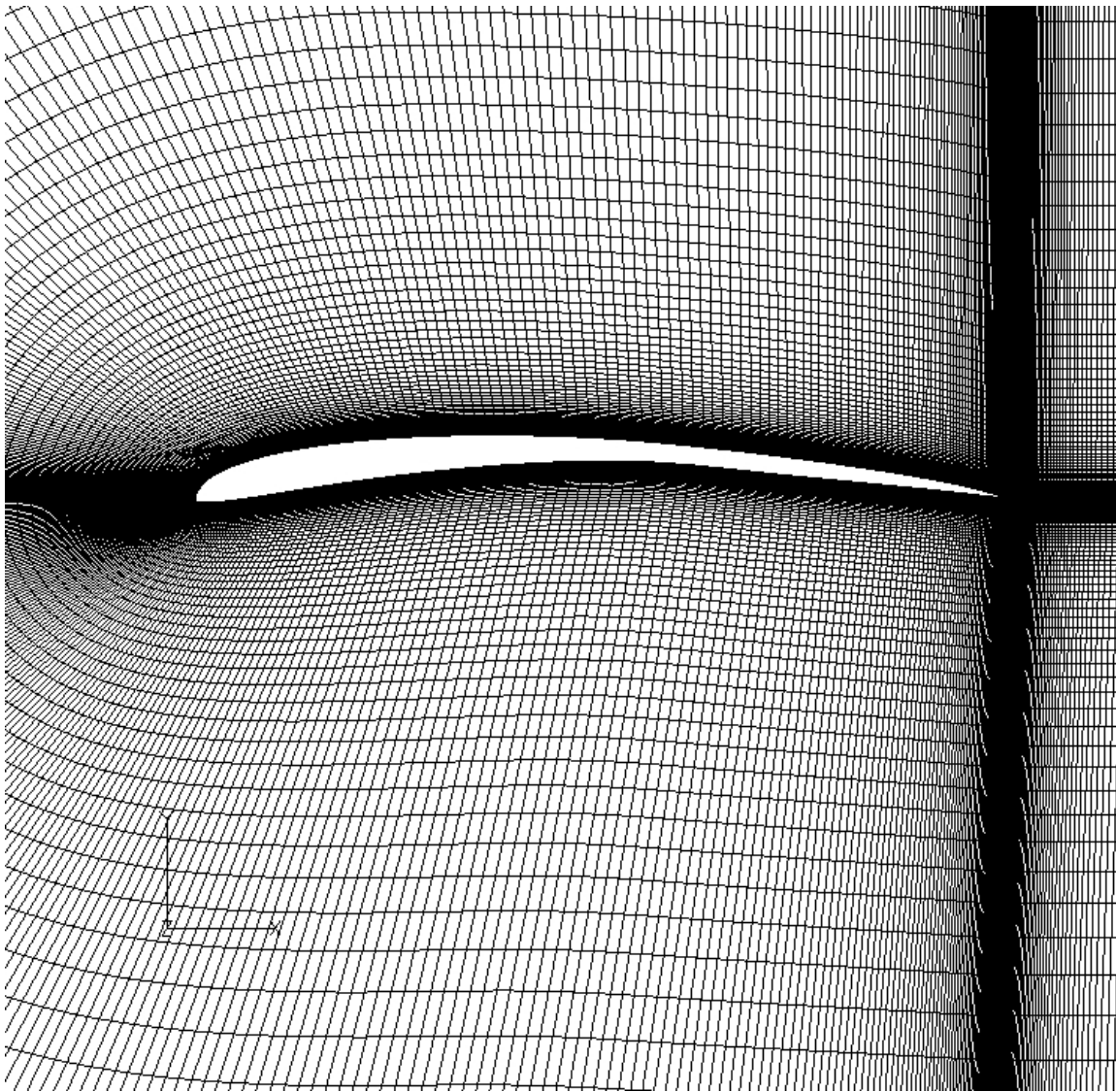


Figure 3-7: 299 x 100 grid used for the CFD calculations

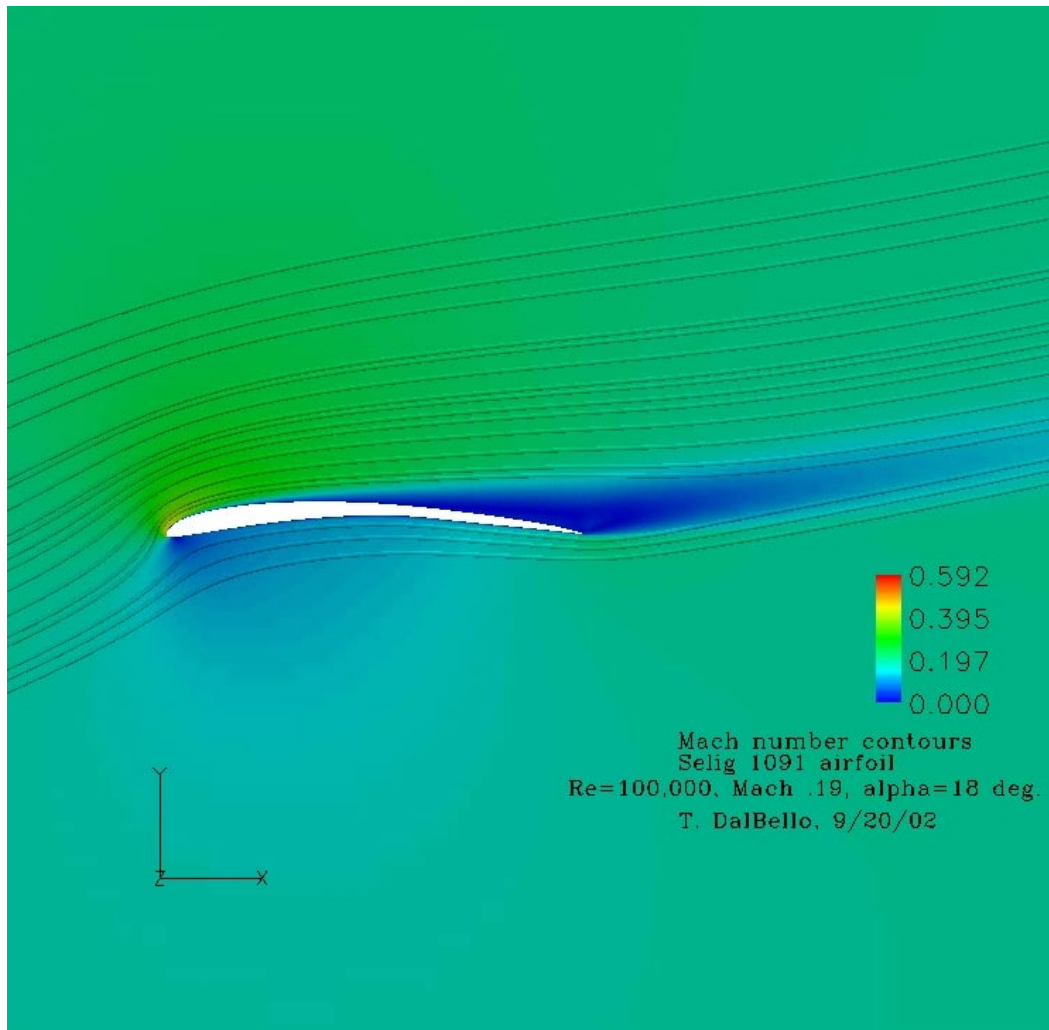


Figure 3-8: Streamlines around the Selig 1091 airfoil at Reynolds number 100,000, mach number 0.19, and 18° angle of attack

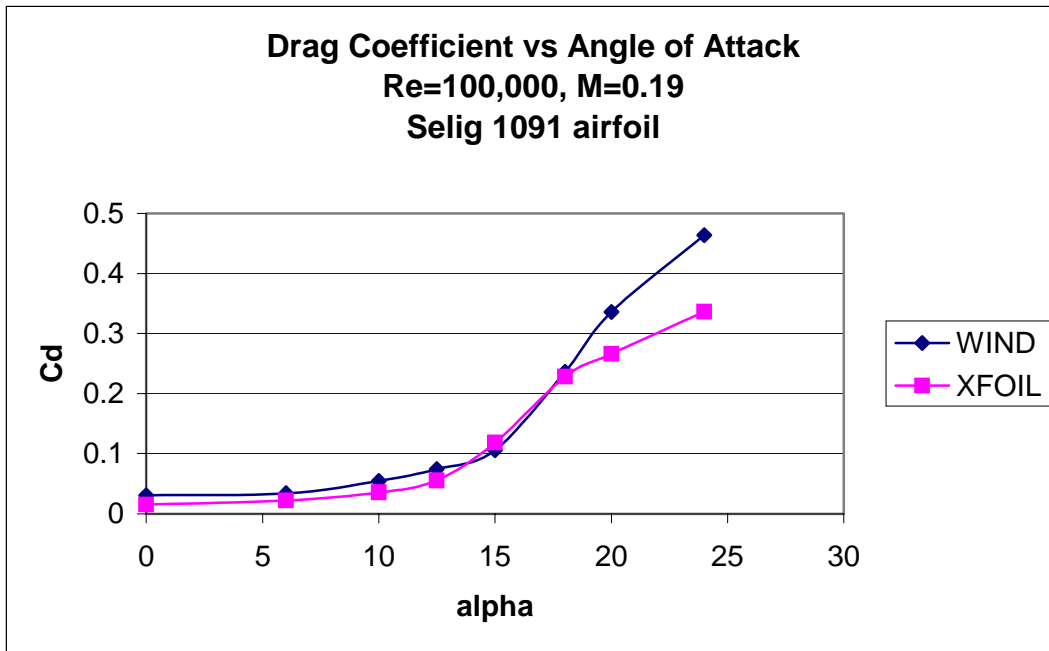


Figure 3-9: Drag coefficient vs. angle of attack for WIND and XFOIL computations

Chapter 4.0 Environment

4.1 Proposed Operational Environments

The environment in which the aircraft will operate has a large influence on its performance. This influence, which is greater than for most conventional aircraft, is mainly because the aircraft receives all of its operating power from the sun. Therefore, environmental conditions that affect the power available from the sun have a significant impact on aircraft performance. The aircraft can potentially operate at any location that has sufficient solar intensity and atmospheric density. It can, therefore, potentially operate on Venus, Earth, and Mars. The environmental conditions on each of these planets are drastically different and must be characterized to determine what effect they would have on the aircraft's operations. The aspects of the environments of interest include the physical characteristics of the planet, its atmospheric composition and conditions at various altitudes, and the solar power available at different altitudes, latitudes, and times of the year.

4.2 Environmental Conditions for Flight on Venus

Venus is very similar in size to Earth. The environmental conditions on Venus are unlike those on any other planet or moon. The planet has a very thick atmosphere with cloud cover over the entire planet. Venus may, however, be an ideal place to fly a solar aircraft, because the cloud cover only extends from approximately 45 km to approximately 64 km above the surface. At the top of the cloud layer, the atmospheric pressure is around 0.1 bar. Within this altitude, the atmospheric temperature ranges from 80° C to -35° C. The temperature profile on Venus is shown in Figures 4-2 and 4-3 [26]. Operation within this temperature range will not be an issue. In fact, operation at the colder end of the range will increase solar array performance. The top of the cloud layer corresponds to a pressure altitude on Earth of 16 km (52,500 ft). Although high, this altitude is well within the range of modern aircraft, and flight aerodynamics within this regime are well understood. [8]

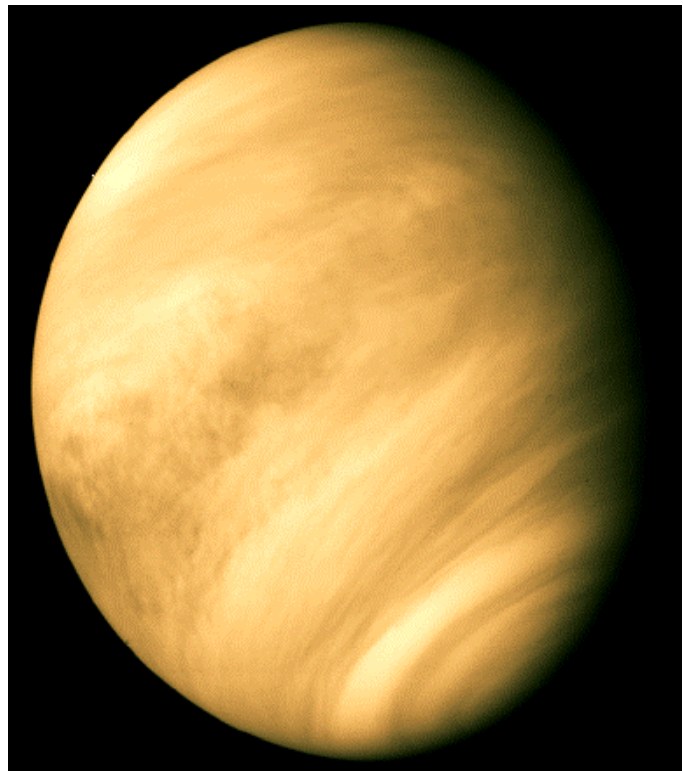


Figure 4-1: Venus

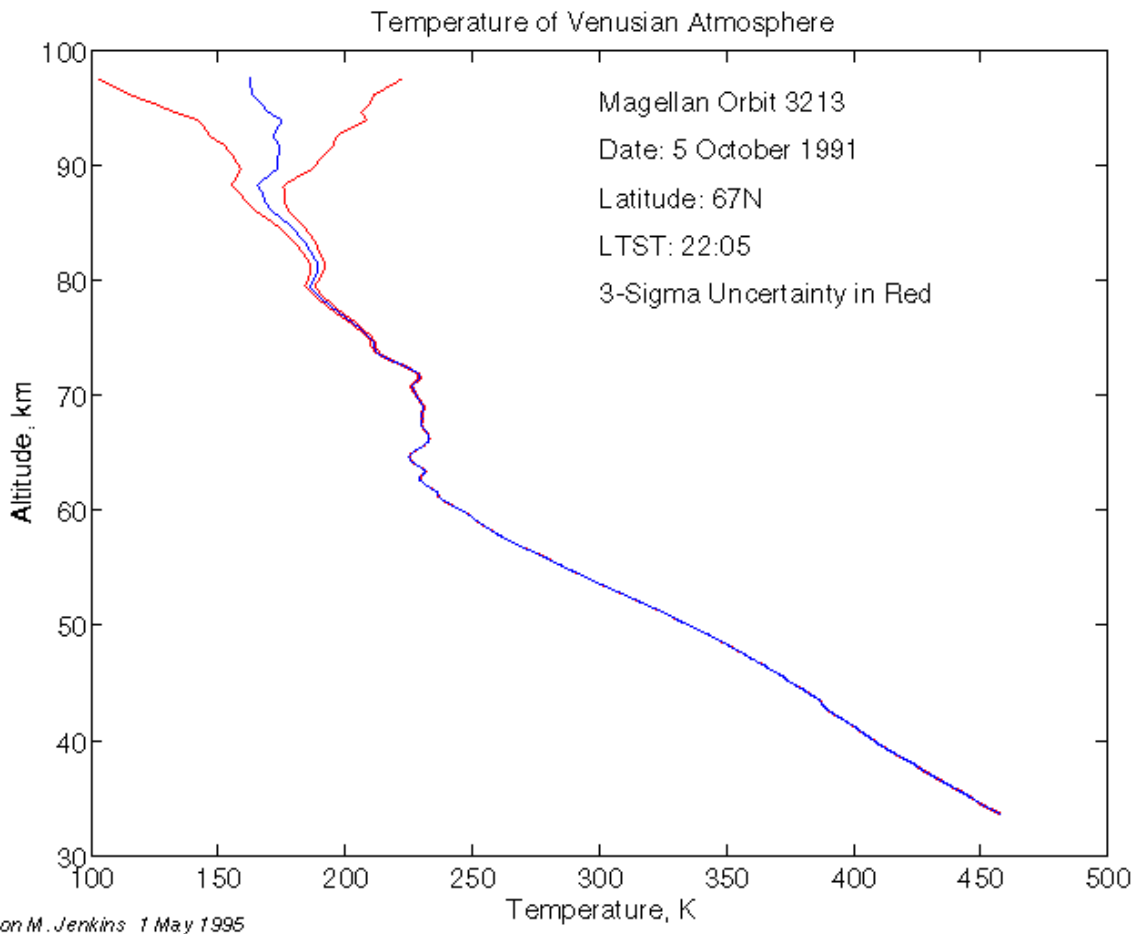


Figure 4-2: Temperature profile of Venus's atmosphere

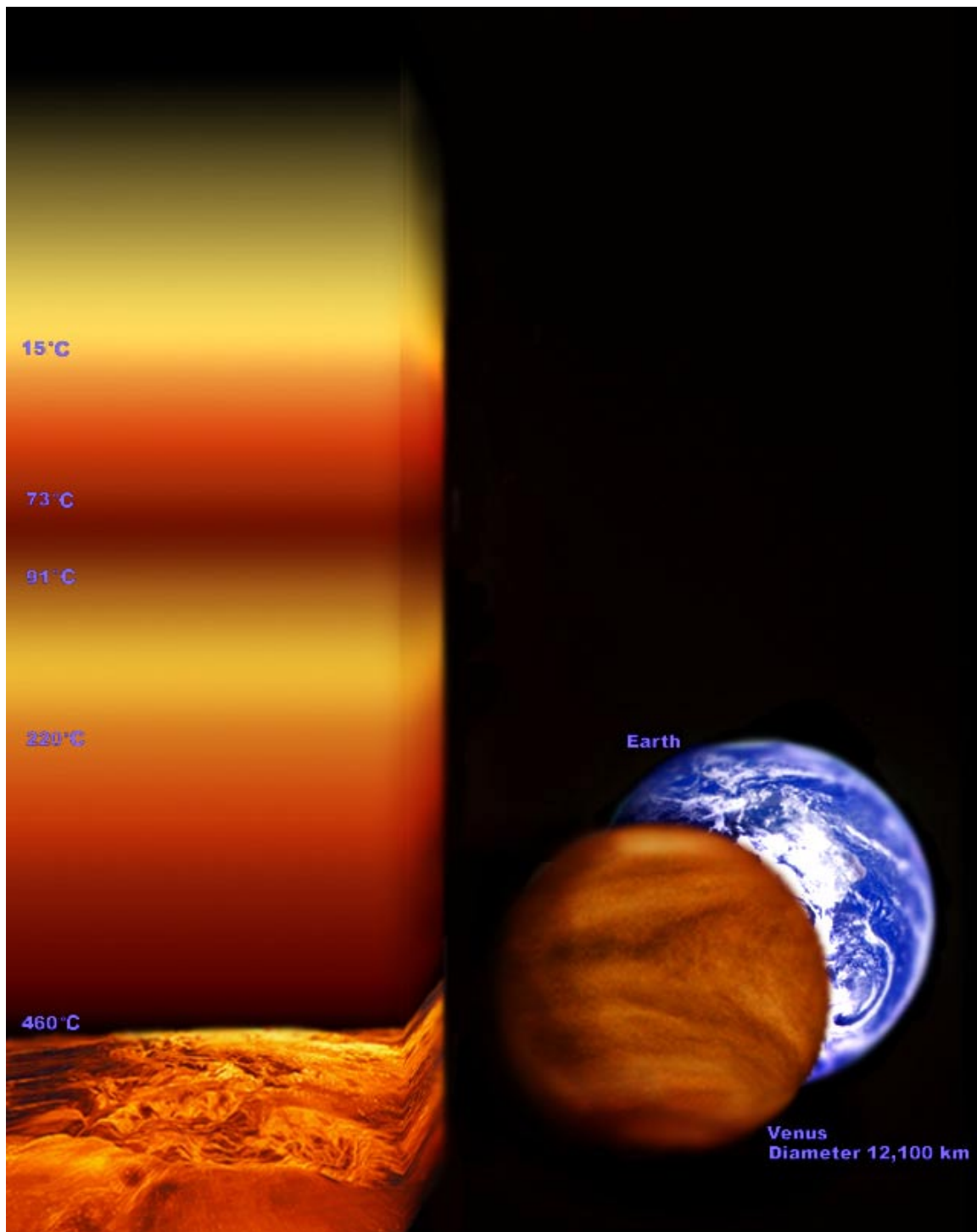


Figure 4-3: Temperature profile within Venus's atmosphere

Above this cloud layer is an abundant amount of solar energy. The solar flux at the orbit of Venus is $2,600 \text{ W/m}^2$, which is much greater than the $1,360 \text{ W/m}^2$ available in Earth's orbit. This nearly 100% increase in solar flux can double the performance of the aircraft. Even within the cloud layer, there may be sufficient solar energy to operate aircraft. At the bottom of the

cloud layer (45 km altitude) the solar intensity is between 520 W/m^2 and $1,300 \text{ W/m}^2$, depending on the wavelength of the radiation being collected. This is comparable to the solar intensity for Mars or Earth. Even within the cloud layer, therefore, the ability to fly under solar power on Venus will be no worse than it is to fly on Earth or Mars. And flying above the cloud layer will produce a much more capable aircraft than flying at similar pressure altitudes on Earth or Mars. [8]

Another unique aspect of Venus is that the day length is longer than the year. Due to this slow rotational rate, the speed to remain over a point on the surface is very low, approximately 13.4 km/hr. Therefore, it is conceivable that a solar powered aircraft could remain within the sunlit portion of the planet indefinitely. Overcoming the wind will be the key to maintaining the aircraft's position within the sunlit portion of the planet. The wind speed reaches about 95 m/s near the top of the cloud layer (64 km above the surface). The gravitational acceleration on Venus (8.87 m/s^2) is slightly less than that on Earth, which aids somewhat in the lifting capability of the aircraft. The atmospheric composition on Venus can also pose problems for the aircraft. The atmosphere is composed mostly of CO_2 but also has trace amounts of corrosive compounds, such as hydrochloric, hydrofluoric, and sulfuric acids. [8]

4.2.1 Physical Properties of Venus

Venus's average atmosphere characteristics as a function of altitude are shown in Table 4-1. [22]

Table 4-1: Physical properties of Venus

Inclination of equator to orbit	3.39°
Orbital eccentricity	0.0067
Day period	243 (Earth days)
Solar radiation intensity	Mean: $2,613.9 \text{ W/m}^2$ Parihelion: $2,649 \text{ W/m}^2$ Aphelion: $2,579 \text{ W/m}^2$
Albedo	0.65
Gravitational constant	8.87 m/s^2
Sidereal year	224 (Earth days)
Surface temperature	737° K
Diameter	12,104 km

4.2.2 Atmospheric Conditions of Venus

The atmosphere on Venus is very thick and extends upwards from the surface for hundreds of kilometers. The winds within the atmosphere blow fairly consistently in the same direction as the planetary rotation (east to west) over all latitudes and altitudes up to 100 km. Above 100 km the winds shift to blow from the day side of the planet to the night side. The wind speeds decrease as a function of altitude from $\sim 100 \text{ m/s}$ at the cloud tops (60 km) to $\sim 0.5 \text{ m/s}$ at the sur-

face. These high wind speeds and the slow rotation of the planet produce a super-rotation of the atmosphere (nearly 60 times faster than the surface). [22]

Table 4-2: Venus atmospheric composition

Gas	Percent Volume
Carbon Dioxide (CO ₂)	96.5
Nitrogen (N ₂)	3.5
Sulfur Dioxide (SO ₂)	150 ppm
Carbon Monoxide (CO)	17 ppm
Water Vapor (H ₂ O)	20 ppm
Neon (Ne)	7 ppm
Argon (Ar)	70 ppm
Helium	17 ppm

[7]

4.2.2.1 Mean Standard Atmosphere for Venus (JPL Model)

Table 4-3: Venus atmospheric properties with altitude

H K m	T K	P (bar)	ρ kg/m ³	U m/s	μ Pa*s	v s/m ²	Cp J/kg*K	Cp/ Cv	A m/s	K W/m*K
0	735.3	92.1	64.79	0.6	3.35E-05	5.17E-07	1181	1.193	410	0.0588
1	727.7	86.45	61.56	0.7	3.12E-05	5.07E-07	1177	1.194	408	0.0575
2	720.2	81.09	58.45	0.8	2.89E-05	4.95E-07	1172	1.195	406	0.0561
3	712.4	76.01	55.47	0.9	2.67E-05	4.81E-07	1168	1.196	404	0.0548
4	704.6	71.2	52.62	1.0	2.44E-05	4.63E-07	1163	1.197	402	0.0534
5	696.8	66.65	49.87	1.2	2.21E-05	4.43E-07	1159	1.198	400	0.0521
6	688.8	62.35	47.24	1.3	2.18E-05	4.62E-07	1155	1.199	398	0.0511
7	681.1	58.28	44.71	1.9	2.16E-05	4.83E-07	1151	1.200	396	0.0501
8	673.6	54.44	42.26	2.4	2.13E-05	5.04E-07	1146	1.200	393	0.0490
9	665.8	50.81	39.95	3.4	2.11E-05	5.27E-07	1142	1.201	391	0.0480
10	658.2	47.39	37.72	4.5	2.08E-05	5.51E-07	1138	1.202	389	0.0470
11	650.6	44.16	35.58	6.3	2.25E-05	6.33E-07	1134	1.203	387	0.0462
12	643.2	41.12	33.54	8.2	2.42E-05	7.23E-07	1129	1.204	385	0.0455
13	635.5	38.26	31.6	10.8	2.60E-05	8.22E-07	1125	1.205	383	0.0447
14	628.1	35.57	29.74	13.4	2.77E-05	9.31E-07	1120	1.206	381	0.0440

Table 4-3: Venus atmospheric properties with altitude (Continued)

H K m	T K	P (bar)	ρ kg/m ³	U m/s	μ Pa*s	ν s/m ²	Cp J/kg*K	Cp/ Cv	A m/s	K W/m*K
15	620.8	33.04	27.95	16.1	2.94E-05	1.05E-06	1116	1.207	379	0.0432
16	613.3	30.66	26.271	19.6	2.91E-05	1.11E-06	1111	1.208	377	0.0425
17	605.2	28.43	24.68	22.0	2.88E-05	1.17E-06	1106	1.209	374	0.0417
18	597.1	26.33	23.18	24.5	2.84E-05	1.23E-06	1101	1.211	372	0.0410
19	589.3	24.36	21.74	26.0	2.81E-05	1.29E-06	1096	1.212	369	0.0402
20	580.7	22.52	20.39	27.6	2.78E-05	1.36E-06	1091	1.213	367	0.0395
21	572.4	20.79	19.11	28.8	2.76E-05	1.44E-06	1085	1.214	365	0.0388
22	564.3	19.17	17.88	29.9	2.74E-05	1.53E-06	1079	1.216	362	0.0382
23	556.0	17.66	16.71	30.6	2.71E-05	1.62E-06	1074	1.217	360	0.0375
24	547.5	16.25	15.62	31.3	2.69E-05	1.72E-06	1068	1.219	357	0.0369
25	539.2	14.93	14.57	32.3	2.67E-05	1.83E-06	1062	1.220	355	0.0362
26	530.7	13.7	13.59	33.3	2.64E-05	1.94E-06	1056	1.222	352	0.0357
27	522.3	12.56	12.65	34.0	2.61E-05	2.06E-06	1049	1.223	350	0.0352
28	513.8	11.49	11.77	34.6	2.58E-05	2.19E-06	1043	1.225	347	0.0346
29	505.6	10.5	10.93	35.0	2.55E-05	2.33E-06	1036	1.226	345	0.0341
30	496.9	9.851	10.15	35.5	2.52E-05	2.48E-06	1030	1.228	342	0.0336
31	488.3	8.729	9.406	36.0	2.49E-05	2.65E-06	1023	1.230	339	0.0331
32	479.9	7.94	8.704	36.4	2.46E-05	2.83E-06	1016	1.232	337	0.0325
33	472.7	7.211	8.041	36.7	2.44E-05	3.03E-06	1010	1.234	334	0.0320
34	463.4	6.537	7.42	36.9	2.41E-05	3.25E-06	1003	1.236	332	0.0314
35	455.5	5.917	6.831	37.3	2.38E-05	3.48E-06	996	1.238	329	0.0309
36	448.0	5.346	6.274	37.6	2.35E-05	3.75E-06	990	1.240	326	0.0304
37	439.9	4.822	5.762	38.2	2.33E-05	4.04E-06	983	1.242	324	0.0300
38	432.5	4.342	5.276	38.7	2.30E-05	4.36E-06	977	1.244	321	0.0295
39	425.1	3.903	4.823	39.7	2.28E-05	4.72E-06	970	1.246	319	0.0291
40	417.6	3.501	4.404	40.7	2.25E-05	5.11E-06	964	1.248	316	0.0286
41	410.0	3.135	4.015	42.6	2.23E-05	5.55E-06	958	1.250	314	0.0282
42	403.5	2.802	3.646	44.5	2.21E-05	6.05E-06	953	1.252	311	0.0277
43	397.1	2.499	3.303	47.4	2.18E-05	6.61E-06	947	1.253	309	0.0273
44	391.2	2.226	2.985	50.3	2.16E-05	7.24E-06	942	1.255	306	0.0268

Table 4-3: Venus atmospheric properties with altitude (Continued)

H K m	T K	P (bar)	ρ kg/m³	U m/s	μ Pa*s	ν s/m²	Cp J/kg*K	Cp/ Cv	A m/s	K W/m*K
45	385.4	1.979	2.693	54.2	2.14E-05	7.95E-06	936	1.257	304	0.0264
46	379.7	1.756	2.426	57.4	2.11E-05	8.71E-06	930	1.259	302	0.0260
47	373.1	1.556	2.186	59.4	2.09E-05	9.55E-06	923	1.261	299	0.0256
48	366.4	1.375	1.967	61.0	2.06E-05	1.05E-05	917	1.264	297	0.0251
49	358.6	1.213	1.769	61.2	2.04E-05	1.15E-05	910	1.266	294	0.0247
50	350.5	1.066	1.594	60.9	2.01E-05	1.26E-05	904	1.268	292	0.0243
51	342.0	0.9347	1.432	60.2	1.97E-05	1.38E-05	895	1.272	288	0.0239
52	333.3	0.8167	1.284	59.4	1.94E-05	1.51E-05	886	1.276	284	0.0235
53	323.0	0.7109	1.153	59.3	1.90E-05	1.65E-05	877	1.279	281	0.0231
54	312.8	0.616	1.032	59.2	1.87E-05	1.81E-05	868	1.283	277	0.0227
55	302.3	0.5314	9207	59.9	1.83E-05	1.99E-05	859	1.287	273	0.0223
56	291.8	0.4559	0.8183	60.5	1.80E-05	2.20E-05	851	1.290	270	0.0219
57	282.5	0.3891	0.7212	62.7	1.77E-05	2.45E-05	844	1.294	266	0.0215
58	275.2	0.3306	0.6289	65.0	1.73E-05	2.76E-05	836	1.297	263	0.0212
59	268.7	0.2796	0.5448	71.1	1.70E-05	3.12E-05	829	1.301	259	0.0208
60	262.8	0.2357	0.4694	77.2	1.67E-05	3.56E-05	821	1.304	256	0.0204
61	258.7	0.2008	0.40525	85.4	1.66E-05	4.09E-05	818	1.306	255	0.0201
62	254.5	0.1659	0.3411	92.0	1.64E-05	4.82E-05	815	1.307	253	0.0197
63	250.0	0.14075	0.2927	94.0	1.63E-05	5.57E-05	811	1.309	252	0.0194
64	245.4	0.1156	0.2443	94.5	1.62E-05	6.62E-05	808	1.310	250	0.0190
65	243.2	0.09765	0.2086	95.0	1.61E-05	7.69E-05	805	1.312	249	0.0187
66	241.0	0.0797	0.1729	94.4	1.59E-05	9.21E-05	802	1.314	247	0.0184
67	238.2	0.06709	0.14695	93.8	1.58E-05	1.07E-04	799	1.315	246	0.0180
68	235.4	0.05447	0.121	93.2	1.57E-05	1.29E-04	795	1.317	244	0.0177
69	232.6	0.04569	0.102465	92.6	1.55E-05	1.52E-04	792	1.318	243	0.0173
70	229.8	0.0369	0.08393	92.0	1.54E-05	1.83E-04	789	1.320	241	0.0170
71	227.0	0.03083	0.07084	89.4	1.53E-05	2.15E-04	786	1.322	239	0.0167
72	224.1	0.02476	0.05775	86.8	1.51E-05	2.61E-04	783	1.324	238	0.0164
73	221.4	0.02061	0.04854	84.2	1.50E-05	3.08E-04	779	1.325	236	0.0161
74	218.6	0.01645	0.03933	81.6	1.48E-05	3.76E-04	776	1.327	235	0.0158

Table 4-3: Venus atmospheric properties with altitude (Continued)

H K m	T K	P (bar)	ρ kg/m ³	U m/s	μ Pa*s	ν s/m ²	Cp J/kg*K	Cp/ Cv	A m/s	K W/m*K
75	215.4	0.01363	0.03298	79.0	1.47E-05	4.44E-04	773	1.329	233	0.0155
76	212.1	0.01081	0.02663	74.6	1.45E-05	5.44E-04	770	1.331	231	0.0151
77	208.7	0.00891	0.022235	70.2	1.44E-05	6.45E-04	767	1.333	230	0.0148
78	205.3	0.00701	0.01784	65.8	1.42E-05	7.96E-04	763	1.334	228	0.0145
79	201.2	0.00589	0.01485	61.4	1.41E-05	9.46E-04	760	1.336	227	0.0142
80	197.1	0.00476	0.01186	57.0	1.39E-05	1.17E-03	757	1.338	225	0.0139
81	193.5	0.00378	0.009793	52.4	1.38E-05	1.41E-03	755	1.340	223	0.0138
82	189.9	0.00281	0.007725	47.8	1.36E-05	1.77E-03	752	1.341	222	0.0136
83	186.9	0.00227	0.006326	43.2	1.35E-05	2.14E-03	750	1.343	220	0.0135
84	183.8	0.00173	0.004926	38.6	1.34E-05	2.72E-03	747	1.344	219	0.0133
85	181.0	0.00139	0.004007	34.0	1.33E-05	3.31E-03	745	1.346	217	0.0132
86	178.2	0.00105	0.003088	30.4	1.31E-05	4.25E-03	743	1.347	215	0.0131
87	175.9	0.00084	0.002493	26.8	1.30E-05	5.21E-03	740	1.349	214	0.0129
88	173.6	0.00063	0.001898	23.2	1.29E-05	6.78E-03	738	1.350	212	0.0128
89	171.5	0.0005	0.001525	19.6	1.27E-05	8.35E-03	735	1.352	211	0.0126
90	169.4	0.00037	0.001151	16.0	1.26E-05	1.09E-02	733	1.353	209	0.0125
91	168.3	0.0003	0.000917	15.0	1.26E-05	1.38E-02	734	1.353	209	0.0125
92	167.2	0.00022	0.000684	14.0	1.27E-05	1.85E-02	734	1.353	210	0.0126
93	167.2	0.00017	0.000542	13.0	1.27E-05	2.34E-02	735	1.353	210	0.0126
94	167.2	0.00013	0.0004	12.0	1.27E-05	3.18E-02	735	1.353	211	0.0126
95	168.2	0.0001	0.000315	11.0	1.28E-05	4.04E-02	736	1.353	211	0.0127
96	169.2	7.5E-05	0.000231	10.8	1.28E-05	5.52E-02	736	1.352	211	0.0127
97	170.6	6E-05	0.000183	10.6	1.28E-05	7.00E-02	737	1.352	212	0.0127
98	172.0	4.5E-05	0.000135	10.4	1.28E-05	9.53E-02	737	1.352	212	0.0127
99	173.7	3.6E-05	0.000107	10.2	1.29E-05	1.21E-01	738	1.352	213	0.0128
100	175.4	2.7E-05	7.89E-05	10.0	1.29E-05	1.63E-01	738	1.352	213	0.0128

4.3 Environmental Conditions for Flight on Earth

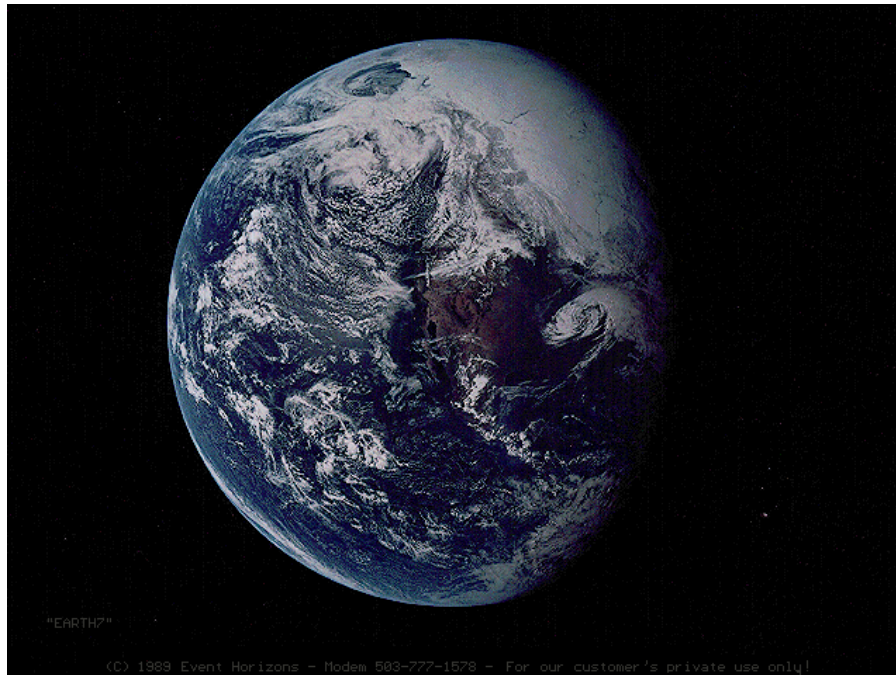


Figure 4-4: Earth

4.3.1 Physical Properties of Earth

Table 4-4: Physical properties of Earth

Inclination of equator to orbit	23.45°
Orbital eccentricity	0.01673
Day period	23 h, 57.8 m
Solar radiation intensity	Mean: 1,352 W/m ² Perihelion: 1,399 W/m ² Aphelion: 1,307 W/m ²
Albedo	0.37
Gravitational constant	9.81 m/s ²
Sidereal year	365.26 (Earth Days)
Surface temperature extremes	130° K to 300° K
Diameter	12,756 km

4.3.2 Atmospheric Conditions of Earth

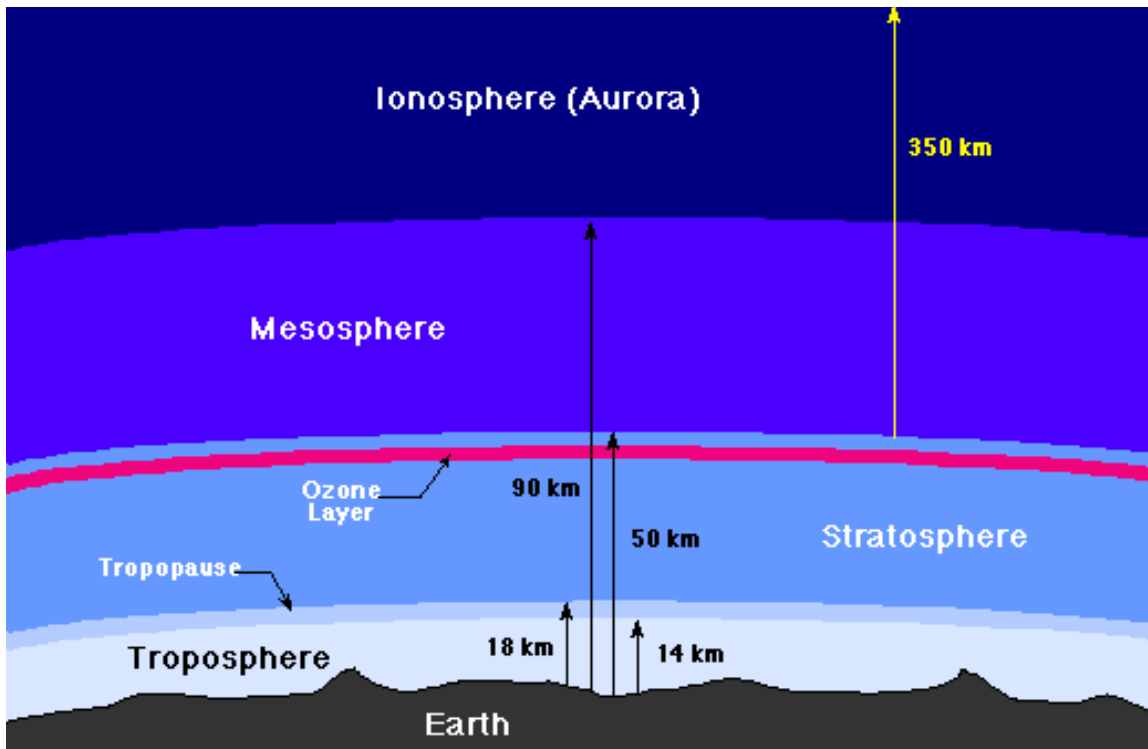


Figure 4-5: Profile of Earth's atmosphere

Earth's atmosphere is broken down into layers, as shown in Figure 4-5. The layers of interest for the SSA are the troposphere (from the surface to approximately 14 km), the tropopause (from ~14 km to ~18 km), and the lowest third of the stratosphere (~18 km to ~30 km). The *troposphere* is the region in the atmosphere where all the active weather occurs. Air rises and falls due to heating and ground effects, causing winds and weather patterns. The majority of cloud formations and the atmosphere as we see it occur in the troposphere, Figure 4-6. There is a gradual change from troposphere to the stratosphere that begins at approximately 14 km high. This is called the *tropopause*. The temperature in the lower stratosphere is extremely stable and cold at -57°C . Here, strong winds occur as part of defined circulation patterns and are mostly horizontal with little mixing. High cirrus clouds sometimes form in the stratosphere, but for the most part there are no significant weather patterns in the stratosphere.



Figure 4-6: Troposphere

The wind speed on Earth is highly variable, depending on the location, time of year, and altitude. Mean wind profiles are shown for two locations (Albuquerque, New Mexico, and Cape

Kennedy, Florida) throughout the year in Figures 4-7 and 4-8. Although the absolute value of the wind speed will vary, the trends with altitude are similar for most locations.

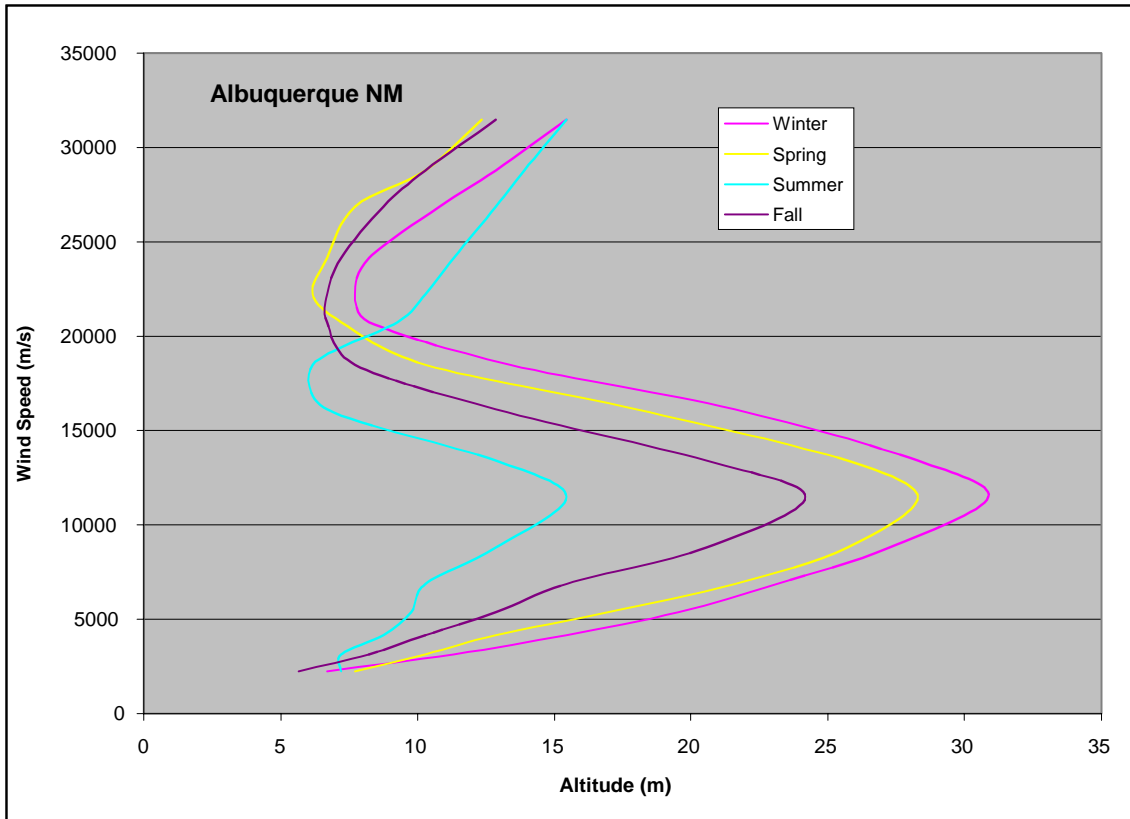


Figure 4-7: Mean wind speeds for Albuquerque, New Mexico

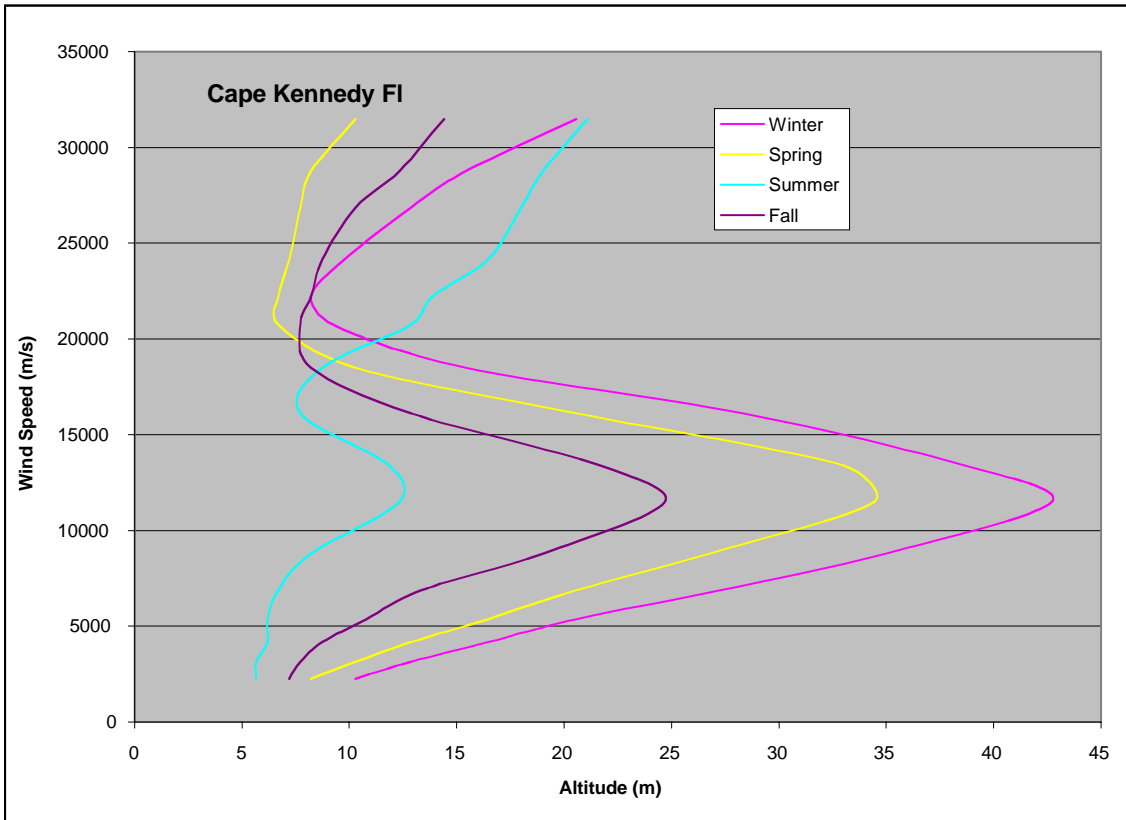


Figure 4-8: Mean wind speeds for Cape Kennedy, Florida

The Earth standard atmosphere table is based on idealized year-round conditions at 45° N latitude. The ideal gas constant for the Earth’s atmosphere is 8.31432 J/mol°K. The viscosity and thermal conductivity of the atmosphere are based on temperature and can be approximated by the following equations: [6]

Viscosity in (kg/m s)
$$\mu = \frac{(1.458E-7)T^{1.5}}{T+110.4}$$
 Equation 4-1

Thermal conductivity in (kcal m s °K)
$$k = \frac{(6.325E-7)T^{1.5}}{T+245.4 \times 10^{\left(\frac{-12}{T}\right)}}$$
 Equation 4-2

The atmospheric composition is given in Table 4-5.

Table 4-5: Major gas components of Earth’s atmosphere

Gas	Percent Volume
Nitrogen (N ₂)	78.084
Oxygen (O ₂)	20.947

Table 4-5: Major gas components of Earth's atmosphere (Continued)

Gas	Percent Volume
Argon (Ar)	0.934
Carbon Dioxide (CO ₂)	0.0314
Neon (Ne)	0.00181
Helium (He)	0.000524

4.3.3 Earth Standard Atmosphere [6]

Table 4-6: Earth standard atmosphere

Altitude (m)	Temp. °K	Pressure mBar	Density (kg/m ³)	Speed of Sound (m/s)	Viscosity (Kg/m s)	Conductivity (kcal m s °K)
0	288.15	1013.3	1.225	340.3	1.789E-5	0.6053E-5
200	286.85	989.5	1.202	339.5	1.783E-5	0.6029E-5
400	285.55	966.1	1.179	338.8	1.777E-5	0.6004E-5
600	284.25	943.2	1.156	338.0	1.771E-5	0.5980E-5
800	282.95	920.8	1.134	337.2	1.764E-5	0.5955E-5
1,000	281.65	898.8	1.112	336.4	1.758E-5	0.5931E-5
1,200	280.35	877.2	1.090	335.7	1.752E-5	0.5906E-5
1,400	279.05	856.0	1.069	334.9	1.745E-5	0.5881E-5
1,600	277.75	835.3	1.048	334.1	1.739E-5	0.5857E-5
1,800	276.45	814.9	1.027	333.3	1.732E-5	0.5832E-5
2,000	275.15	795.0	1.007	332.5	1.726E-5	0.5807E-5
2,200	273.86	775.5	0.987	331.7	1.720E-5	0.5784E-5
2,400	272.56	756.3	0.967	331.0	1.713E-5	0.5759E-5
2,600	271.26	737.6	0.947	330.2	1.707E-5	0.5733E-5
2,800	269.96	719.2	0.928	329.4	1.700E-5	0.5708E-5
3,000	268.66	701.2	0.909	328.6	1.694E-5	0.5683E-5
3,200	267.36	683.6	0.891	327.8	1.687E-5	0.5658E-5
3,400	266.06	666.3	0.872	327.0	1.681E-5	0.5634E-5
3,600	264.76	649.4	0.854	326.2	1.674E-5	0.5609E-5

Table 4-6: Earth standard atmosphere (Continued)

Altitude (m)	Temp. °K	Pressure mBar	Density (kg/m ³)	Speed of Sound (m/s)	Viscosity (Kg/m s)	Conductivity (kcal m s °K)
3,800	263.47	632.8	0.837	325.4	1.668E-5	0.5584E-5
4,000	262.17	616.6	0.819	324.6	1.661E-5	0.5559E-5
4,200	260.87	600.7	0.802	323.8	1.655E-5	0.5534E-5
4,400	259.57	585.2	0.785	323.0	1.648E-5	0.5508E-5
4,600	258.27	570.0	0.769	322.2	1.642E-5	0.5483E-5
4,800	256.97	555.1	0.752	321.4	1.635E-5	0.5458E-5
5,000	255.68	540.5	0.736	320.5	1.628E-5	0.5433E-5
5,200	254.38	526.2	0.721	319.7	1.622E-5	0.5408E-5
5,400	253.08	512.3	0.705	318.9	1.615E-5	0.5383E-5
5,600	251.78	498.6	0.690	318.1	1.608E-5	0.5357E-5
5,800	250.48	485.2	0.675	317.3	1.602E-5	0.5332E-5
6,000	249.191	472.2	0.660	316.5	1.595E-5	0.5307E-5
6,200	247.89	459.4	0.646	315.6	1.588E-5	0.5282E-5
6,400	246.59	446.9	0.631	314.8	1.582E-5	0.5256E-5
6,600	245.29	434.7	0.617	314.0	1.575E-5	0.5231E-5
6,800	244.00	422.7	0.604	313.1	1.568E-5	0.5205E-5
7,000	242.70	411.1	0.590	312.3	1.561E-5	0.5180E-5
7,500	239.46	383.0	0.572	310.2	1.544E-5	0.5116E-5
8,000	236.22	356.5	0.526	308.1	1.527E-5	0.5052E-5
8,500	232.97	331.6	0.496	306.0	1.510E-5	0.4988E-5
9,000	229.73	308.0	0.467	303.8	1.493E-5	0.4924E-5
9,500	226.49	285.8	0.440	301.7	1.475E-5	0.4859E-5
10,000	223.25	265.0	0.414	299.5	1.458E-5	0.4794E-5
11,000	216.77	227.0	0.365	295.2	1.422E-5	0.4664E-5
12,000	216.65	194.0	0.312	295.1	1.422E-5	0.4664E-5
13,000	216.65	165.8	0.267	295.1	1.422E-5	0.4664E-5
14,000	216.65	141.7	0.228	295.1	1.422E-5	0.4664E-5
15,000	216.65	121.1	0.195	295.1	1.422E-5	0.4664E-5

Table 4-6: Earth standard atmosphere (Continued)

Altitude (m)	Temp. °K	Pressure mBar	Density (kg/m ³)	Speed of Sound (m/s)	Viscosity (Kg/m s)	Conductivity (kcal m s °K)
16,000	216.65	103.5	0.166	295.1	1.422E-5	0.4664E-5
17,000	216.65	88.5	0.142	295.1	1.422E-5	0.4664E-5
18,000	216.65	75.7	0.122	295.1	1.422E-5	0.4664E-5
19,000	216.65	64.7	0.104	295.1	1.422E-5	0.4664E-5
20,000	216.65	55.3	0.0889	295.1	1.422E-5	0.4664E-5
22,000	218.57	40.5	0.0645	296.4	1.433E-5	0.4702E-5
24,000	220.56	29.7	0.0469	297.8	1.444E-5	0.4742E-5
26,000	222.54	21.9	0.0343	299.1	1.454E-5	0.4782E-5
28,000	224.53	16.2	0.0251	300.4	1.465E-5	0.4820E-5
30,000	226.51	12.0	0.0184	301.7	1.475E-5	0.4859E-5
35,000	236.51	5.75	0.0085	308.3	1.529E-5	0.5058E-5
40,000	250.35	2.87	0.0040	317.2	1.601E-5	0.5330E-5
50,000	270.65	.798	0.0010	329.8	1.704E-5	0.5721E-5
100,000	210.02	3e-4	5e-7	---	---	---

4.4 Environmental Conditions for Flight on Mars

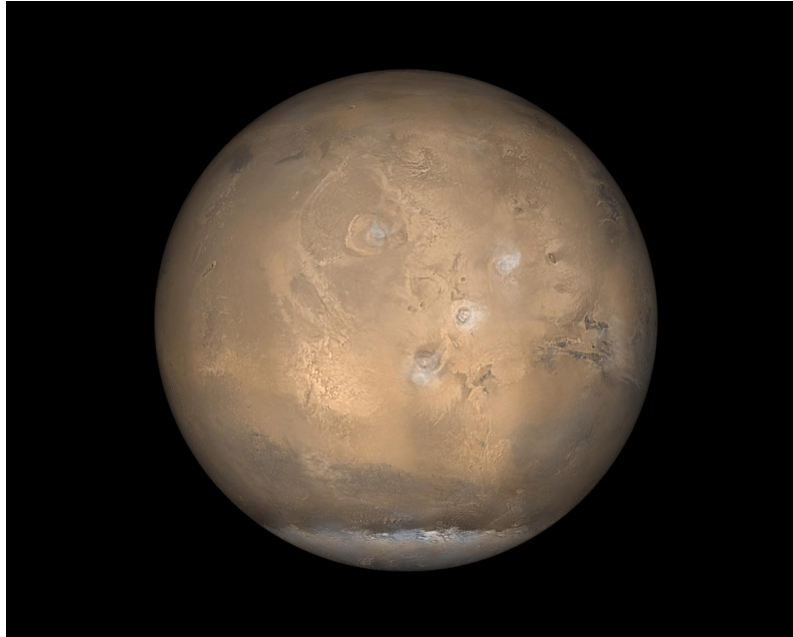


Figure 4-9: Mars

The Mars environment is very different from Earth's, so there are issues and concerns associated with operating a vehicle in that environment that are not encountered on Earth. Mars has an atmosphere (Figure 4-10), but it is very thin. Near the surface on Mars the atmospheric density is similar to the density of Earth's atmosphere at 30 km. The atmosphere is made up almost entirely of carbon dioxide. The temperature on Mars is on average much colder than on Earth. Although at certain times of the year and locations the temperature will rise above freezing, most of the time temperatures are well below the freezing point of water. The gravitational force on Mars is about a third of what it is on Earth. Therefore, the lift that the SSA would need to generate to carry a given amount of mass is only a third of what it would need to be on Earth. This reduced gravity and consequent lower lift requirement will greatly benefit operation of the aircraft. However, the environmental conditions on Mars are not all beneficial. The low atmospheric density means that the SSA will be flying in a very low Reynolds number flight regime. There are a number of aerodynamic concerns with flight at very low Reynolds numbers. Most of these are based on flow separation which can affect the aircraft's stability, control, and lift generation.



Figure 4-10: Image of Mars atmosphere taken from Pathfinder Lander

Other environmental characteristics important to the system's design include the surface temperature, atmospheric dust, solar intensity, soil and atmospheric composition, and terrain characteristics (Figures 4-11 and 4-12). These factors influence just about every aspect of the SSA's operation and potential mission capabilities. Some of these operational issues include what latitudes can the vehicle fly at and at what times during the year, can the vehicle land and be operational on the surface, the type and capabilities of the communications system, the type and approach for the navigation and control system, the construction materials used in the vehicle, and landing and sampling approach.

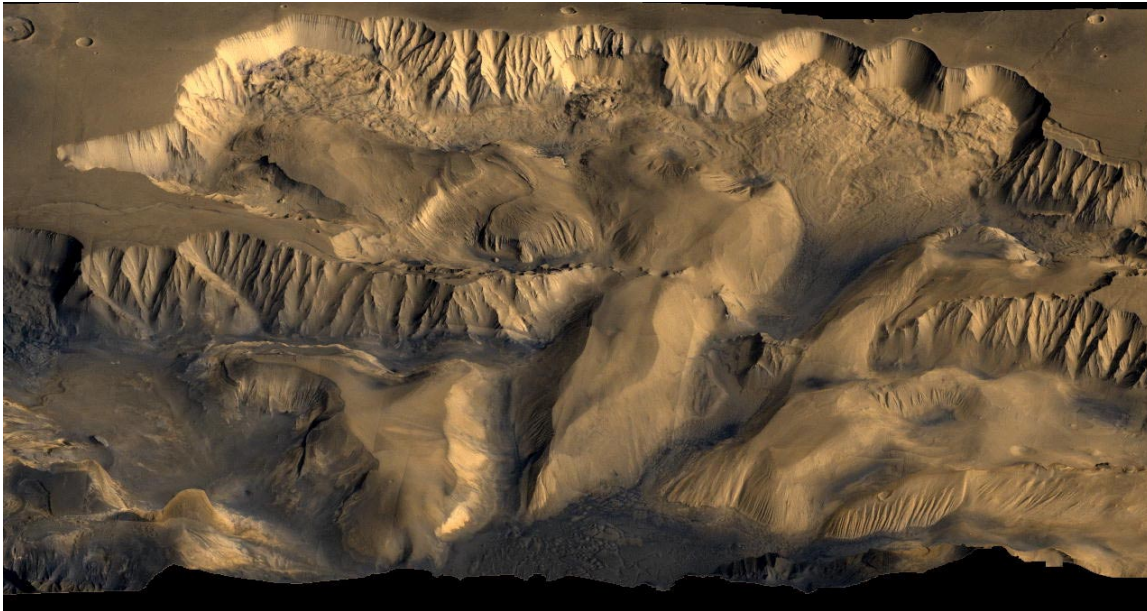


Figure 4-11: Orbital image of surface features on Mars



Figure 4-12: Image of Mars surface from Pathfinder Lander

As a basis for investigating the SSA's applicability and capabilities on Mars, a concise summary of the Mars environmental conditions was assembled. Some of the more recent Mars science missions (particularly the Pathfinder mission) have provided detailed information on various aspects of the Mars environment. However, many aspects of the Mars environment are still not well understood. The information provided in the following tables and figures represent the present state of knowledge of the Mars environment. This information and the influence it has on the SSA design may be subject to change as our understanding of the environment of Mars increases.

4.4.1 Physical Properties on Mars

Table 4-7: Physical properties of Mars

Inclination of equator to orbit	25.2°
Orbital eccentricity	0.093
Day period	24 h 39 m
Solar radiation intensity	Mean: 590 W/m ² Parihelion: 718 W/m ² Aphelion: 493 W/m ²
Albedo	0.15
Gravitational constant	3.73 m/s ²
Sidereal year	687 days (Martian)
Surface temperature extremes	130° K to 300° K
Diameter	6,794 km

4.4.2 Atmospheric Conditions on Mars [22]

Table 4-8: Mars atmospheric composition

Gas	Percent Volume
Carbon dioxide (CO ₂)	95.32
Nitrogen (N ₂)	2.7
Argon (Ar)	1.6
Oxygen (O ₂)	0.13
Carbon monoxide (CO)	0.07
Water vapor (H ₂ O)	0.03
Neon (Ne)	2.5 ppm
Krypton (Kr)	0.3 ppm
Xenon (Xe)	0.08 ppm

Mars atmospheric profiles are listed in Section 4.4.4, starting on Page 66. These tables consist of four atmospheric profiles generated by different sources and locations on Mars. The data available with each profile is not necessarily the same.

The first profile is a reference atmosphere supplied by JPL. [7] This data was generated for a latitude of -20°. It provides data on temperature, pressure, viscosity, and density from just above the surface to nearly 10 km².

The second profile is a general atmospheric model not specific to any location, generated to provide a rough estimate of the atmospheric conditions at any location on the planet. It provides density, temperature, pressure, and speed-of-sound data for elevations of -5 km (below the mean surface level) to 120 km above the surface [2].

The third profile was generated using the Mars-GRAM atmospheric simulation tool. This profile was generated for a specific location on Mars, Parana Valles (-25°, 11°). It contains information on density, temperature, pressure, speed of sound, and viscosity for altitudes of 2.38 km to 20 km. [3]

The fourth and last profile was also generated using the Mars-GRAM atmospheric simulation tool. This profile was generated for a specific location on Mars Utopia Planitia (57°, 235°). It contains information on density, temperature, pressure speed of sound and viscosity for altitudes of -1.74 km to 20 km. [3]

Significant data was also collected on the Mars atmosphere during the recent Pathfinder mission. For the first 30 days, surface pressure at the landing site underwent substantial daily variations of 0.2 to 0.3 mbar, associated primarily with the large thermal tides in the thin Mars atmosphere. Daily pressure cycles were characterized by a significant pressure change throughout the day period. This is shown in Figure 4-13, and the pressure change over a 30-day period is shown in Figure 4-14.

The near-surface temperature on Mars is greatly influenced by the surface temperature cycle, surface heating during the day and radiative cooling at night due to the low density of the Mars atmosphere. At sunrise, the atmosphere is typically stable, and cool, dense air lies near the surface. As the surface warms, the air mass is heated and by early morning begins to rise. As heating continues the atmosphere becomes unstable. This causes temperature fluctuations on the order of 15° K to 20° K, which are observed during the remainder of the morning and early afternoon. Later in the afternoon the surface cools, instability decreases, and temperature fluctuations reduce.

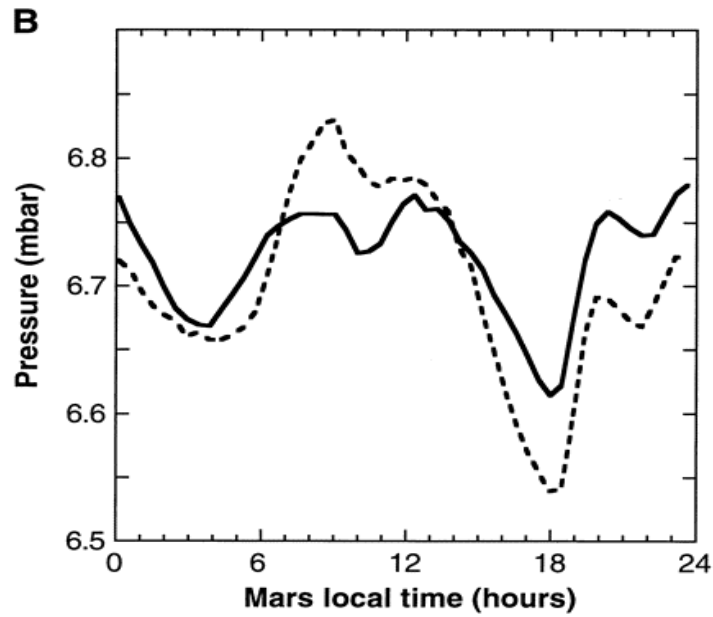


Figure 4-13: Daily pressure variation (Pathfinder data)
[14]

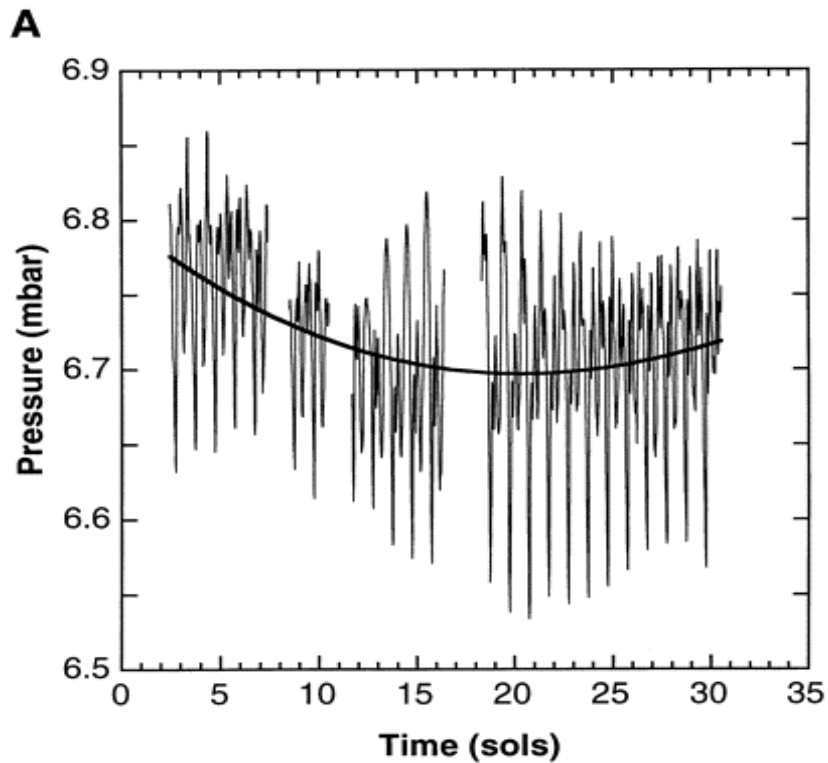


Figure 4-14: Pressure variation over a one-month period (Pathfinder data)
[14]

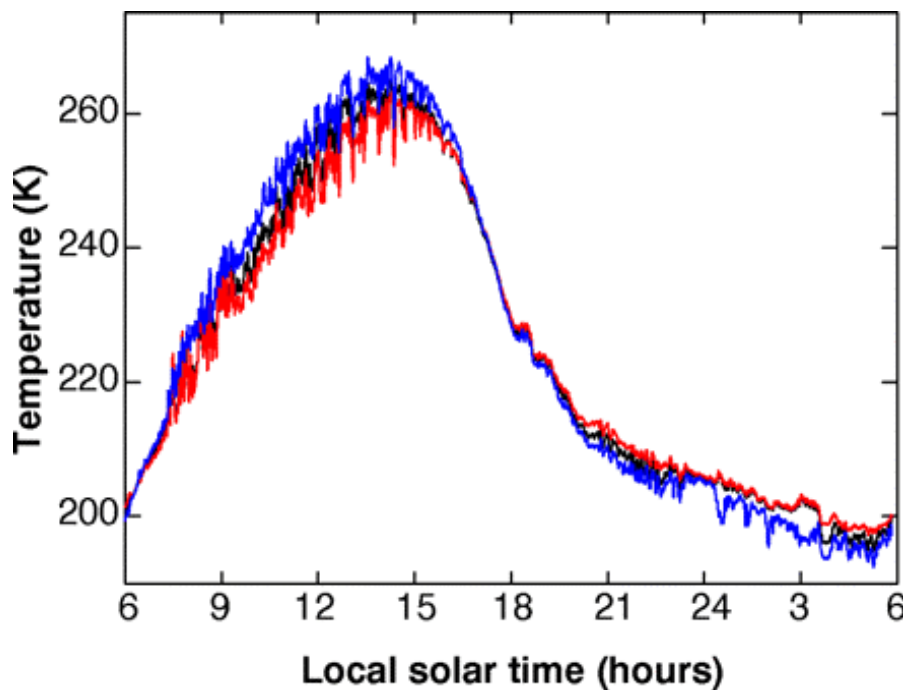


Figure 4-15: Atmospheric temperature variation throughout a day (Pathfinder data)
[14]

By evening, thermal convection subsides, and the instability in the atmosphere is diminished. The atmosphere becomes stable again due to surface cooling during the night. Any major nighttime temperature fluctuations are caused by downslope winds that disturb the surface-boundary layer.

4.4.3 Dust Storms and Wind

The wind at or near the surface can range from 2 m/s to 7 m/s, (based on Viking Lander data). These winds have a strong diurnal and seasonal variation in both direction and magnitude. Wind speeds of up to and possibly greater than 50 m/s will occur above the surface-boundary layer; this surface-boundary layer is estimated to extend tens of meters above the surface. Preliminary estimates of the Pathfinder wind data suggest that wind speeds were comparable with or lower than those measured by Viking Lander-1 at the same time of year. Speeds were generally less than 5 m/s to 10 m/s, except during the passage of dust devils, and were often less than 1 m/s in the morning hours. This may be consistent with the lower slope at the Pathfinder site. [14]

For a one-month period, Pathfinder data shows that wind direction generally rotated in a clockwise manner through a full 360°. Winds were consistently from the south in the late and early morning and then rotated steadily through west, north, and east during the day. The wind direction at night was very consistent but became more variable throughout the day. Wind direction is shown in Figure 4-16.

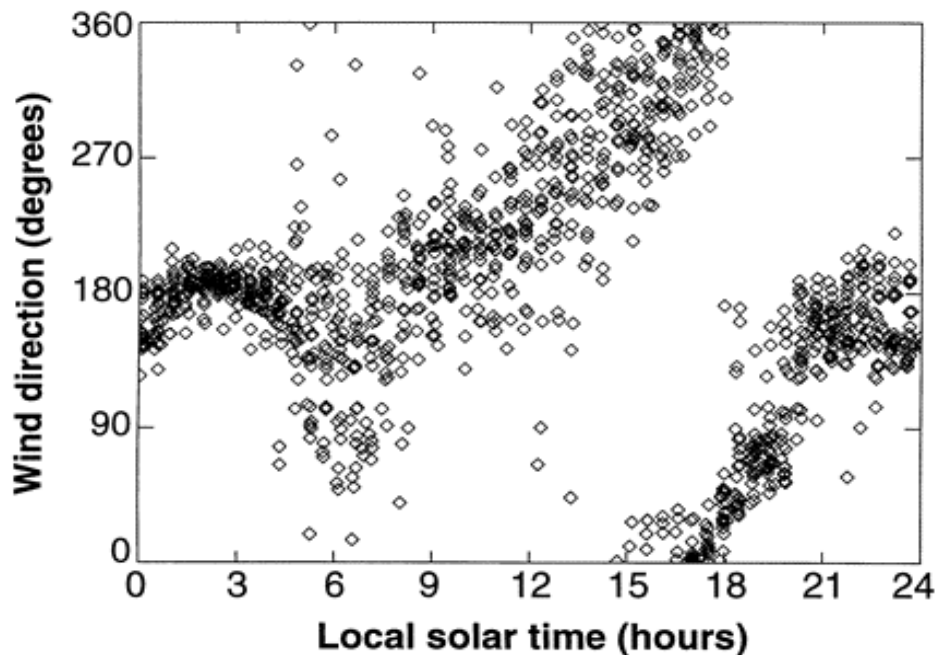


Figure 4-16: Wind direction throughout the day (Pathfinder data)

[14]

Dust storms tend to occur when Mars is near perihelion, when the solar intensity is the greatest. It is believed that the greater intensity of solar radiation, coupled with variations in the topology of Mars, triggers the dust storms. The storms can last up to several months, and their opacity can be quite high. Due to the low atmospheric density, these dust storms result in only minimal distribution and accumulation of debris. More information on dust storms, gathered for the Mars Micromission Aircraft Program is given in by Cruz [3].

Dust devils are short-term variations in measured surface pressure, wind velocity, and air temperature over periods of tens of seconds to minutes, shown in Figure 4-17. Dust devils, about 2 km wide and a few kilometers high, have been observed in the tropics by the Viking orbiters.

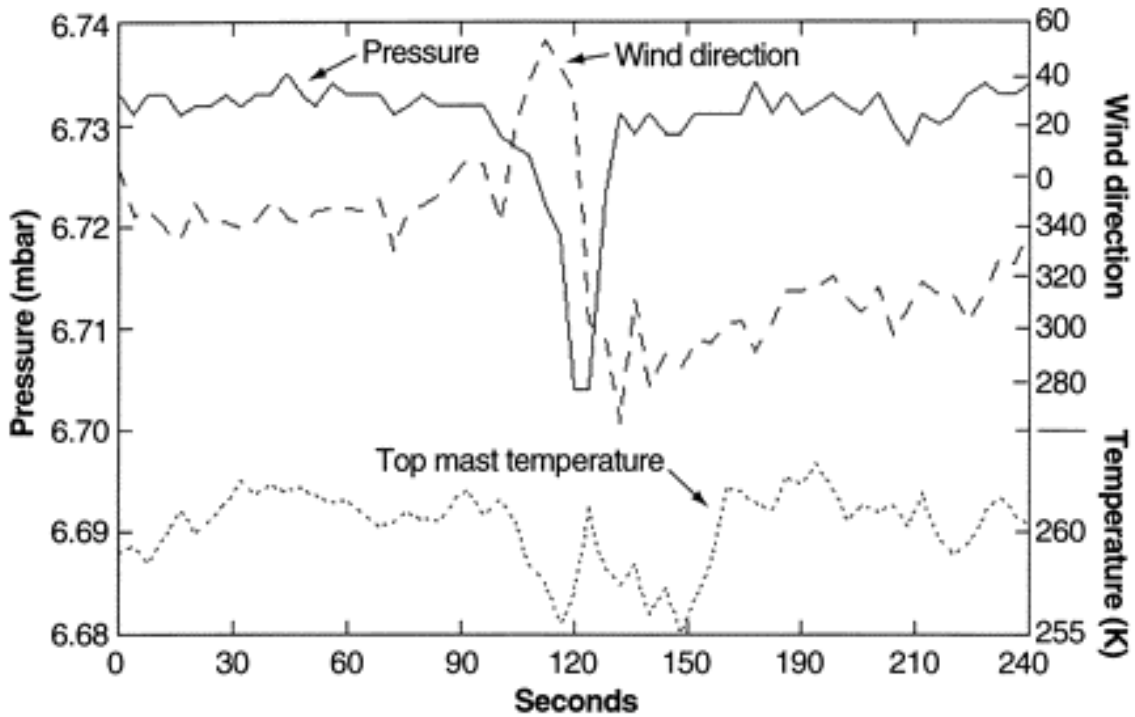


Figure 4-17: Measurements taken during a dust devil (Pathfinder data) [14]

4.4.4 Mars Atmosphere Data [7, 2, 3]

Table 4-9: JPL reference Mars atmosphere for -20° latitude

Mars Atmosphere Model

Lat = -20 coxZ 0.7
 Z,deg 41.9298101

H, km	T, K	P, Pa	ρ , g/m ³	μ , Pa*s	ν , m ² /s	1/ ν
9.8750	205	273.6	6.968	1.04E-05	0.00150	667
9.6250	206	280.2	7.100	1.05E-05	0.00148	677
9.3750	207	286.8	7.234	1.05E-05	0.00146	687
9.1250	208	293.6	7.369	1.06E-05	0.00144	696
8.8750	209	300.6	7.507	1.06E-05	0.00142	706
8.6250	209	307.6	7.683	1.06E-05	0.00138	723
8.3750	210	314.8	7.826	1.07E-05	0.00136	733
8.1250	211	322.2	7.970	1.07E-05	0.00135	743
7.8750	212	329.7	8.117	1.08E-05	0.00133	753

Table 4-9: JPL reference Mars atmosphere for -20° latitude (Continued)

Mars Atmosphere Model

Lat = -20 coxZ 0.7
 Z,deg 41.9298101

H, km	T, K	P, Pa	ρ , g/m ³	μ , Pa*s	ν , m ² /s	1/ ν
7.6250	213	337.3	8.266	1.08E-05	0.00131	764
7.3750	214	345.0	8.416	1.09E-05	0.00129	774
7.1250	215	352.9	8.569	1.09E-05	0.00127	785
6.8750	216	361.0	8.724	1.10E-05	0.00126	795
6.6250	217	369.2	8.880	1.10E-05	0.00124	806
6.3750	218	377.5	9.039	1.11E-05	0.00122	817
6.1250	218	386.0	9.243	1.11E-05	0.00120	835
5.8750	219	394.7	9.407	1.11E-05	0.00118	847
5.6250	220	403.5	9.574	1.12E-05	0.00117	858
5.3750	221	412.5	9.743	1.12E-05	0.00115	869
5.1250	222	421.6	9.914	1.13E-05	0.00114	881
4.8750	223	430.9	10.087	1.13E-05	0.00112	892
4.6250	224	440.4	10.262	1.14E-05	0.00111	904
4.3750	224	450.0	10.487	1.14E-05	0.00108	924
4.1250	225	459.9	10.669	1.14E-05	0.00107	936
3.8750	226	469.9	10.853	1.14E-05	0.00105	948
3.6250	227	480.0	11.039	1.15E-05	0.00104	960
3.3750	227	490.4	11.278	1.15E-05	0.00102	981
3.1250	228	501.0	11.470	1.15E-05	0.00101	994
2.8750	228	511.8	11.717	1.15E-05	0.00099	1015
2.6250	229	522.8	11.917	1.16E-05	0.00097	1028
2.3750	229	534.0	12.172	1.16E-05	0.00095	1050
2.1250	229	545.4	12.433	1.16E-05	0.00093	1073
1.8750	229	557.1	12.699	1.16E-05	0.00091	1095
1.6250	229	569.0	12.971	1.16E-05	0.00089	1119
1.3750	228	581.2	13.308	1.15E-05	0.00087	1153
1.1250	227	593.8	13.655	1.15E-05	0.00084	1188

Table 4-9: JPL reference Mars atmosphere for -20° latitude (Continued)

Mars Atmosphere Model

Lat = -20 coxZ 0.7
 Z,deg 41.9298101

H, km	T, K	P, Pa	p, g/m ³	μ, Pa*s	v, m ² /s	1/v
0.8750	226	606.6	14.012	1.14E-05	0.00082	1224
0.6375	228	619.1	14.174	1.15E-05	0.00081	1228
0.4500	230	629.0	14.276	1.16E-05	0.00082	1226
0.3250	231	635.7	14.365	1.17E-05	0.00081	1229
0.2375	232	640.4	14.408	1.17E-05	0.00081	1228
0.1750	233	643.7	14.422	1.18E-05	0.00082	1224
0.1300	234	646.1	14.414	1.18E-05	0.00082	1218
0.0950	234	648.0	14.456	1.18E-05	0.00082	1222
0.0675	235	649.5	14.427	1.19E-05	0.00082	1214
0.0450	236	650.7	14.393	1.19E-05	0.00083	1207
0.0275	237	651.6	14.353	1.20E-05	0.00083	1198
0.0150	238	652.3	14.307	1.20E-05	0.00084	1190
0.0066	239	652.7	14.257	1.21E-05	0.00085	1181
0.0016	244	653.0	13.970	1.23E-05	0.00088	1135

Table 4-10: General Mars atmosphere model (NASA Langley)

Altitude(ell), km	Altitude (surf), km	Density (kg/m ³)	Pressure (N/m ²)	Temperature (K°)	Speed of Sound (m/s)
0.00E+00	-5.50E+00	1.44E-02	7.91E+02	2.87E+02	2.68E+02
1.00E+00	-4.50E+00	1.38E-02	7.39E+02	2.81E+02	2.65E+02
2.00E+00	-3.50E+00	1.31E-02	6.88E+02	2.74E+02	2.62E+02
3.00E+00	-2.50E+00	1.25E-02	6.40E+02	2.68E+02	2.59E+02
4.00E+00	-1.50E+00	1.19E-02	5.95E+02	2.62E+02	2.56E+02
5.00E+00	-5.00E-01	1.13E-02	5.52E+02	2.56E+02	2.53E+02
6.00E+00	5.00E-01	1.07E-02	5.11E+02	2.49E+02	2.50E+02
7.00E+00	1.50E+00	1.01E-02	4.72E+02	2.43E+02	2.47E+02
8.00E+00	2.50E+00	9.60E-03	4.35E+02	2.37E+02	2.43E+02

Table 4-10: General Mars atmosphere model (NASA Langley) (Continued)

Altitude(ell), km	Altitude (surf), km	Density (kg/m ³)	Pressure (N/m ²)	Temperature (K°)	Speed of Sound (m/s)
9.00E+00	3.50E+00	9.07E-03	4.00E+02	2.31E+02	2.40E+02
1.00E+01	4.50E+00	8.56E-03	3.68E+02	2.25E+02	2.37E+02
1.10E+01	5.50E+00	7.98E-03	3.37E+02	2.21E+02	2.35E+02
1.20E+01	6.50E+00	7.37E-03	3.08E+02	2.19E+02	2.34E+02
1.30E+01	7.50E+00	6.80E-03	2.82E+02	2.17E+02	2.33E+02
1.40E+01	8.50E+00	6.27E-03	2.58E+02	2.15E+02	2.32E+02
1.50E+01	9.50E+00	5.78E-03	2.35E+02	2.13E+02	2.31E+02
1.60E+01	1.05E+01	5.32E-03	2.15E+02	2.11E+02	2.30E+02
1.70E+01	1.15E+01	4.90E-03	1.96E+02	2.09E+02	2.29E+02
1.80E+01	1.25E+01	4.50E-03	1.78E+02	2.07E+02	2.28E+02
1.90E+01	1.35E+01	4.14E-03	1.63E+02	2.05E+02	2.27E+02
2.00E+01	1.45E+01	3.80E-03	1.48E+02	2.04E+02	2.26E+02
2.10E+01	1.55E+01	3.48E-03	1.34E+02	2.02E+02	2.25E+02
2.20E+01	1.65E+01	3.18E-03	1.22E+02	2.01E+02	2.24E+02
2.30E+01	1.75E+01	2.91E-03	1.11E+02	1.99E+02	2.23E+02
2.40E+01	1.85E+01	2.66E-03	1.01E+02	1.98E+02	2.22E+02
2.50E+01	1.95E+01	2.43E-03	9.12E+01	1.96E+02	2.22E+02
2.60E+01	2.05E+01	2.22E-03	8.26E+01	1.95E+02	2.21E+02
2.70E+01	2.15E+01	2.02E-03	7.48E+01	1.94E+02	2.20E+02
2.80E+01	2.25E+01	1.84E-03	6.77E+01	1.92E+02	2.19E+02
2.90E+01	2.35E+01	1.68E-03	6.13E+01	1.91E+02	2.18E+02
3.00E+01	2.45E+01	1.53E-03	5.54E+01	1.90E+02	2.18E+02
3.10E+01	2.55E+01	1.39E-03	5.00E+01	1.88E+02	2.17E+02
3.20E+01	2.65E+01	1.26E-03	4.51E+01	1.87E+02	2.16E+02
3.30E+01	2.75E+01	1.15E-03	4.07E+01	1.86E+02	2.15E+02
3.40E+01	2.85E+01	1.04E-03	3.67E+01	1.84E+02	2.15E+02
3.50E+01	2.95E+01	9.46E-04	3.31E+01	1.83E+02	2.14E+02
3.60E+01	3.05E+01	8.58E-04	2.98E+01	1.81E+02	2.13E+02
3.70E+01	3.15E+01	7.77E-04	2.68E+01	1.80E+02	2.12E+02

Table 4-10: General Mars atmosphere model (NASA Langley) (Continued)

Altitude(ell), km	Altitude (surf), km	Density (kg/m ³)	Pressure (N/m ²)	Temperature (K°)	Speed of Sound (m/s)
3.80E+01	3.25E+01	7.03E-04	2.41E+01	1.79E+02	2.12E+02
3.90E+01	3.35E+01	6.36E-04	2.16E+01	1.78E+02	2.11E+02
4.00E+01	3.45E+01	5.75E-04	1.94E+01	1.77E+02	2.10E+02
4.10E+01	3.55E+01	5.19E-04	1.74E+01	1.75E+02	2.09E+02
4.20E+01	3.65E+01	4.69E-04	1.56E+01	1.74E+02	2.09E+02
4.30E+01	3.75E+01	4.23E-04	1.40E+01	1.73E+02	2.08E+02
4.40E+01	3.85E+01	3.81E-04	1.25E+01	1.72E+02	2.07E+02
4.50E+01	3.95E+01	3.43E-04	1.12E+01	1.71E+02	2.06E+02
4.60E+01	4.05E+01	3.09E-04	1.00E+01	1.69E+02	2.06E+02
4.70E+01	4.15E+01	2.78E-04	8.95E+00	1.68E+02	2.05E+02
4.80E+01	4.25E+01	2.50E-04	7.99E+00	1.67E+02	2.04E+02
4.90E+01	4.35E+01	2.25E-04	7.12E+00	1.66E+02	2.04E+02
5.00E+01	4.45E+01	2.02E-04	6.35E+00	1.65E+02	2.03E+02
5.10E+01	4.55E+01	1.81E-04	5.65E+00	1.63E+02	2.02E+02
5.20E+01	4.65E+01	1.62E-04	5.03E+00	1.62E+02	2.01E+02
5.30E+01	4.75E+01	1.45E-04	4.47E+00	1.61E+02	2.01E+02
5.40E+01	4.85E+01	1.30E-04	3.98E+00	1.60E+02	2.00E+02
5.50E+01	4.95E+01	1.16E-04	3.53E+00	1.59E+02	1.99E+02
5.60E+01	5.05E+01	1.04E-04	3.13E+00	1.57E+02	1.98E+02
5.70E+01	5.15E+01	9.26E-05	2.77E+00	1.57E+02	1.98E+02
5.80E+01	5.25E+01	8.24E-05	2.46E+00	1.56E+02	1.97E+02
5.90E+01	5.35E+01	7.32E-05	2.18E+00	1.56E+02	1.97E+02
6.00E+01	5.45E+01	6.51E-05	1.93E+00	1.55E+02	1.97E+02
6.10E+01	5.55E+01	5.78E-05	1.71E+00	1.54E+02	1.96E+02
6.20E+01	5.65E+01	5.13E-05	1.51E+00	1.54E+02	1.96E+02
6.30E+01	5.75E+01	4.56E-05	1.34E+00	1.53E+02	1.96E+02
6.40E+01	5.85E+01	4.04E-05	1.18E+00	1.53E+02	1.95E+02
6.50E+01	5.95E+01	3.59E-05	1.04E+00	1.52E+02	1.95E+02
6.60E+01	6.05E+01	3.18E-05	9.21E-01	1.52E+02	1.95E+02

Table 4-10: General Mars atmosphere model (NASA Langley) (Continued)

Altitude(ell), km	Altitude (surf), km	Density (kg/m³)	Pressure (N/m²)	Temperature (K°)	Speed of Sound (m/s)
6.70E+01	6.15E+01	2.82E-05	8.14E-01	1.51E+02	1.94E+02
6.80E+01	6.25E+01	2.50E-05	7.18E-01	1.50E+02	1.94E+02
6.90E+01	6.35E+01	2.21E-05	6.34E-01	1.50E+02	1.94E+02
7.00E+01	6.45E+01	1.96E-05	5.59E-01	1.49E+02	1.93E+02
7.10E+01	6.55E+01	1.73E-05	4.93E-01	1.49E+02	1.93E+02
7.20E+01	6.65E+01	1.53E-05	4.34E-01	1.48E+02	1.92E+02
7.30E+01	6.75E+01	1.36E-05	3.82E-01	1.48E+02	1.92E+02
7.40E+01	6.85E+01	1.20E-05	3.37E-01	1.47E+02	1.92E+02
7.50E+01	6.95E+01	1.06E-05	2.96E-01	1.46E+02	1.91E+02
7.60E+01	7.05E+01	9.35E-06	2.61E-01	1.46E+02	1.91E+02
7.70E+01	7.15E+01	8.25E-06	2.29E-01	1.45E+02	1.91E+02
7.80E+01	7.25E+01	7.28E-06	2.02E-01	1.45E+02	1.90E+02
7.90E+01	7.35E+01	6.42E-06	1.77E-01	1.44E+02	1.90E+02
8.00E+01	7.45E+01	5.66E-06	1.56E-01	1.44E+02	1.89E+02
8.10E+01	7.55E+01	4.99E-06	1.37E-01	1.43E+02	1.89E+02
8.20E+01	7.65E+01	4.40E-06	1.20E-01	1.43E+02	1.89E+02
8.30E+01	7.75E+01	4.00E-06	1.09E-01	1.42E+02	1.89E+02
8.40E+01	7.85E+01	3.51E-06	9.55E-02	1.43E+02	1.89E+02
8.50E+01	7.95E+01	3.08E-06	8.39E-02	1.43E+02	1.89E+02
8.60E+01	8.05E+01	2.70E-06	7.36E-02	1.43E+02	1.89E+02
8.70E+01	8.15E+01	2.37E-06	6.47E-02	1.43E+02	1.89E+02
8.80E+01	8.25E+01	2.08E-06	5.68E-02	1.43E+02	1.89E+02
8.90E+01	8.35E+01	1.83E-06	4.99E-02	1.43E+02	1.89E+02
9.00E+01	8.45E+01	1.60E-06	4.38E-02	1.43E+02	1.89E+02
9.10E+01	8.55E+01	1.41E-06	3.85E-02	1.43E+02	1.89E+02
9.20E+01	8.65E+01	1.24E-06	3.38E-02	1.43E+02	1.89E+02
9.30E+01	8.75E+01	1.09E-06	2.97E-02	1.43E+02	1.89E+02
9.40E+01	8.85E+01	9.55E-07	2.61E-02	1.43E+02	1.89E+02
9.50E+01	8.95E+01	8.39E-07	2.30E-02	1.43E+02	1.89E+02

Table 4-10: General Mars atmosphere model (NASA Langley) (Continued)

Altitude(ell), km	Altitude (surf), km	Density (kg/m ³)	Pressure (N/m ²)	Temperature (K°)	Speed of Sound (m/s)
9.60E+01	9.05E+01	7.37E-07	2.02E-02	1.43E+02	1.89E+02
9.70E+01	9.15E+01	6.48E-07	1.78E-02	1.43E+02	1.89E+02
9.80E+01	9.25E+01	5.69E-07	1.56E-02	1.43E+02	1.89E+02
9.90E+01	9.35E+01	5.01E-07	1.37E-02	1.43E+02	1.89E+02
1.00E+02	9.45E+01	4.40E-07	1.21E-02	1.44E+02	1.89E+02
1.01E+02	9.55E+01	3.87E-07	1.06E-02	1.44E+02	1.89E+02
1.02E+02	9.65E+01	3.40E-07	9.35E-03	1.44E+02	1.89E+02
1.03E+02	9.75E+01	2.99E-07	8.22E-03	1.44E+02	1.89E+02
1.04E+02	9.85E+01	2.63E-07	7.24E-03	1.44E+02	1.90E+02
1.05E+02	9.95E+01	2.32E-07	6.37E-03	1.44E+02	1.90E+02
1.06E+02	1.01E+02	2.04E-07	5.61E-03	1.44E+02	1.90E+02
1.07E+02	1.02E+02	1.79E-07	4.94E-03	1.44E+02	1.90E+02
1.08E+02	1.03E+02	1.58E-07	4.35E-03	1.44E+02	1.90E+02
1.09E+02	1.04E+02	1.39E-07	3.83E-03	1.44E+02	1.90E+02
1.10E+02	1.05E+02	1.22E-07	3.37E-03	1.44E+02	1.90E+02
1.11E+02	1.06E+02	1.07E-07	2.97E-03	1.45E+02	1.90E+02
1.12E+02	1.07E+02	9.42E-08	2.62E-03	1.45E+02	1.91E+02
1.13E+02	1.08E+02	8.27E-08	2.31E-03	1.46E+02	1.91E+02
1.14E+02	1.09E+02	7.27E-08	2.04E-03	1.47E+02	1.92E+02
1.15E+02	1.10E+02	6.39E-08	1.80E-03	1.47E+02	1.92E+02
1.16E+02	1.11E+02	5.62E-08	1.59E-03	1.48E+02	1.92E+02
1.17E+02	1.12E+02	4.95E-08	1.41E-03	1.49E+02	1.93E+02
1.18E+02	1.13E+02	4.36E-08	1.25E-03	1.50E+02	1.93E+02
1.19E+02	1.14E+02	3.84E-08	1.10E-03	1.50E+02	1.94E+02
1.20E+02	1.15E+02	3.39E-08	9.78E-04	1.51E+02	1.94E+02
1.21E+02	1.16E+02	2.99E-08	8.68E-04	1.52E+02	1.95E+02
1.22E+02	1.17E+02	2.64E-08	7.70E-04	1.52E+02	1.95E+02
1.23E+02	1.18E+02	2.34E-08	6.83E-04	1.53E+02	1.96E+02
1.24E+02	1.19E+02	2.07E-08	6.07E-04	1.54E+02	1.96E+02

Table 4-10: General Mars atmosphere model (NASA Langley) (Continued)

Altitude(ell), km	Altitude (surf), km	Density (kg/m ³)	Pressure (N/m ²)	Temperature (K ^o)	Speed of Sound (m/s)
1.25E+02	1.20E+02	1.83E-08	5.40E-04	1.54E+02	1.96E+02

Table 4-11: Mars-GRAM generated atmosphere profile for -25° latitude, 11° longitude

Height (km)	Density (kg/m ³)	Temperature (K)	Pressure (Pa)	Speed of Sound (m/s)	Viscosity (kg/m s)
2.38	1.25E-02	252.4	594.8	251.11	1.29E-05
2.5	1.24E-02	251.8	589.2	250.82	1.28E-05
2.75	1.22E-02	250.7	577.9	250.27	1.28E-05
3	1.20E-02	249.7	566.9	249.77	1.27E-05
3.25	1.18E-02	248.6	556	249.22	1.27E-05
3.5	1.17E-02	247.5	545.4	248.66	1.26E-05
3.75	1.15E-02	246.5	534.9	248.16	1.26E-05
4	1.13E-02	245.4	524.7	247.61	1.25E-05
4.25	1.12E-02	244.3	514.6	247.05	1.24E-05
4.5	1.10E-02	243.2	504.8	246.49	1.24E-05
4.75	1.08E-02	242.2	495.1	245.99	1.23E-05
5	1.07E-02	241.1	485.6	245.43	1.23E-05
5.25	1.05E-02	240.5	475.4	245.12	1.22E-05
5.5	1.03E-02	239.9	465.4	244.82	1.22E-05
5.75	1.01E-02	239.3	455.6	244.51	1.22E-05
6	9.90E-03	238.7	446	244.2	1.22E-05
6.25	9.71E-03	238.1	436.6	243.9	1.21E-05
6.5	9.53E-03	237.6	427.4	243.64	1.21E-05
6.75	9.35E-03	237	418.4	243.33	1.21E-05
7	9.18E-03	236.4	409.6	243.02	1.20E-05
7.25	9.01E-03	235.8	401	242.72	1.20E-05
7.5	8.84E-03	235.2	392.6	242.41	1.20E-05
7.75	8.68E-03	234.6	384.3	242.1	1.19E-05

Table 4-11: Mars-GRAM generated atmosphere profile for -25° latitude, 11° longitude (Continued)

Height (km)	Density (kg/m ³)	Temperature (K)	Pressure (Pa)	Speed of Sound (m/s)	Viscosity (kg/m s)
8	8.51E-03	234	376.2	241.79	1.19E-05
8.25	8.36E-03	233.4	368.3	241.48	1.19E-05
8.5	8.20E-03	232.8	360.5	241.17	1.19E-05
8.75	8.05E-03	232.2	353	240.86	1.18E-05
9	7.90E-03	231.6	345.5	240.54	1.18E-05
9.25	7.75E-03	231	338.3	240.23	1.18E-05
9.5	7.61E-03	230.4	331.1	239.92	1.17E-05
9.75	7.47E-03	229.9	324.2	239.66	1.17E-05
10	7.33E-03	229.3	317.3	239.35	1.17E-05
10.25	7.18E-03	228.8	310.5	239.09	1.16E-05
10.5	7.04E-03	228.4	303.7	238.88	1.16E-05
10.75	6.90E-03	228	297.1	238.67	1.16E-05
11	6.76E-03	227.6	290.7	238.46	1.16E-05
11.25	6.63E-03	227.1	284.4	238.2	1.16E-05
11.5	6.50E-03	226.7	278.2	237.99	1.15E-05
11.75	6.37E-03	226.3	272.2	237.78	1.15E-05
12	6.24E-03	225.9	266.3	237.57	1.15E-05
12.25	6.12E-03	225.4	260.5	237.3	1.15E-05
12.5	6.00E-03	225	254.9	237.09	1.15E-05
12.75	5.88E-03	224.6	249.3	236.88	1.14E-05
13	5.76E-03	224.2	243.9	236.67	1.14E-05
13.25	5.65E-03	223.8	238.6	236.46	1.14E-05
13.5	5.53E-03	223.3	233.5	236.19	1.14E-05
13.75	5.42E-03	222.9	228.4	235.98	1.13E-05
14	5.32E-03	222.5	223.5	235.77	1.13E-05
14.25	5.21E-03	222.1	218.6	235.56	1.13E-05
14.5	5.11E-03	221.6	213.9	235.29	1.13E-05
14.75	5.01E-03	221.2	209.2	235.08	1.13E-05

Table 4-11: Mars-GRAM generated atmosphere profile for -25° latitude, 11° longitude (Continued)

Height (km)	Density (kg/m ³)	Temperature (K)	Pressure (Pa)	Speed of Sound (m/s)	Viscosity (kg/m s)
15	4.91E-03	220.8	204.7	234.87	1.12E-05
15.25	4.80E-03	220.4	200.1	234.66	1.12E-05
15.5	4.70E-03	219.9	195.6	234.39	1.12E-05
15.75	4.61E-03	219.5	191.1	234.18	1.12E-05
16	4.51E-03	219.1	186.8	233.96	1.11E-05
16.25	4.42E-03	218.7	182.6	233.75	1.11E-05
16.5	4.33E-03	218.3	178.5	233.54	1.11E-05
16.75	4.24E-03	217.8	174.5	233.27	1.11E-05
17	4.15E-03	217.4	170.5	233.05	1.11E-05
17.25	4.06E-03	217	166.7	232.84	1.10E-05
17.5	3.98E-03	216.6	162.9	232.62	1.10E-05
17.75	3.90E-03	216.1	159.2	232.36	1.10E-05
18	3.82E-03	215.7	155.6	232.14	1.10E-05
18.25	3.74E-03	215.3	152.1	231.93	1.09E-05
18.5	3.66E-03	214.9	148.7	231.71	1.09E-05
18.75	3.59E-03	214.5	145.3	231.49	1.09E-05
19	3.51E-03	214	142.1	231.22	1.09E-05
19.25	3.44E-03	213.6	138.8	231.01	1.09E-05
19.5	3.37E-03	213.2	135.7	230.79	1.08E-05
19.75	3.30E-03	212.8	132.6	230.57	1.08E-05
20	3.23E-03	212.4	129.7	230.36	1.08E-05

Table 4-12: Mars-GRAM generated atmosphere profile for 57° latitude, 2.35° longitude

Height (km)	Density (kg/m ³)	Temperature (K)	Pressure (Pa)	Speed of Sound (m/s)	Viscosity (kg/m s)
-1.74	2.82E-02	168.3	896.7	205.05	8.44E-06
-1.5	2.72E-02	168.8	865.8	205.36	8.47E-06

Table 4-12: Mars-GRAM generated atmosphere profile for 57° latitude, 2.35° longitude (Continued)

Height (km)	Density (kg/m ³)	Temperature (K)	Pressure (Pa)	Speed of Sound (m/s)	Viscosity (kg/m s)
-1.25	2.63E-02	169.3	842.1	205.66	8.49E-06
-1	2.55E-02	169.8	819	205.97	8.52E-06
-0.75	2.48E-02	170.3	796.5	206.27	8.55E-06
-0.5	2.40E-02	170.8	774.7	206.57	8.57E-06
-0.25	2.33E-02	171.3	753.4	206.87	8.60E-06
0	2.26E-02	171.7	732.8	207.11	8.62E-06
0.25	2.19E-02	172.2	712.7	207.42	8.65E-06
0.5	2.12E-02	172.7	693.1	207.72	8.68E-06
0.75	2.06E-02	173.2	674.1	208.02	8.71E-06
1	2.00E-02	173.7	655.6	208.32	8.73E-06
1.25	1.94E-02	174.2	637.6	208.62	8.76E-06
1.5	1.88E-02	174.7	620.1	208.92	8.79E-06
1.75	1.82E-02	175.2	603.1	209.21	8.81E-06
2	1.77E-02	175.7	586.6	209.51	8.84E-06
2.25	1.71E-02	176.1	570.5	209.75	8.86E-06
2.5	1.66E-02	176.6	554.8	210.05	8.89E-06
2.75	1.61E-02	177.1	539.6	210.35	8.92E-06
3	1.56E-02	177.6	524.8	210.64	8.94E-06
3.25	1.52E-02	178.1	510.4	210.94	8.97E-06
3.5	1.47E-02	178.6	496.4	211.24	9.00E-06
3.75	1.43E-02	179.1	482.8	211.53	9.02E-06
4	1.38E-02	179.6	469.5	211.83	9.05E-06
4.25	1.34E-02	180.1	456.7	212.12	9.08E-06
4.5	1.30E-02	180.6	444.1	212.41	9.11E-06
4.75	1.26E-02	181	431.9	212.65	9.13E-06
5	1.22E-02	181.5	420.1	212.94	9.15E-06
5.25	1.19E-02	181.8	409	213.12	9.17E-06
5.5	1.16E-02	182.1	398.2	213.3	9.19E-06

Table 4-12: Mars-GRAM generated atmosphere profile for 57° latitude, 2.35° longitude (Continued)

Height (km)	Density (kg/m³)	Temperature (K)	Pressure (Pa)	Speed of Sound (m/s)	Viscosity (kg/m s)
5.75	1.12E-02	182.4	387.8	213.47	9.20E-06
6	1.09E-02	182.7	377.5	213.65	9.22E-06
6.25	1.06E-02	183	367.6	213.82	9.24E-06
6.5	1.03E-02	183.3	357.9	214	9.25E-06
6.75	1.00E-02	183.5	348.5	214.11	9.26E-06
7	9.77E-03	183.8	339.3	214.29	9.28E-06
7.25	9.49E-03	184.1	330.3	214.46	9.29E-06
7.5	9.23E-03	184.4	321.6	214.64	9.31E-06
7.75	8.97E-03	184.7	313.2	214.81	9.33E-06
8	8.72E-03	185	304.9	214.99	9.34E-06
8.25	8.48E-03	185.3	296.9	215.16	9.36E-06
8.5	8.24E-03	185.6	289.1	215.34	9.38E-06
8.75	8.01E-03	185.8	281.4	215.45	9.39E-06
9	7.79E-03	186.1	274	215.62	9.40E-06
9.25	7.57E-03	186.4	266.8	215.8	9.42E-06
9.5	7.36E-03	186.7	259.8	215.97	9.43E-06
9.75	7.16E-03	187	252.9	216.15	9.45E-06
10	6.96E-03	187.3	246.3	216.32	9.47E-06
10.25	6.77E-03	187.5	239.9	216.43	9.48E-06
10.5	6.59E-03	187.6	233.8	216.49	9.48E-06
10.75	6.41E-03	187.8	227.8	216.61	9.49E-06
11	6.24E-03	188	221.9	216.72	9.50E-06
11.25	6.08E-03	188.2	216.2	216.84	9.51E-06
11.5	5.92E-03	188.4	210.7	216.95	9.53E-06
11.75	5.76E-03	188.5	205.3	217.01	9.53E-06
12	5.60E-03	188.7	200	217.13	9.54E-06
12.25	5.46E-03	188.9	194.9	217.24	9.55E-06
12.5	5.31E-03	189.1	189.9	217.36	9.56E-06

Table 4-12: Mars-GRAM generated atmosphere profile for 57° latitude, 2.35° longitude (Continued)

Height (km)	Density (kg/m ³)	Temperature (K)	Pressure (Pa)	Speed of Sound (m/s)	Viscosity (kg/m s)
12.75	5.17E-03	189.3	185	217.47	9.57E-06
13	5.03E-03	189.4	180.2	217.53	9.58E-06
13.25	4.90E-03	189.6	175.6	217.64	9.59E-06
13.5	4.77E-03	189.8	171.1	217.76	9.60E-06
13.75	4.64E-03	190	166.7	217.87	9.61E-06
14	4.52E-03	190.2	162.4	217.99	9.62E-06
14.25	4.40E-03	190.3	158.2	218.04	9.63E-06
14.5	4.28E-03	190.5	154.2	218.16	9.64E-06
14.75	4.16E-03	190.7	150.2	218.27	9.65E-06
15	4.05E-03	190.9	146.4	218.39	9.66E-06
15.25	3.95E-03	190.9	142.7	218.39	9.66E-06
15.5	3.85E-03	191	139	218.45	9.66E-06
15.75	3.75E-03	191	135.5	218.45	9.66E-06
16	3.66E-03	191	132.1	218.45	9.66E-06
16.25	3.56E-03	191.1	128.7	218.5	9.67E-06
16.5	3.47E-03	191.1	125.4	218.5	9.67E-06
16.75	3.38E-03	191.1	122.3	218.5	9.67E-06
17	3.30E-03	191.2	119.2	218.56	9.68E-06
17.25	3.21E-03	191.2	116.1	218.56	9.68E-06
17.5	3.13E-03	191.2	113.2	218.56	9.68E-06
17.75	3.05E-03	191.2	110.3	218.56	9.68E-06
18	2.97E-03	191.3	107.5	218.62	9.68E-06
18.25	2.90E-03	191.3	104.8	218.62	9.68E-06
18.5	2.82E-03	191.3	102.1	218.62	9.68E-06
18.75	2.75E-03	191.4	99.5	218.67	9.69E-06
19	2.68E-03	191.4	97	218.67	9.69E-06
19.25	2.61E-03	191.4	94.5	218.67	9.69E-06
19.5	2.54E-03	191.5	92.1	218.73	9.69E-06

**Table 4-12: Mars-GRAM generated atmosphere profile for 57° latitude,
2.35° longitude (Continued)**

Height (km)	Density (kg/ m³)	Temperature (K)	Pressure (Pa)	Speed of Sound (m/s)	Viscosity (kg/m s)
19.75	2.48E-03	191.5	89.8	218.73	9.69E-06
20	2.42E-03	191.5	87.5	218.73	9.69E-06

Chapter 5.0 Feasibility Analysis

5.1 Solar Array Power Production

One of the main operational constraints on the SSA is the amount of power available for flight. The main power source for the SSA is the sun. PV arrays convert sunlight into electricity, which is either stored in the lithium-ion battery or used directly for aircraft operation. The amount of solar energy available is dependent on the location (or latitude) of the aircraft, the time of year, and any atmospheric attenuation due to clouds, haze, or dust. For the aircraft to operate, the power requirements will need to be less than what is available from the solar arrays.

To determine the available power at the various proposed operational locations (Venus, Earth, and Mars), some assumptions must be made about the capabilities and geometry of the solar array and its power-control system. These assumptions are as follows:

- Solar cell efficiency (η_{sc}) 10%
- Solar cell fill factor (Sff) 80%
- Power conditioning efficiency (η_{pcon}) 95%
- Horizontal solar array

Also important in determining the total available power are the orbital and environmental characteristics of the planets where the SSA might operate. From the environmental section, the data that is important in determining the output of the solar array is given in Table 5-1.

Table 5-1: Solar array output parameters

Parameter	Venus	Earth	Mars
Orbital eccentricity (e)	0.0068	0.0167	0.0934
Maximum eeclination angle (δ_{max})	3°	23.5°	24°
Mean orbital radius (km) (r_m)	108×10^6	150×10^6	228×10^6
Total days in a year (d_p)	0.92	365	666
Day length (hours) (h_p)	5,816	23.935	24.65
Mean solar intensity at planetary orbit (W/m^2) (SI_{om})	2,620	1,352.8	590
Atmospheric attenuation (τ)	0.75	0.85	0.85

The power available (P) per square meter of area is calculated as follows:

$$P = SI_o \tau \eta_{sc} S_{ff} (S - C \cos(-a)) \quad \text{Equation 5-1}$$

where

$$S = \sin(\phi) \sin(\delta) \quad \text{Equation 5-2}$$

$$C = \cos(\phi) \cos(\delta) \quad \text{Equation 5-3}$$

The latitude (ϕ) and Earth's declination angle (δ) vary with the day of the year (d). This day number (d) is based on the vernal equinox, so d = 1 is March 21 for Earth.

$$\delta = \delta_{max} \sin(2 \pi d / d_t) \quad \text{Equation 5-4}$$

The hour angle (a) is given by the following expression, where i is the instantaneous time of day in hours:

$$a = 2 \pi i / h_1 \quad \text{Equation 5-5}$$

$$SI_o = SI_{om} (r_m^2 / r^2) \quad \text{Equation 5-6}$$

The distance from the flight planet to the sun (r) varies throughout the year. The planet's orbital radius is based on the mean radius (r_m) and is represented by Equations 5-7 and 5-8. The day number (d_p) is based on the date of perihelion. So, for Earth, $d_p = 1$ is January 4th:

$$r = r_m (1 - e^2) / (1 + e \cos(\theta)) \quad \text{Equation 5-7}$$

$$\theta = 2 \pi d_p / d_t \quad \text{Equation 5-8}$$

Based on the equations given above, power-available curves were generated for Venus, Earth, and Mars. These curves will be used to determine the flight envelope for the SSA. The curves represent the available power at different latitudes and times of the year. Four times of the year were plotted: vernal equinox, summer solstice, autumnal equinox, and winter solstice. These dates represent the maximum and minimum points for the year as well as the times of equal day-night cycle lengths. Figure 5-1 shows the power available on Venus at different latitudes. Because the day length is longer than one year on Venus, there are no plots showing its available power as a function of time of year. A single day length covers the entire year. Therefore, the yearly change in output power is the same as the change throughout a day period. Figures 5-2 through 5-6 show the power available on Earth, and Figures 5-7 through 5-11 show the power available on Venus.

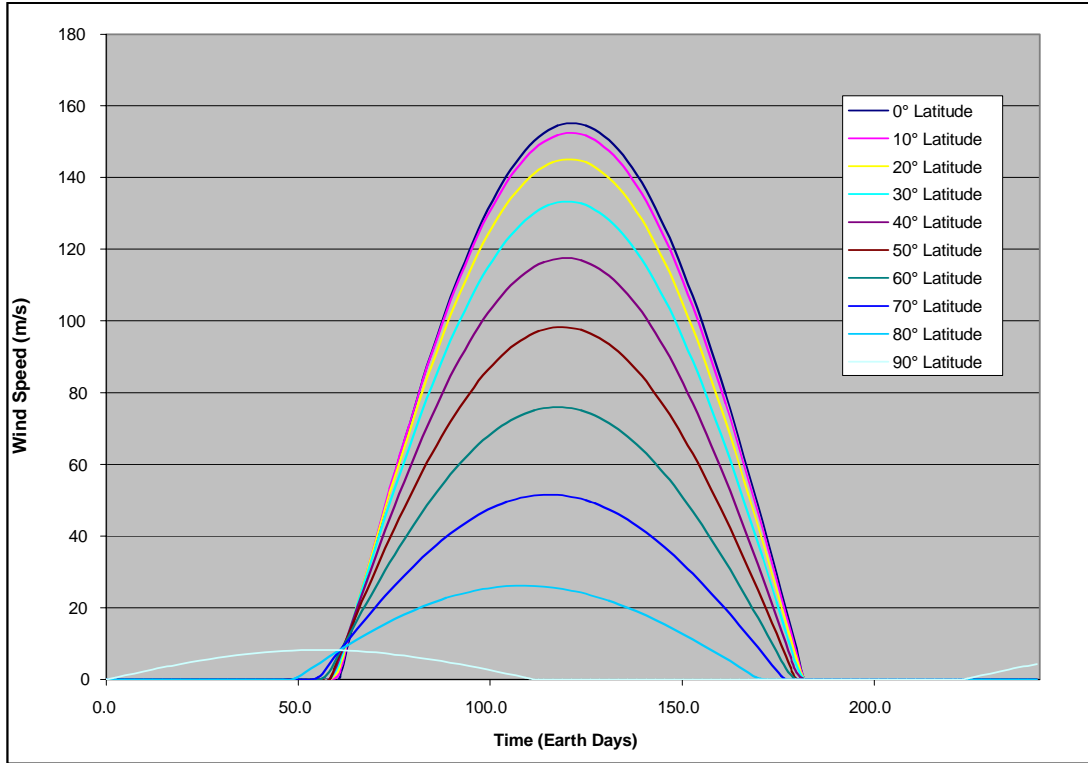


Figure 5-1: Venus: Available power throughout a day at various latitudes

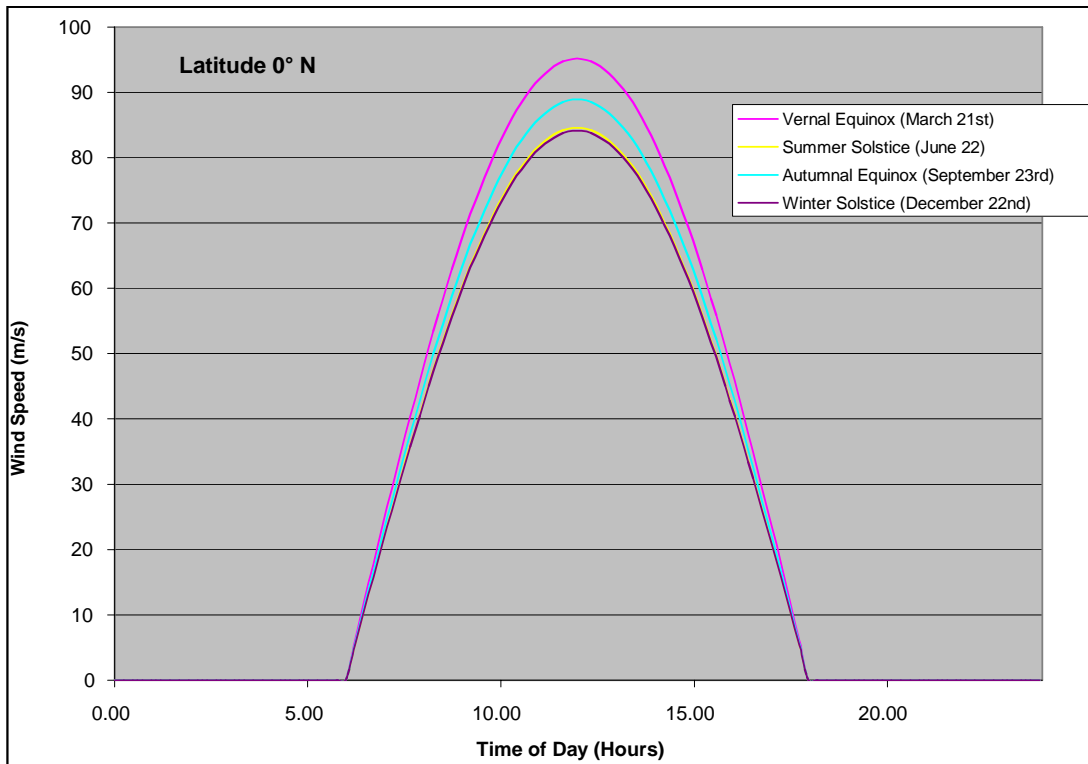


Figure 5-2: Earth: Available power throughout the day at 0° latitude

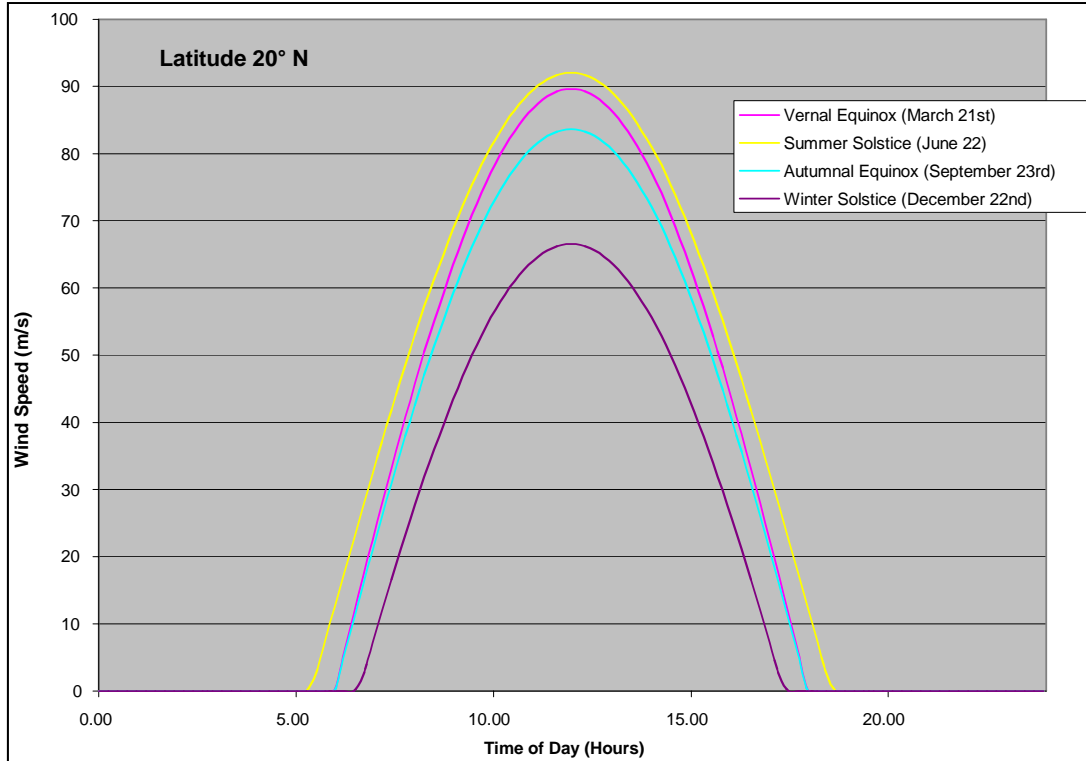


Figure 5-3: Earth: Available power throughout the day at 20° latitude

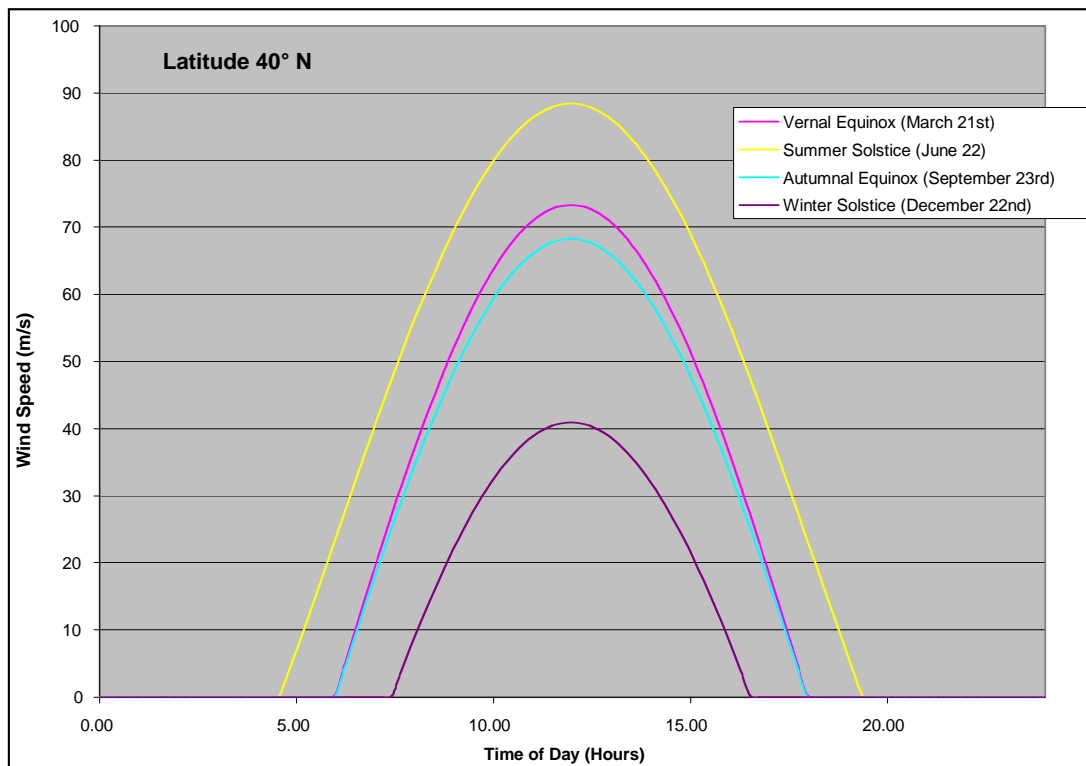


Figure 5-4: Earth: Available power throughout the day at 40° latitude

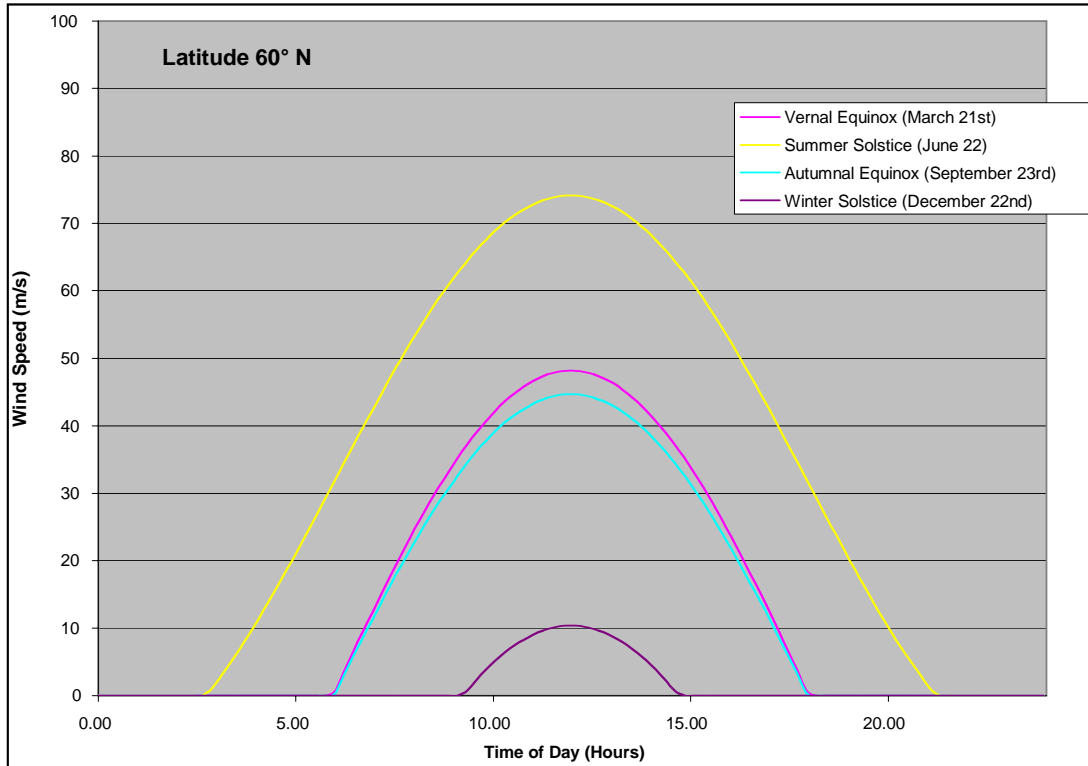


Figure 5-5: Earth: Available power throughout the day at 60° latitude

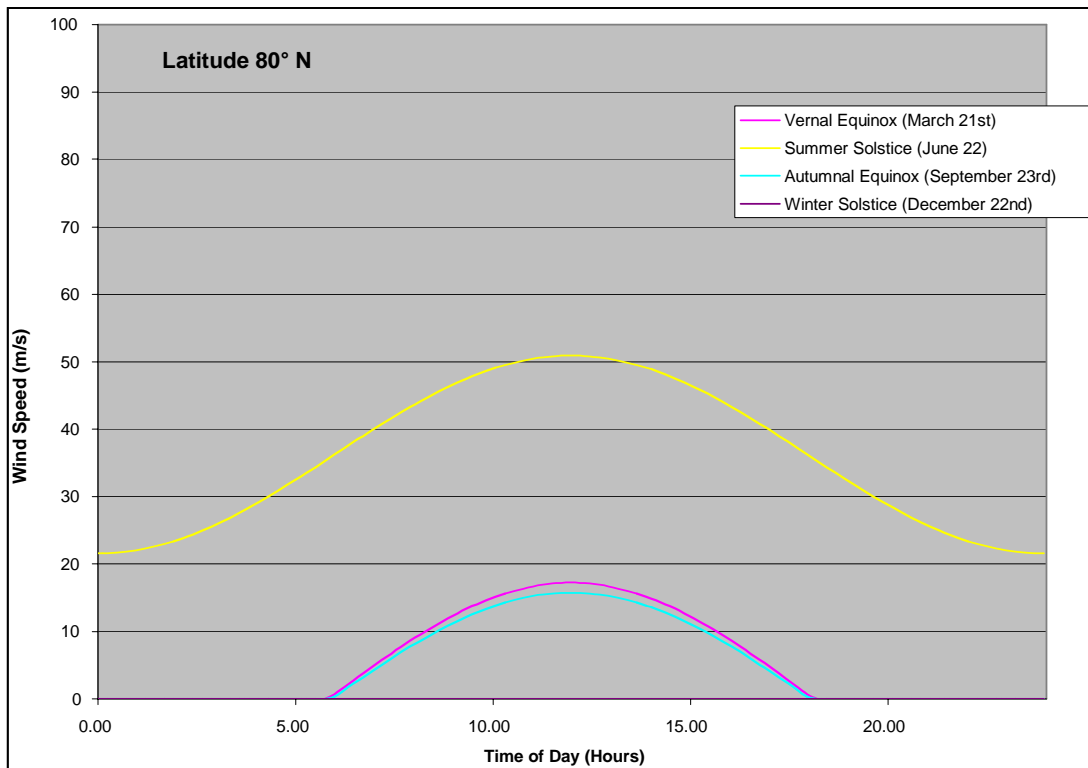


Figure 5-6: Earth: Available power throughout the day at 80° latitude

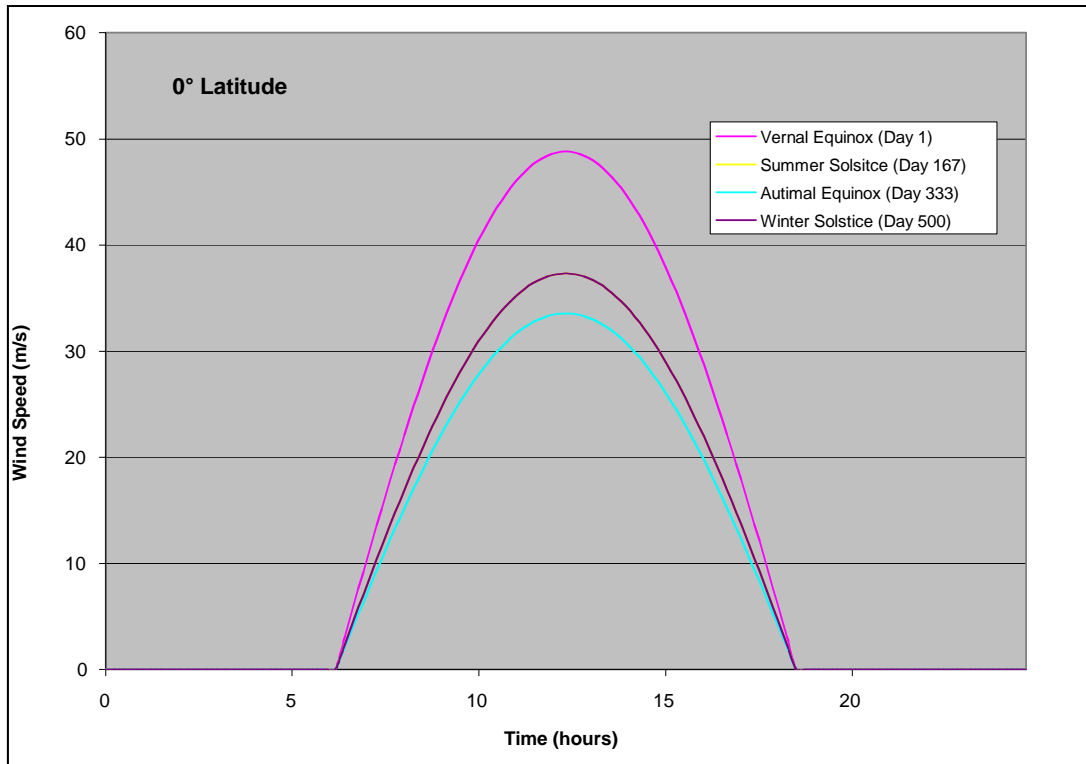


Figure 5-7: Mars: Available power throughout the day at 0° latitude

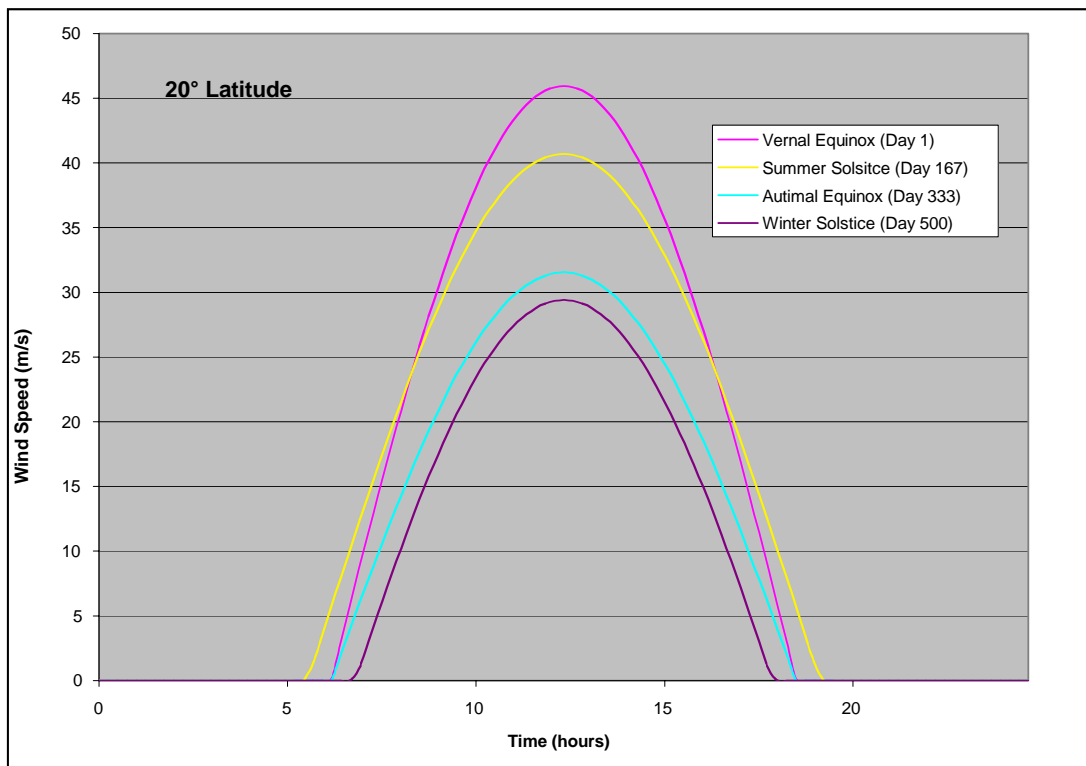


Figure 5-8: Mars: Available power throughout the day at 20° latitude

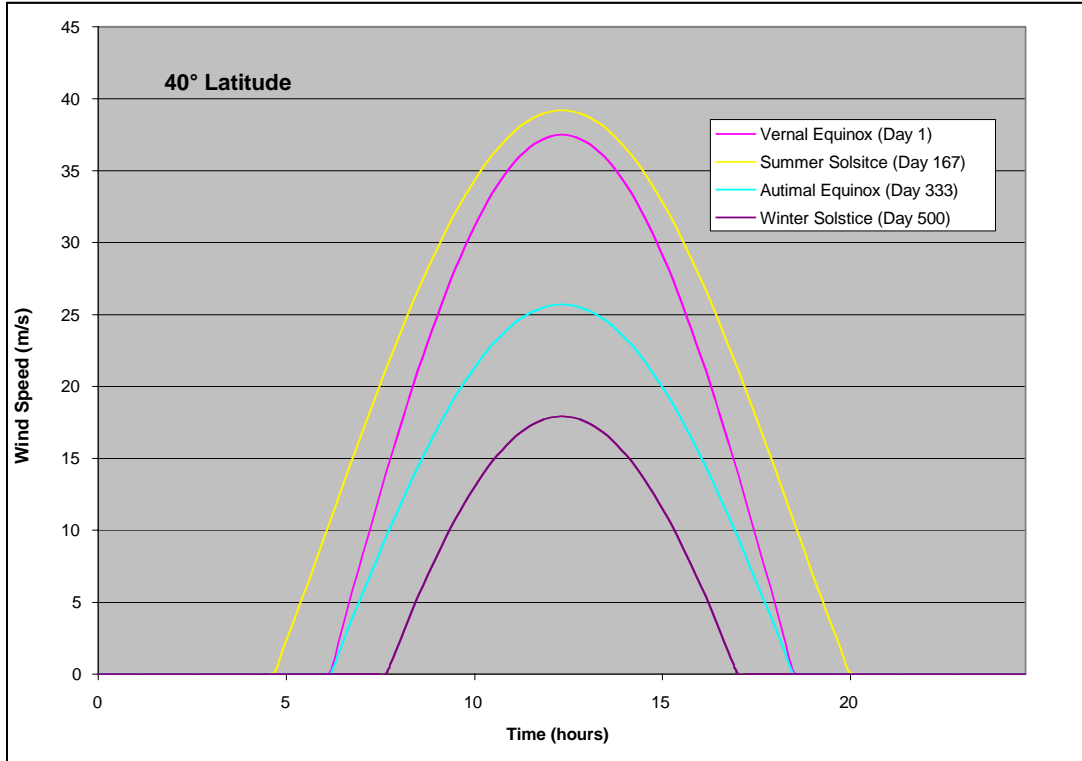


Figure 5-9: Mars: Available power throughout the day at 40° latitude

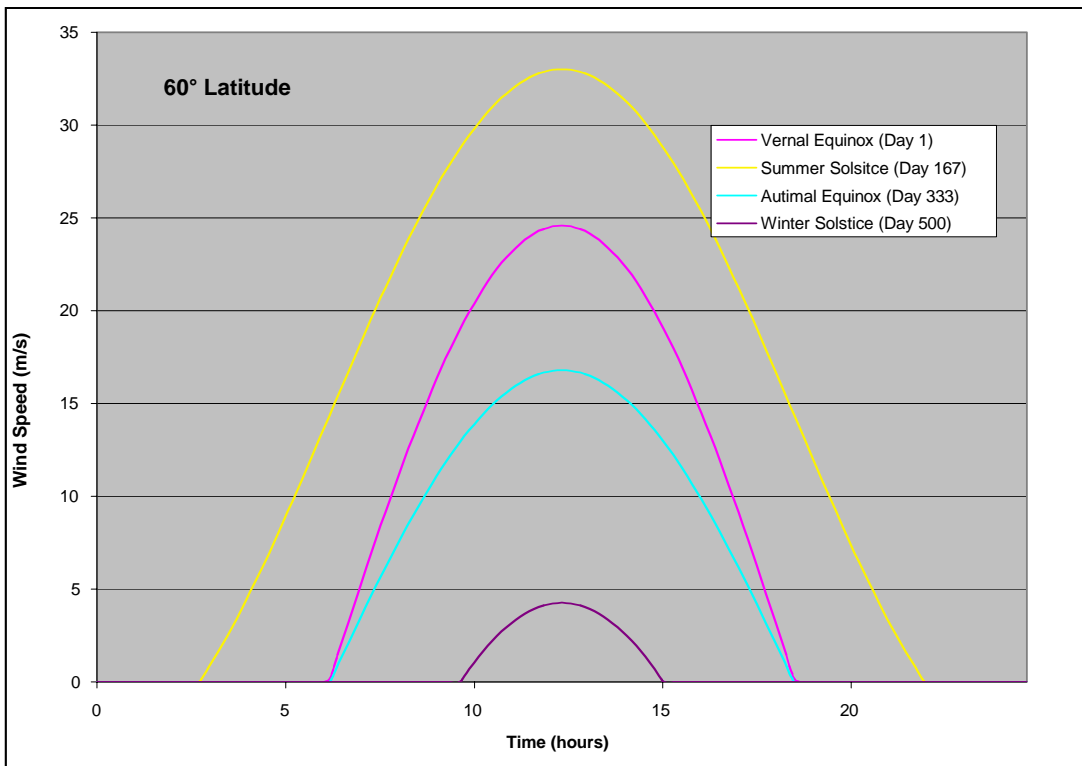


Figure 5-10: Mars: Available power throughout the day at 60° latitude

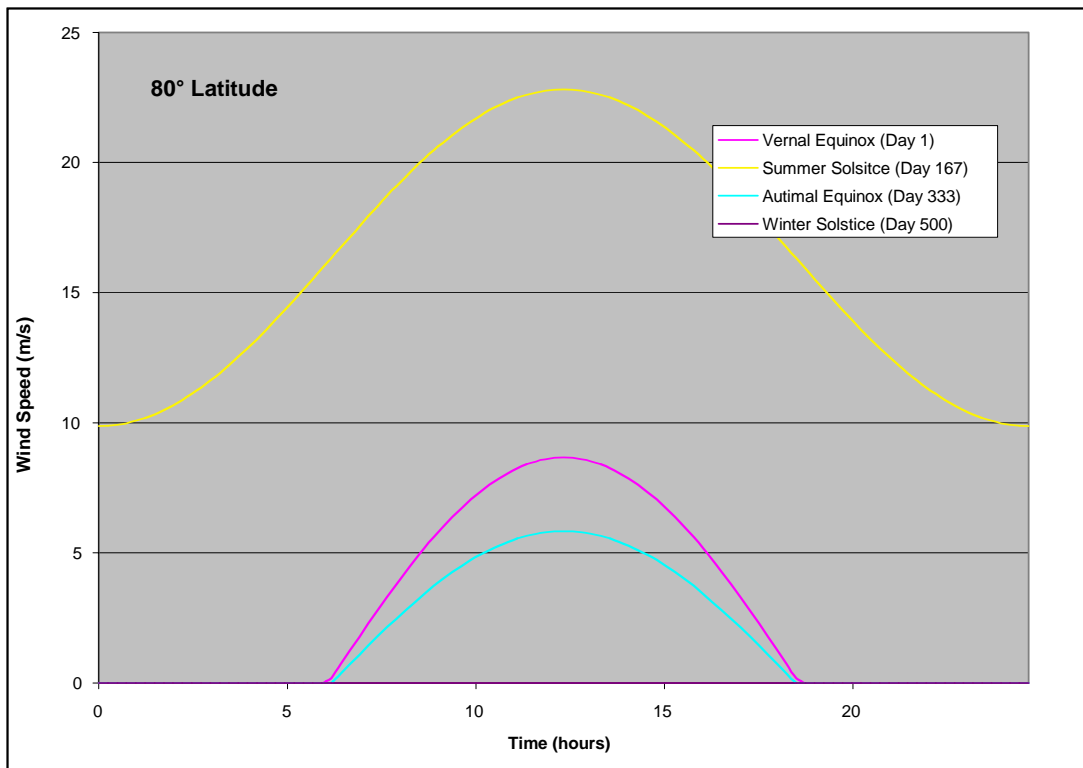


Figure 5-11: Mars: Available power throughout the day at 80° latitude

5.2 Vehicle-Sizing Analysis

5.2.1 Airfoil Properties

Like all flapping wing flyers in nature, the SSA will operate within a low Reynolds number flight regime. This is due mainly to its required low wing loading and the potential for high altitude operation, where the air density is low. The Reynolds number for the vehicle is based on the chord length (c), velocity of air over the wing (V), and air density and viscosity (ρ , μ). The Reynolds number (given in Equation 5-9) is a means of gauging the aerodynamic performance and capabilities of a vehicle. Vehicles or devices operating under the same Reynolds number operate similarly aerodynamically. The Reynolds number is a nondimensional number representing a ratio of the dynamic forces to viscous forces of the fluid flow over the given object.

$$R_e = \frac{\rho V c}{\mu} \quad \text{Equation 5-9}$$

The altitude at which the SSA flies will establish the density and viscosity as well as the flight speed. Because the aircraft's mass is assumed to be evenly distributed over its wing surface, wing loading is constant regardless of vehicle size. Changing the aircraft's size or wingspan, therefore, affects the chord length (for a given aspect ratio), but it does not affect cruise velocity. Cruise velocity is, however, affected by atmospheric conditions and therefore will vary with altitude. This can be seen in Figure 5-12 for various wing-loading values.

Based on the velocities shown in Figure 5-12, the cruise-flight Reynolds numbers for the aircraft are shown in Figure 5-13. This figure represents Reynolds number per wing-chord length. To get the actual flight Reynolds number, the values in the graph need to be multiplied by the chord length in meters. Reynolds numbers below approximately $2.00E5$ are considered to be low and produce low Reynolds number aerodynamic effects.

Airfoils within this low Reynolds number flight regime have characteristics that differ somewhat from those used in higher Reynolds number operation. The main issue, which at low Reynolds numbers is highly variable, is boundary-layer stability, which describes where the boundary layer separates from the surface or transitions to turbulent flow. These boundary-layer effects will in turn affect the wing's lift-generating capability and control.

A curved flat plate airfoil was used for the SSA analysis. Because of the desired low wing loading, airfoil thickness will be kept to a minimum. With a wing-chord length much larger than the wing thickness, the curved flat plate provides a good approximation of the lifting characteristics of the wing. Data on a curved flat plate are shown in Figures 5-14 and 5-15. As a more detailed design of the vehicle is achieved, the airfoil will be optimized for greater efficiency and lift. However, this optimization is beyond the scope of this Phase I project and will be addressed in more detail during Phase II.

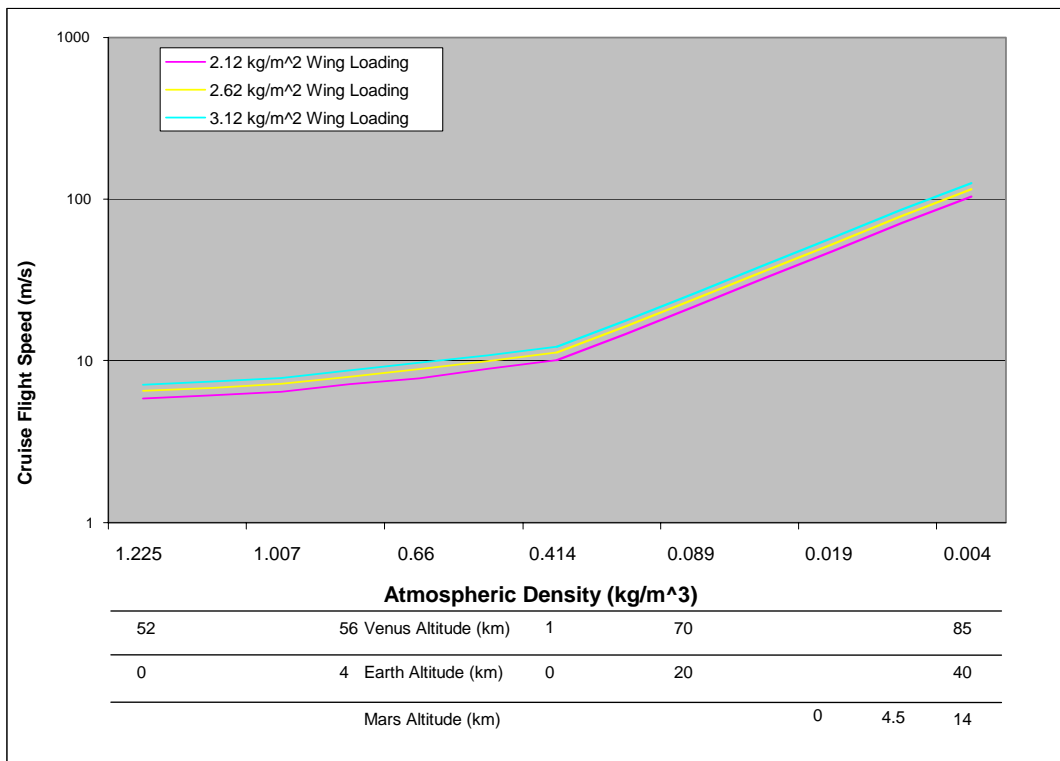


Figure 5-12: Cruise-flight speed as a function of atmospheric density

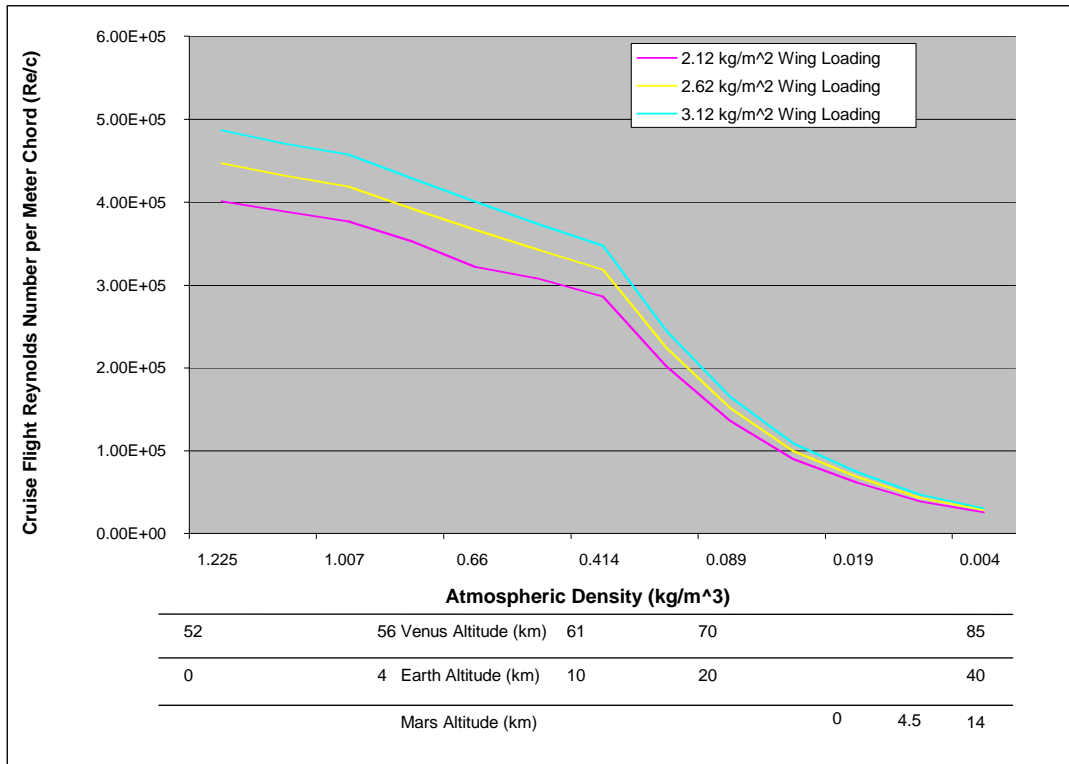


Figure 5-13: Cruise Reynolds number per chord length vs. atmospheric density

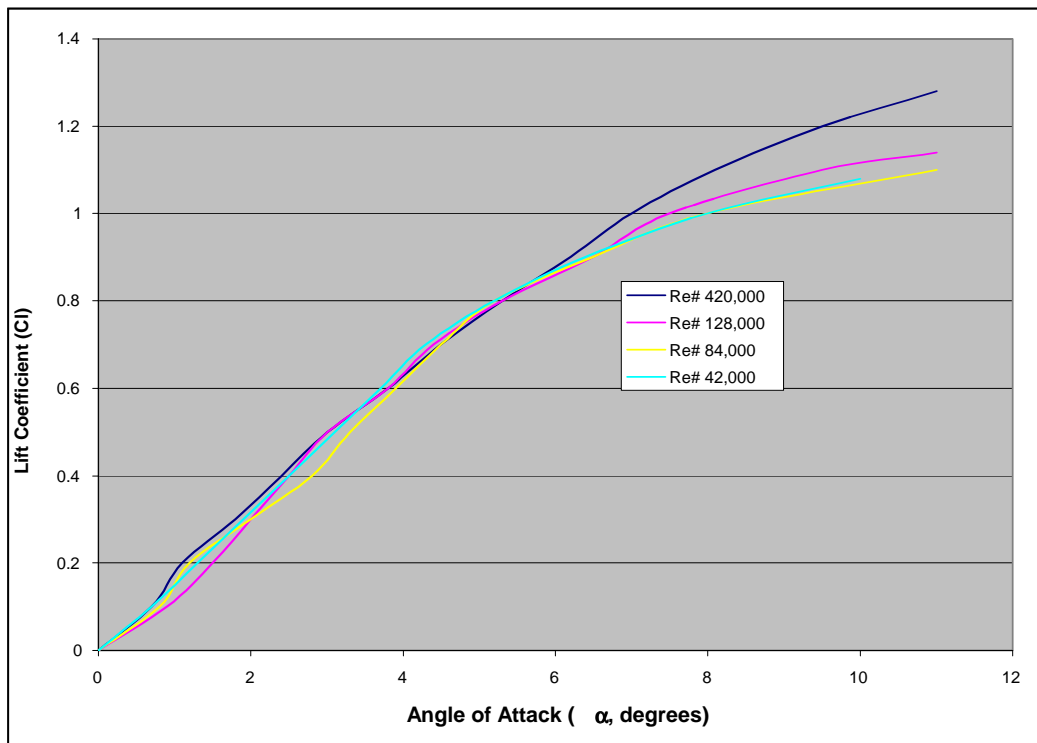


Figure 5-14: Lift coefficient vs. angle of attack for a curved flat plate at various low Reynolds numbers [9]

Regressions were performed on the lift coefficient (C_l) versus angle of attack data (α) plotted in Figure 5-14. The curve-fits generated by the regressions are given in Equations 5-10 through 5-13.

$$\text{Re\#} = 420,000 \quad C_l = -0.010263 + 0.18651\alpha - 0.0062394\alpha^2 \quad \text{Equation 5-10}$$

$$\text{Re\#} = 420,000 \quad C_l = -0.092355 + 0.22017\alpha - 0.0098994\alpha^2 \quad \text{Equation 5-11}$$

$$\text{Re\#} = 420,000 \quad C_l = -0.037329 + 0.19727\alpha - 0.008449\alpha^2 \quad \text{Equation 5-12}$$

$$\text{Re\#} = 420,000 \quad C_l = -0.029874 + 0.20066\alpha - 0.0086644\alpha^2 \quad \text{Equation 5-13}$$

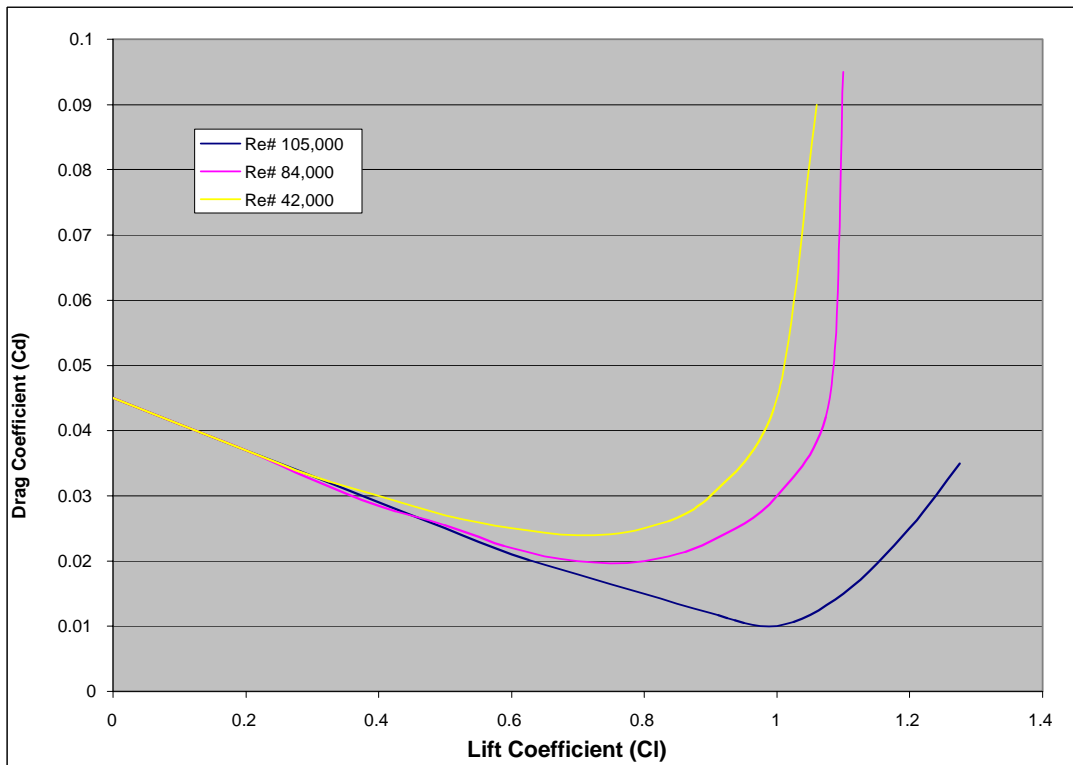


Figure 5-15: Lift coefficient vs. drag coefficient for a curved flat plate at various low Reynolds numbers

[9]

As with the data in Figure 5-14, a regression was performed for the data used to generate Figure 5-15. The resulting curve-fits of lift coefficient versus drag coefficient for various Reynolds numbers are given in Equations 5-14 through 5-16.

Re# = 105,000

$$C_d = 0.045079 - 0.041756C_l - 0.0027412C_l^2 + 0.049651C_l^3 - 0.10393C_l^4 + 0.065285C_l^5 \quad \text{Equation 5-14}$$

Re# = 84,000

$$C_d = 0.044899 - 0.02599C_l - 0.13674C_l^2 + 0.41452C_l^3 - 0.51246C_l^4 + 0.24663C_l^5 \quad \text{Equation 5-15}$$

Re# = 42,000

$$C_d = 0.044885 - 0.032763C_l - 0.058057C_l^2 + 0.23791C_l^3 - 0.3715C_l^4 + 0.22436C_l^5 \quad \text{Equation 5-16}$$

5.2.2 Power and Energy Required

The power required (P) by the SSA to maintain flight can be broken into two categories, power to overcome drag (P_d) and power to move the wings (P_m). The movement of the wings consists of the acceleration and deceleration associated with flapping the wing at the desired flapping frequency and through the desired angle of motion. The drag on the vehicle consists of parasite drag, which is the drag associated with the vehicle moving through the air, and the induced drag, the drag generated due to the production of lift. The total power the SSA needs in order to fly is given by Equation 5-17.

$$P_r = P_d + P_m \quad \text{Equation 5-17}$$

The SSA's energy requirements are dependent on the way the vehicle will operate. The operating scheme consists of a wing flap followed by a period of gliding flight. During the wing flap, altitude and velocity will be gained and subsequently lost during the gliding portion of the flight. This flap/glide cycle continues to maintain the SSA near its desired mission altitude. There are two main aspects that define this cycle: the rate at which a flap is performed and the glide time between flaps. These characteristics depend on the lift-to-drag ratio of the SSA and the incident power available. Examples of some of the many potential flap and glide combinations are shown in Figure 5-16. Determining the optimum combination of these characteristics under different flight conditions is a main goal of this analysis.

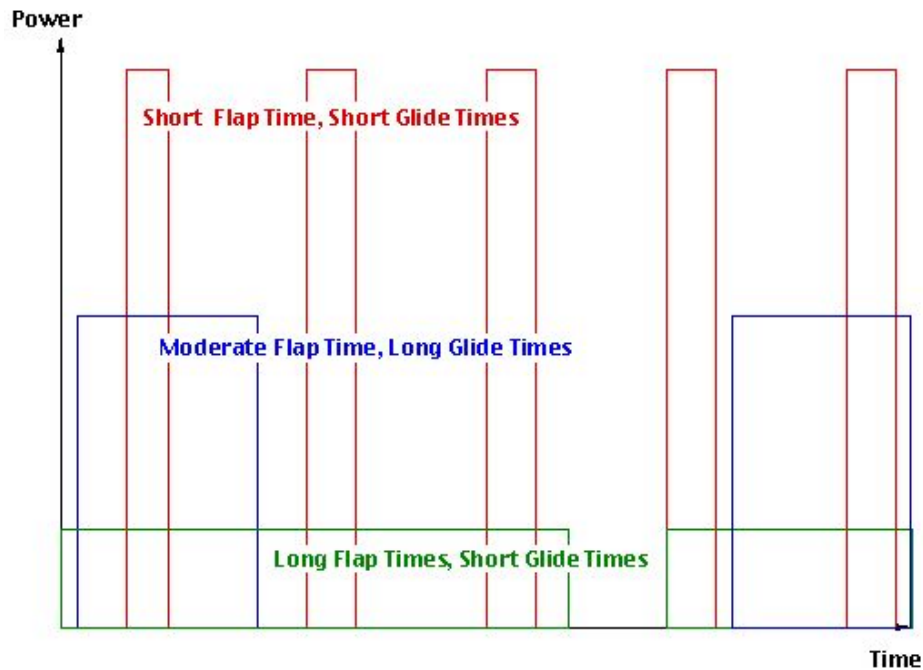


Figure 5-16: Examples of potential flap/glide combinations

The energy consumed during a flap/glide cycle (E) is the continuous power consumed during the flap (P_f) multiplied by the duration of the flap (t_f).

$$E = P_f t_f \quad \text{Equation 5-18}$$

However, because there is a period of time between flaps when no power is consumed, the continuous power level required from the solar arrays (P) is the energy consumed during a flap divided by the total flap time and glide time (t_g) for one complete cycle.

$$P = \frac{E}{t_f + t_g} \quad \text{Equation 5-19}$$

5.2.2.1 Power Required Due to Motion

The movement of the wings is the mechanism for generating thrust for the aircraft. The force and associated power needed to move the wing is therefore a key aspect of vehicle operation. The power required for motion will be much greater than the power to overcome the drag of the vehicle.

The energy required to move the mass of the wing can be easily calculated based on the geometry of the wing, mass distribution along the wing, and the flapping rate. These parameters, including wing length, flapping frequency, and angle through which the wing moves during the flap cycle, are shown in Figure 5-17. They can be varied to optimize the wing design and operation. The optimization consists of maximizing lift while minimizing power required. The loading along the wing due to wing motion is based on the mass distribution along the wing. For this

initial analysis, a rectangular planform was assumed with a uniform distribution of mass along the wing. In a more detailed analysis, the wing geometry can be optimized by varying the taper, chord length, twist, and sweep. The addition of these parameters to the wing design is beyond the scope of this initial Phase I study. These factors will be considered during the detailed design effort conducted under the Phase II portion of the program. The mass distribution and corresponding loading are shown in Figure 5-18.

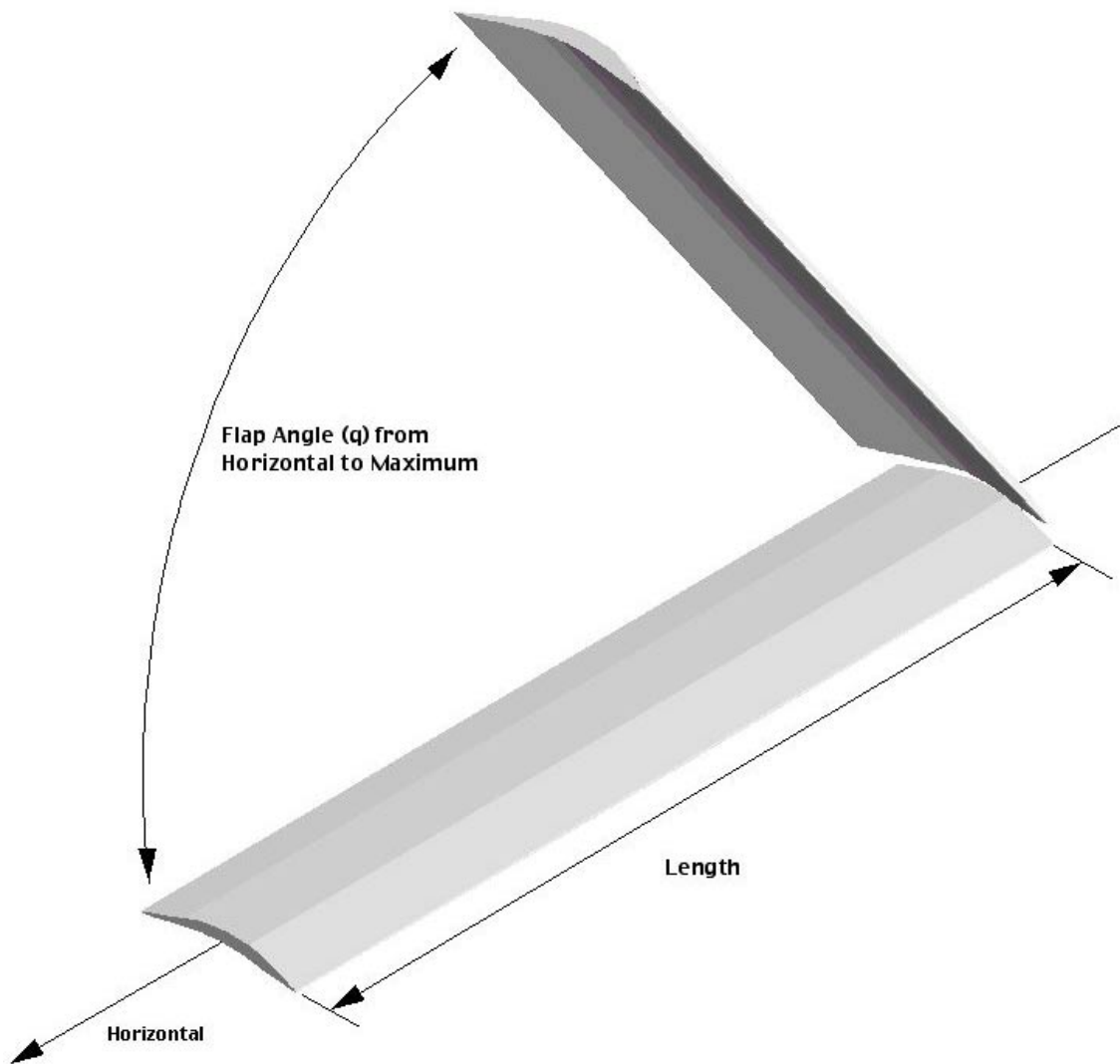


Figure 5-17: Wing motion and geometry

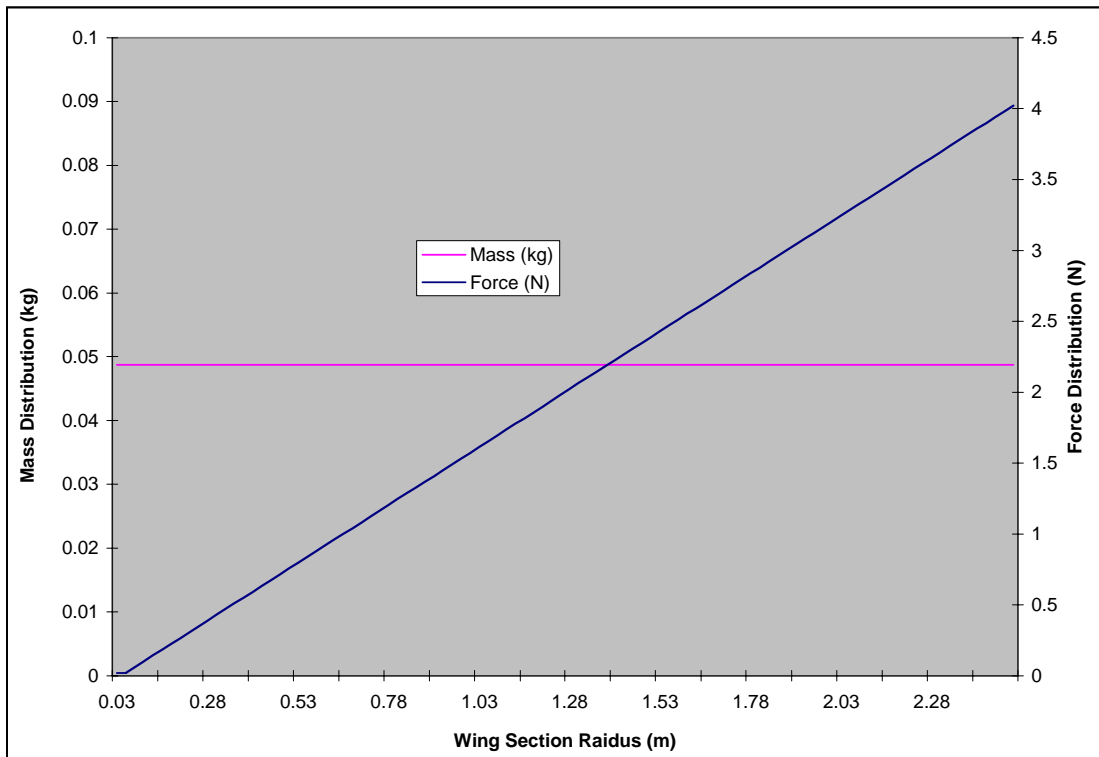


Figure 5-18: Force and mass distribution along a wing section (for a 5-m wingspan and 1 Hz flapping rate)

The wing loading shown in Figure 5-17 is caused by the acceleration of the wing mass; aerodynamic and other loads are not included at this point. The maximum deflection angle and flapping frequency describe the wing motion and are inputs into the analysis. These values can be varied to determine the optimum motion characteristics for the wing for given flight conditions and vehicle size. The wing acceleration was assumed to be a constant from the beginning of the stroke where the wing is in its full upward position, to the wing positioned horizontally. The curves shown in Figure 5-18 show the force and mass distributions for a generic case, not specific to a particular flapping frequency or angle. The curve profiles should be the same for all operating conditions and wing sizes; only the absolute values should be affected by a change in these parameters. As expected, with a uniform and constant mass distribution, the force increases linearly along the wing length from root to tip. The force (F) needed to move one wing section is given by Equation 5-20, where m_i is the mass of an incremental piece of the wing corresponding to a mean radial distance of r_i , θ is the angle through which the wing will move during acceleration, and f is the flapping frequency in cycles per second. Some of these variables are illustrated in Figure 5-19. The wing section is considered to be one-half the wing length (from the center body to the tip). For the entire vehicle the force is twice that given by Equation 5-20.

$$F = \sum_{i=0}^{i=R} m_i \frac{2\theta r_i}{\left(\frac{1}{4f}\right)^2} \quad \text{Equation 5-20}$$

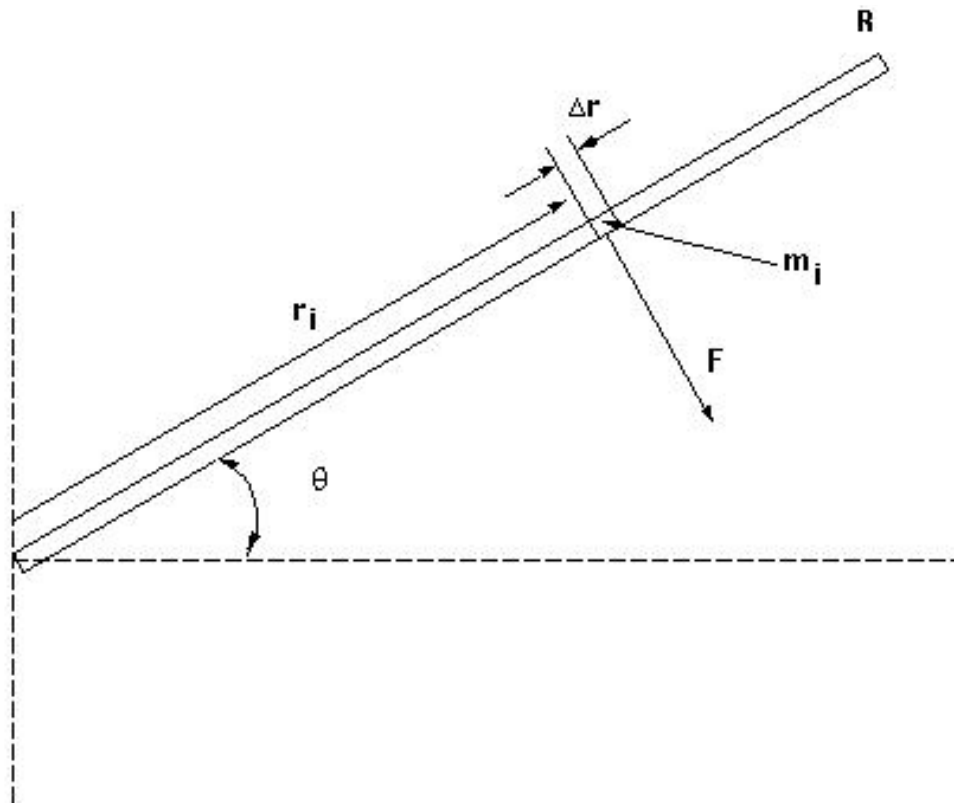


Figure 5-19: Acceleration force diagram

The absolute values associated with the curves given in Figure 5-18 are dependent on the size of the wing, flapping rate, and maximum angle through which the wing will move. The combination of these variables must be optimized to maximize the amount of lift generated by the wing while operating at a power level that can be supplied by the solar array.

The total work performed by the engine to provide the acceleration needed during a flap cycle is given by Equation 5-21.

$$W = 2 \int_0^R F(r) \theta r dr \quad \text{Equation 5-21}$$

The total work performed (or energy consumed), under a given operational condition and wing geometry is the area under the force, distance-traveled curve. Examples are shown in Figure 5-20 for various flapping frequencies, wing lengths, and flapping angle.

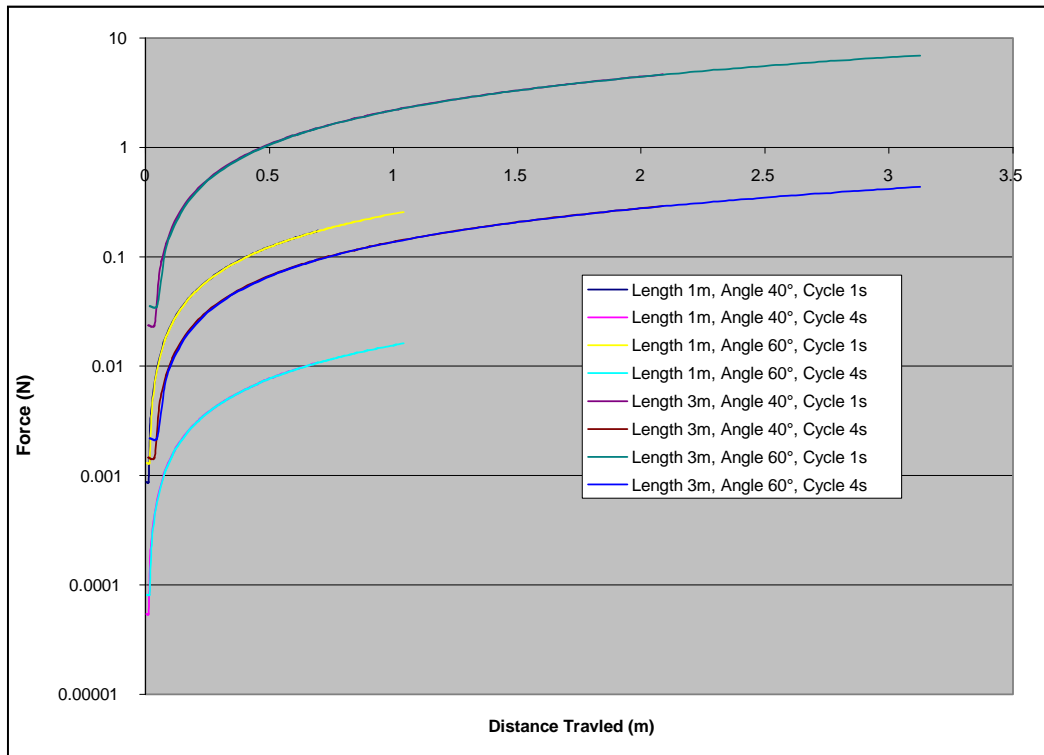


Figure 5-20: Force along the wing as a function of distance traveled by each segment of the wing section

The continuous power consumption (P_r) over the duration of the flap (t_f) is given by Equation 5-22.

$$P_m = \frac{W}{t_f} \quad \text{Equation 5-22}$$

5.2.2.2 Power Required Due to Drag

The drag due to lift generation and flight through the atmosphere is the second power-consuming mechanism considered in this analysis. For any vehicle that flies through the air, there are two main components of drag: parasite drag and induced drag. Parasite drag is produced by the movement of the vehicle through the air. For the thin shape of the SSA, this drag will be mainly due to the surface friction of the air moving over the vehicle surface. The effect of surface friction can be represented by a surface-friction drag coefficient (c_f). Induced drag is produced through the generation of lift. This type of drag results from the generation of vortices by the wing. Induced drag is the main component of drag generated by a surface that generates lift. This drag is also represented by a drag coefficient (c_d). This drag coefficient is related to the amount of lift generated by the wing, as shown in Figure 5-15.

Based on these two types of drag, the total of the SSA's drag during cruise can be represented by Equation 5-23, where S is wing area, ρ is atmospheric density, and V is wing velocity.

$$D = \frac{1}{2} \rho V^2 (c_f 2S + c_d S) \quad \text{Equation 5-23}$$

The atmospheric density will depend on the flight altitude and planetary location in which the SSA is operating. During cruise, the velocity is the flight velocity; however, during a flap the velocity (V_f) is the flight velocity plus a component due to the motion of the wing. Since the wing is moving in an arc, the velocity of each radial station is different and will increase along the wing. The velocity along the wing (V_{fi} at a station i) during a flap is given by Equation 5-24, and the drag during a flap (D_f) is given by Equation 5-25.

$$V_{fi} = \sqrt{V^2 + \frac{4\theta r_i}{t_f}} \quad \text{Equation 5-24}$$

$$D_f = \sum_0^i \frac{1}{2} \rho V_i^2 (c_f 2S + c_d S) \quad \text{Equation 5-25}$$

The total continuous power required during a flap to overcome the drag is given by Equation 5-26.

$$P_d = D_f V \quad \text{Equation 5-26}$$

5.2.3 Lift Generation

The lifting force for the SSA is generated by the flapping of the wings. The lift is generated in a fashion similar to that of an aircraft in which the airflow over the wing causes a pressure difference above and below the wing. This pressure difference produces an upward force, thereby producing lift. However, since the wings of the SSA are moving, unsteady flow phenomena will occur with the SSA, that do not occur with conventional fixed wing flight. A detailed description of the desired wing motion and its effects on airflow over the wing surface and subsequent lift generation are beyond the scope of this Phase I effort. These phenomena will be thoroughly investigated under the Phase II portion of the program. For this analysis, the airflow is assumed to be steady, and lift generation is based on the wing angle of attack and air velocity during the flapping motion.

The lift generated will depend on the angle of attack of the wing, the speed at which the SSA is flying, and the speed of the wing's motion. Based on the wing angle there will be both a horizontal and vertical component to the lift. The horizontal component will need to be large enough to overcome vehicle drag, and the vertical component will need to be greater than the weight of the vehicle to gain altitude for the subsequent glide period. Figure 5-21 shows the lift forces generated during the flapping of the wings.

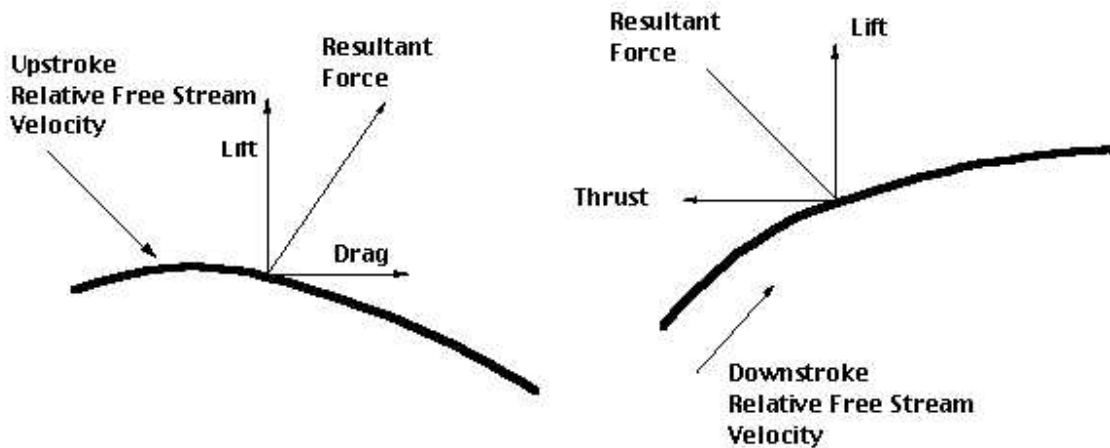


Figure 5-21: Lift force generation due to flapping

The SSA will operate by flapping its wings, gaining altitude and then gliding back to its original altitude, where it flaps its wings again to continue the cycle. This lift cycle is illustrated in Figure 5-22. The gliding portion of the cycle is used to collect energy to be stored for the subsequent flap. As long as sufficient solar energy can be collected during the glide portion to power the flapping motion, the cycle can continue indefinitely. The power-available curves for various operational locations and times are shown in the power-production section. An operational envelope can be established by comparing the power required to generate sufficient lift to maintain the lift/glide cycle, to the available power.

The total lift generated by the wind during the flap is given by Equation 5-27 and shown in Figure 5-23 for various flapping rates. This lifting force is broken into two components: a vertical component (L_y) that produces an upward movement of the vehicle, and a horizontal component (L_x) that produces thrust to overcome vehicle drag. These two components of the lift are given in Equations 5-28 and 5-29. The vertical and horizontal forces generated are dependent on the angle through which the lifting force acts relative to the force of gravity (β). The smaller this angle, the greater the upward lift and the lower the thrust. This angle is controllable by varying the shape and angle of the wing. It can also be controlled as a function of the distance along the wing. For instance, higher angles can be used inboard near the root to generate more thrust along this portion of the wing, and lower angles can be used outboard toward the tip to generate more lift on that portion of the wing. The optimization of the thrust and lift components generated during a flap will be performed during the more detailed design and analysis efforts of the Phase II portion of the program. For this analysis, it is assumed that the angle is constant along the wing length.

$$L = \sum_0^R \frac{1}{2} \rho V_i^2 C_l r_i \quad \text{Equation 5-27}$$

$$L_x = L \sin(\beta) \quad \text{Equation 5-28}$$

$$L_y = L \cos(\beta) \quad \text{Equation 5-29}$$

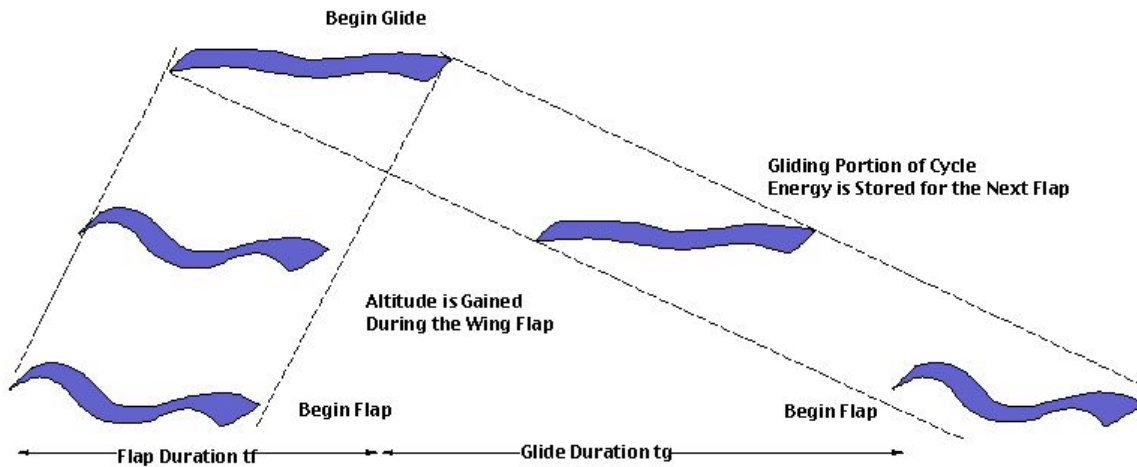


Figure 5-22: Lift/gl glide cycle for the SSA operation

The distance the SSA will move upward (Y) due to a flap of the wings is given by Equation 5-30, where g is the gravitational constant of the planet on which the SSA is flying, W is the total weight of the vehicle, and m is its total mass.

$$Y = \frac{1}{2} t_f^2 \frac{(L_y - W)}{m} \left(\frac{(L_y - W)}{mg} + 1 \right) \quad \text{Equation 5-30}$$

The horizontal distance (X) the vehicle will move while it descends back to its starting altitude is based on its glide slope. The glide slope is dependent on the lift-to-drag value for the SSA. This horizontal distance is given in Equation 5-31.

$$X = Y \frac{C_l}{C_d + 2C_f} \quad \text{Equation 5-31}$$

Using the horizontal distance traveled, X , and the cruise velocity, V , given by Equation 5-32, glide time (t_g) can be calculated. The glide time, given in Equation 5-33, is then used to determine the power level needed from the solar array (Equation 5-19) to maintain flight.

$$V = \sqrt{\frac{2W}{\rho C_l S}} \quad \text{Equation 5-32}$$

$$t_g = \frac{X}{V} \quad \text{Equation 5-33}$$

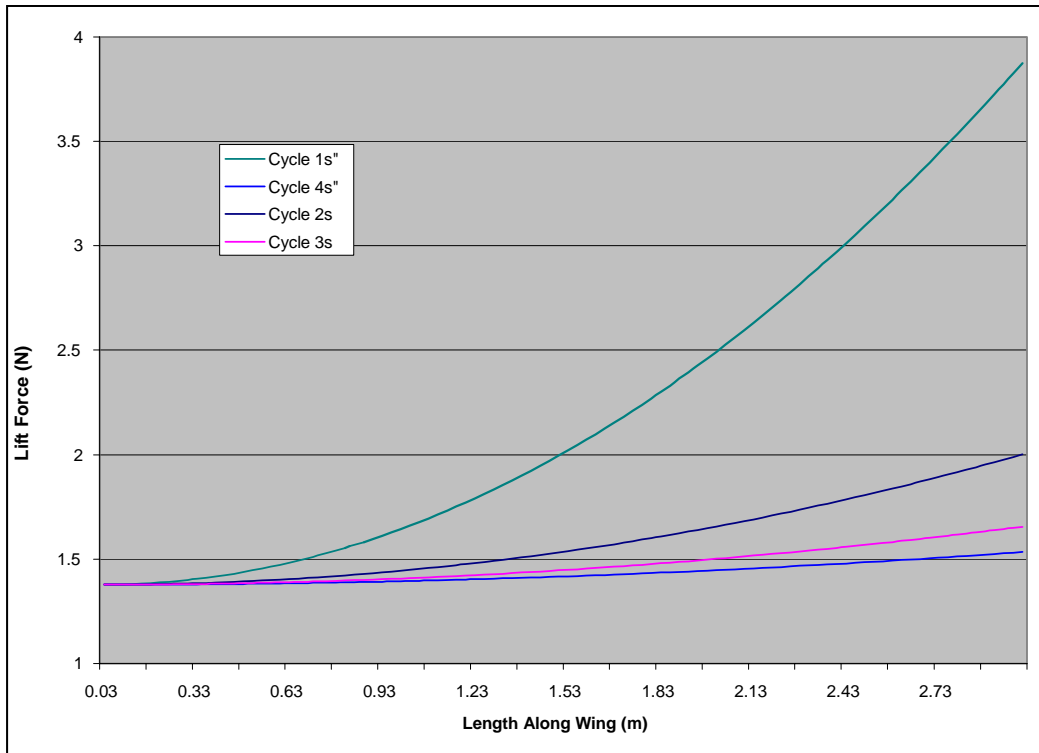


Figure 5-23: Lift force along the wing for various flap rates

5.2.4 Results

The above analysis was used to generate data on the power per square meter required for the SSA to fly under various conditions. The power required was determined for a range of atmospheric densities that correspond to a distinct altitude range for each of the planets of interest (Venus, Earth, and Mars). Also generated by the analysis was the glide time between wing flaps. Several assumptions were used to generate these results, as summarized in Table 5-2. These assumptions represent baseline operating conditions and were used to produce the initial set of results shown in Figures 5-24 through 5-38. As more detail is provided on the operation and layout of the SSA these assumptions will be altered.

Table 5-2: Analysis baseline assumptions

Variable	Value
Maximum wing flap angle	45°
Aspect ratio	8
Wing shape	Rectangular
Solar cell	0.12 kg/m ²
Battery	0.75 kg/m ²
IPMC	2 kg/m ²

Table 5-2: Analysis baseline assumptions (Continued)

Variable	Value
Payload	0.25 kg/m ²

Graphs were generated for power required per square meter as a function of wing area and flap duration for a specific atmospheric density. Graphs were produced over a density range that corresponded to the following altitude ranges for each of the planets of interest:

Table 5-3: Altitude ranges in which results were produced for the various planets

Planet	Altitude Range
Venus	53 km to 82 km
Earth	1 km to 35 km
Mars	1 km to 7 km

For each wingspan at a given altitude, there is a flap duration that produces minimum required power. This flap duration also corresponds to a specific glide time between flaps. This combination of flap duration and glide time is necessary for the SSA to maintain altitude. These two parameters (flap duration and glide duration) set the operational conditions for the aircraft and are selected, for a given altitude, to minimize required power. Required specific power versus flap time is shown in Figures 5-24 through 5-29 for various altitudes and vehicle sizes. For a given altitude and aircraft size, the flap duration needed to minimize power consumption can be selected from these figures. Glide duration between flaps, shown in Figures 5-30 through 5-35, can then be determined. This glide duration establishes the amount of energy that must be stored within the battery between each flap.

From these figures it can be seen that reducing the flapping rate minimizes power consumption. This can be achieved up to the point where the glide time is zero. Beyond this point power required will begin to increase again. The reduction in glide time also reduces the amount of energy storage needed of the batteries. This energy-storage requirement goes to zero as glide time goes to zero.

The minimum power-required point for each altitude-wingspan combination is plotted in Figure 5-36 as a function of Earth altitude. The corresponding flap durations and glide times for this minimum power point are plotted in Figures 5-37 and 5-38, respectively. As the glide duration goes to zero, the required battery capacity goes to zero.

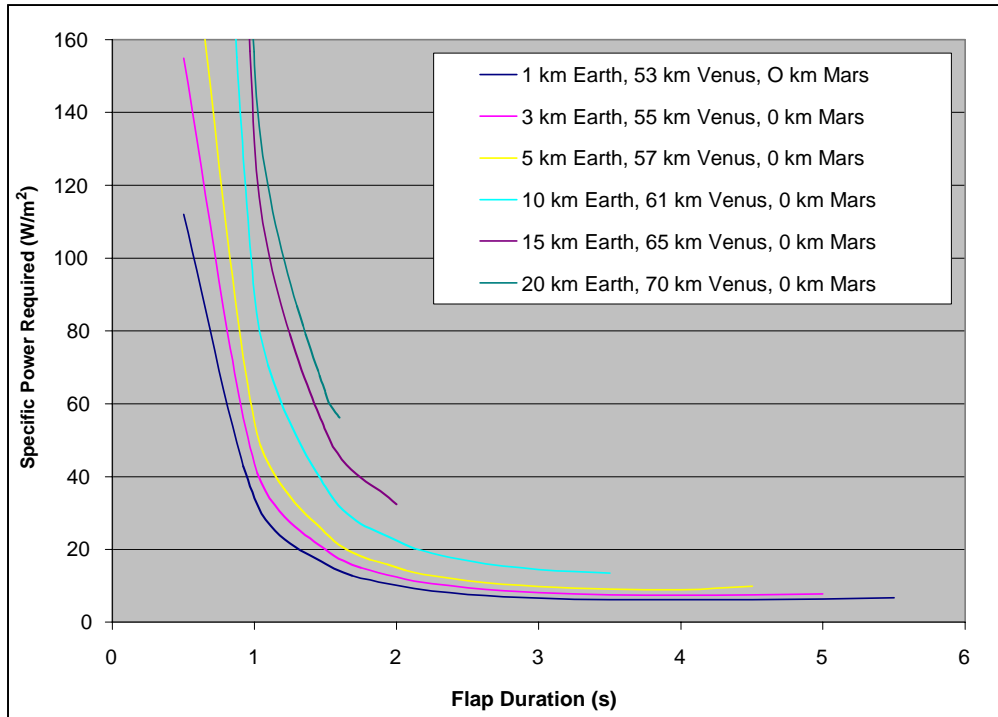


Figure 5-24: Specific power vs. flap duration for a 3-m wingspan vehicle at various altitudes

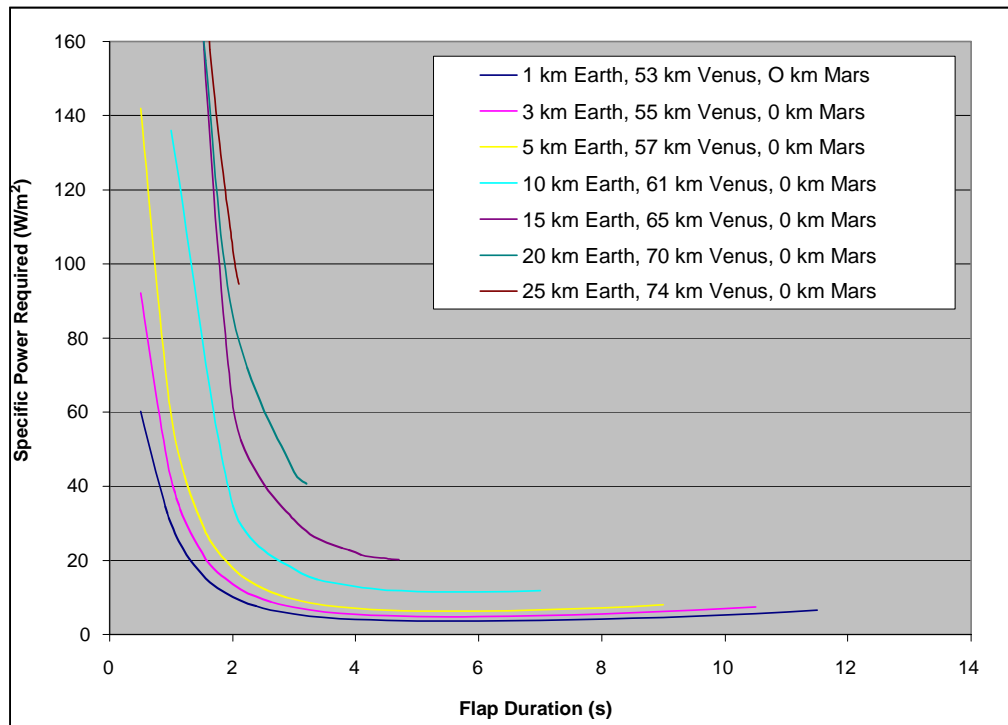


Figure 5-25: Specific power vs. flap duration for a 6-m wingspan vehicle at various altitudes

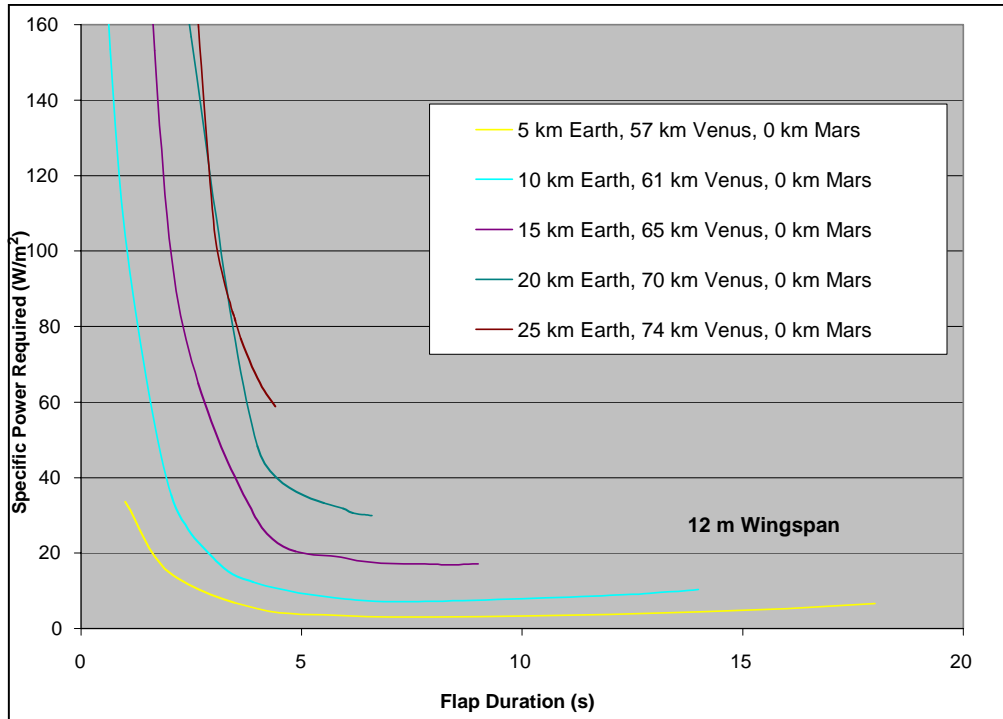


Figure 5-26: Specific power vs. flap duration for a 12-m wingspan vehicle at various altitudes

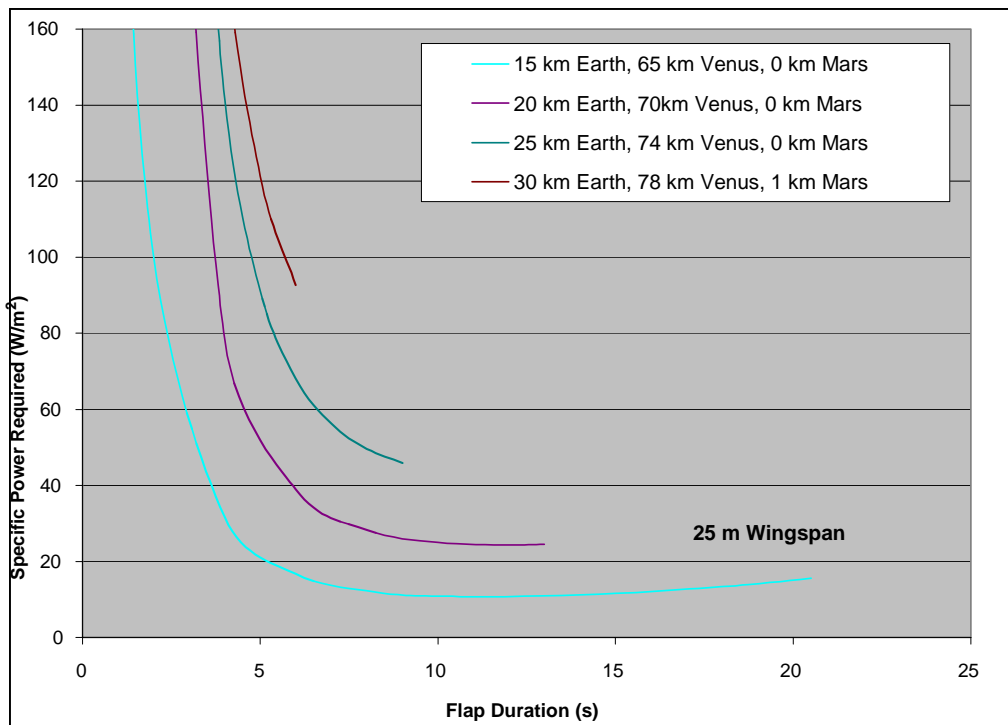


Figure 5-27: Specific power vs. flap duration for a 25-m wingspan vehicle at various altitudes

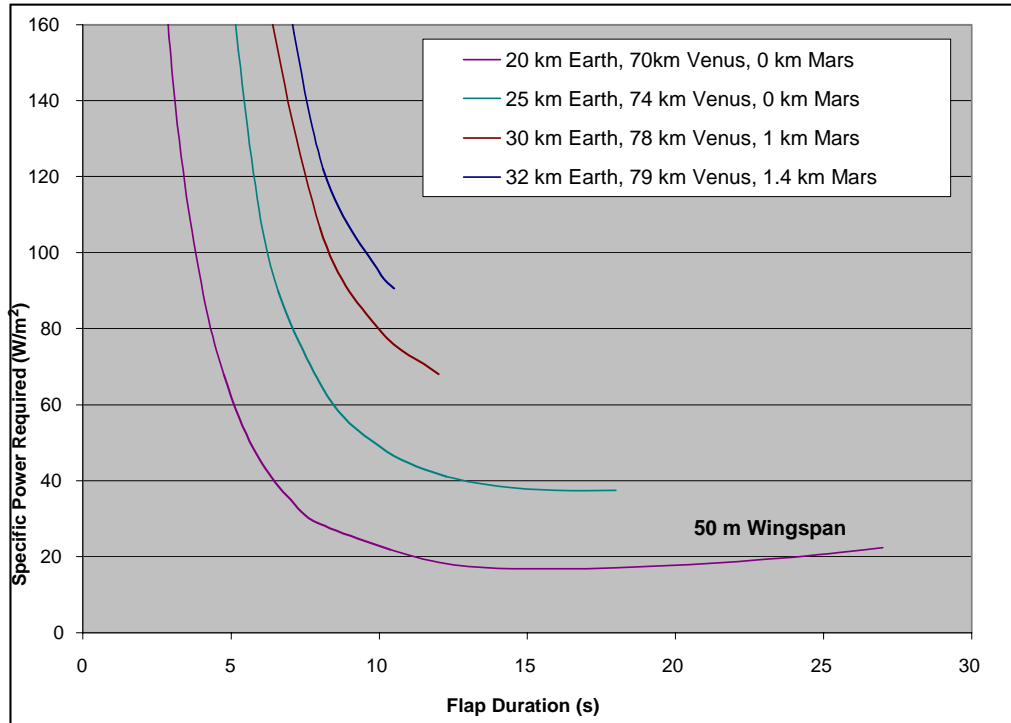


Figure 5-28: Specific power vs. flap duration for a 50-m wingspan vehicle at various altitudes

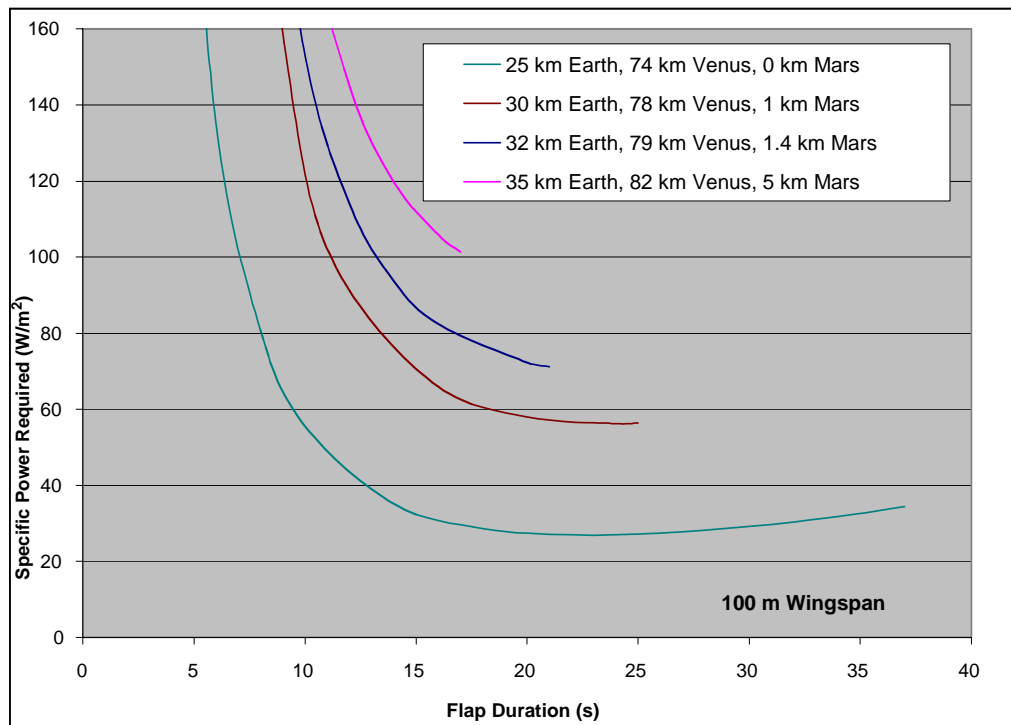


Figure 5-29: Specific power vs. flap duration for a 100-m wingspan vehicle at various altitudes

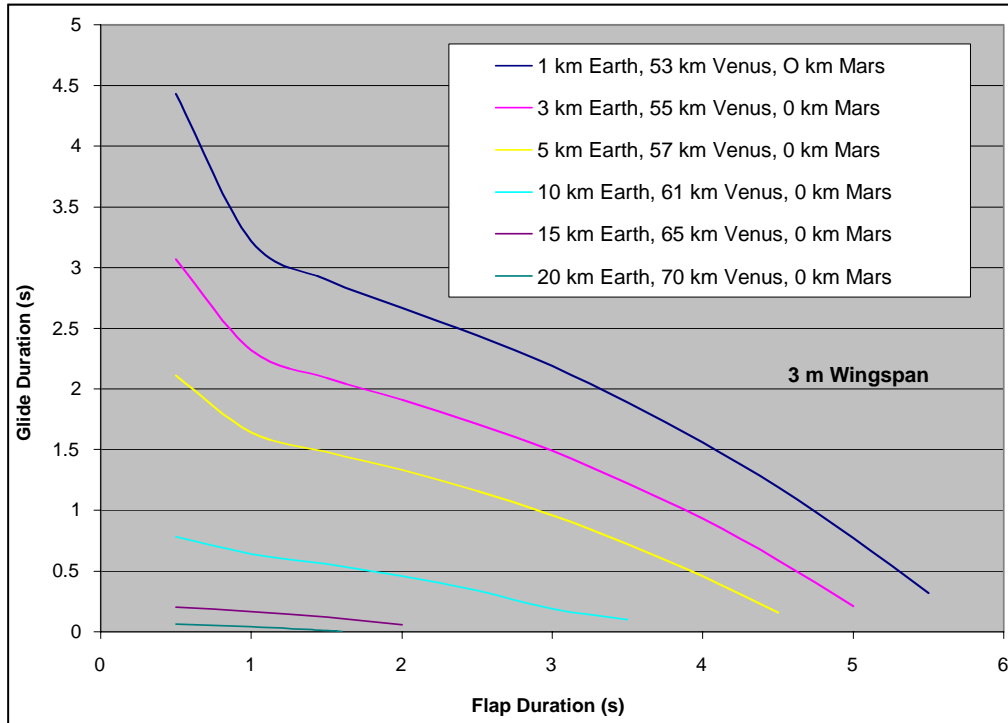


Figure 5-30: Glide duration vs. flap duration for a 3-m wingspan vehicle at various altitudes

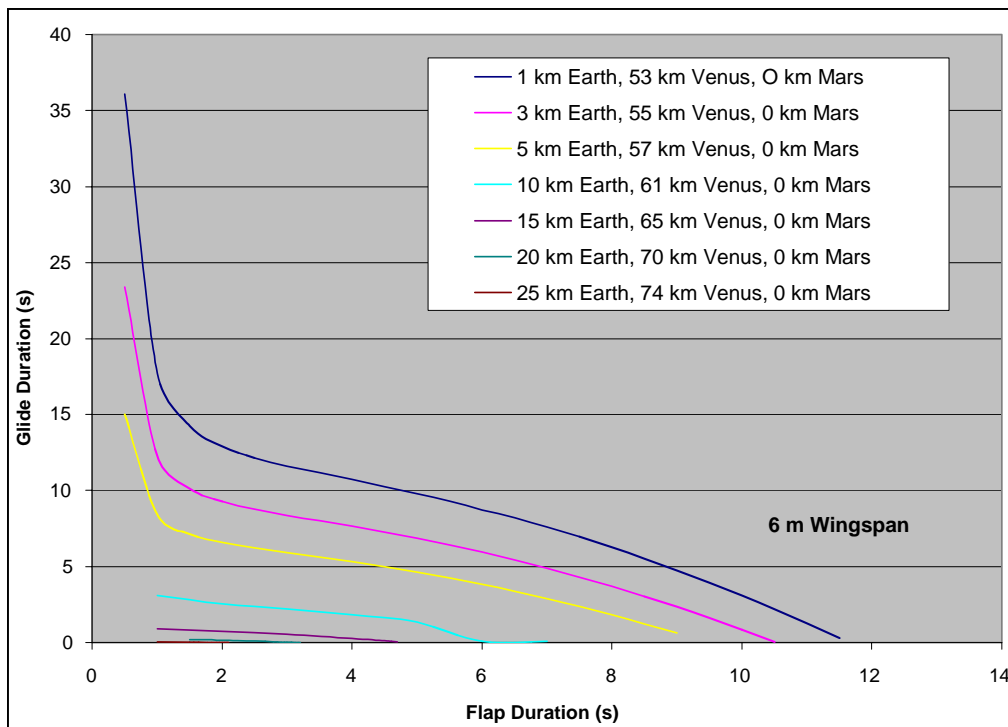


Figure 5-31: Glide duration vs. flap duration for a 6-m wingspan vehicle at various altitudes

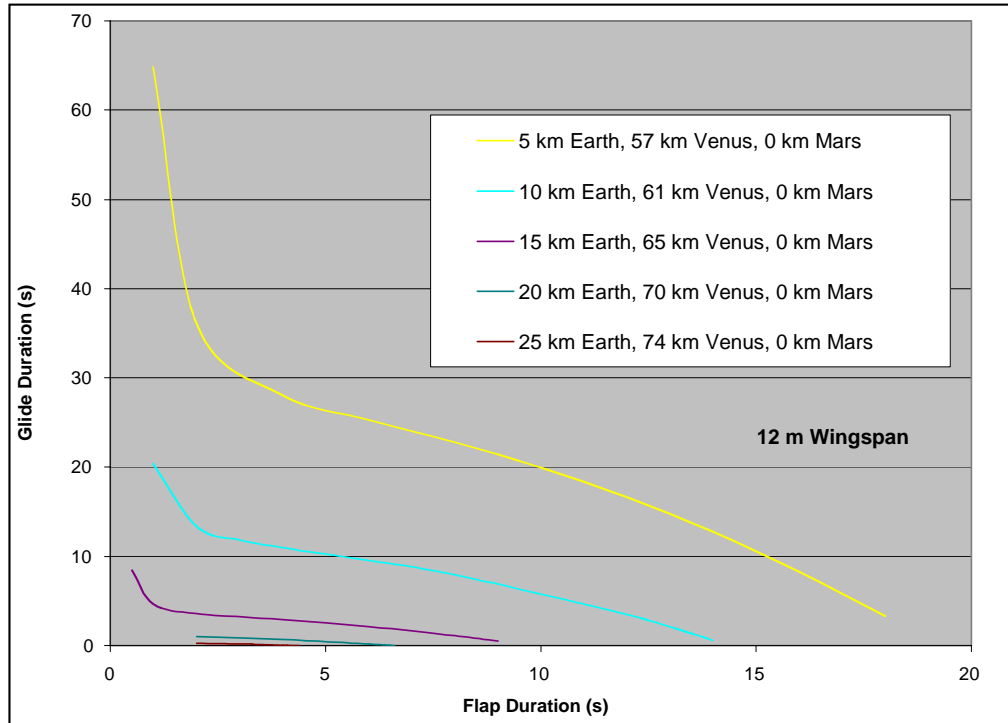


Figure 5-32: Glide duration vs. flap duration for a 12-m wingspan vehicle at various altitudes

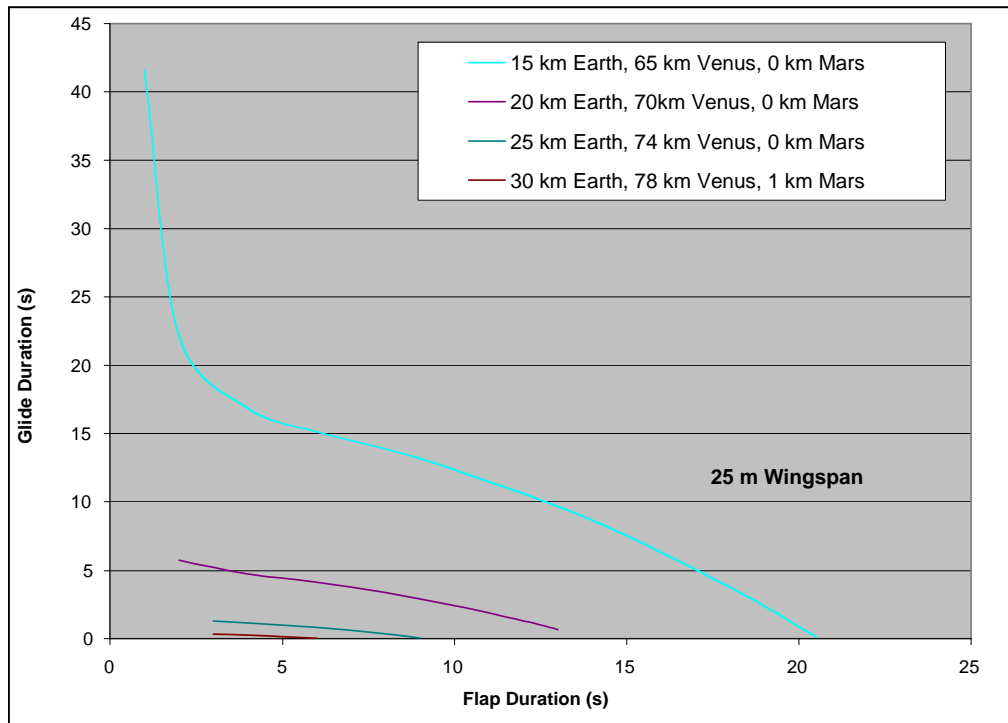


Figure 5-33: Glide duration vs. flap duration for a 25-m wingspan vehicle at various altitudes

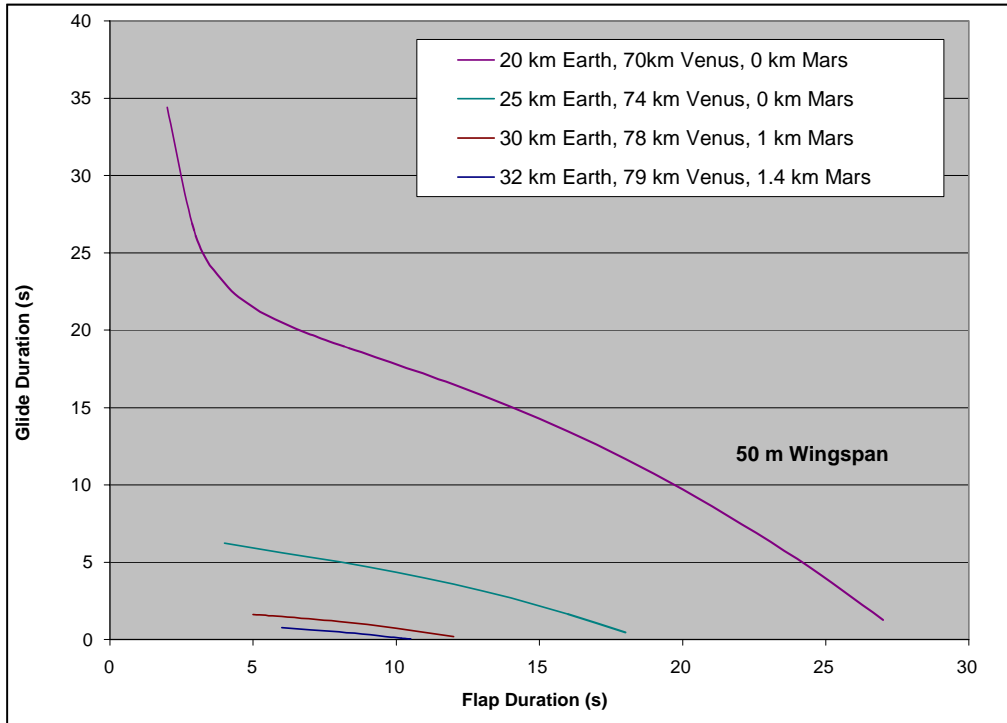


Figure 5-34: Glide duration vs. flap duration for a 50-m wingspan vehicle at various altitudes

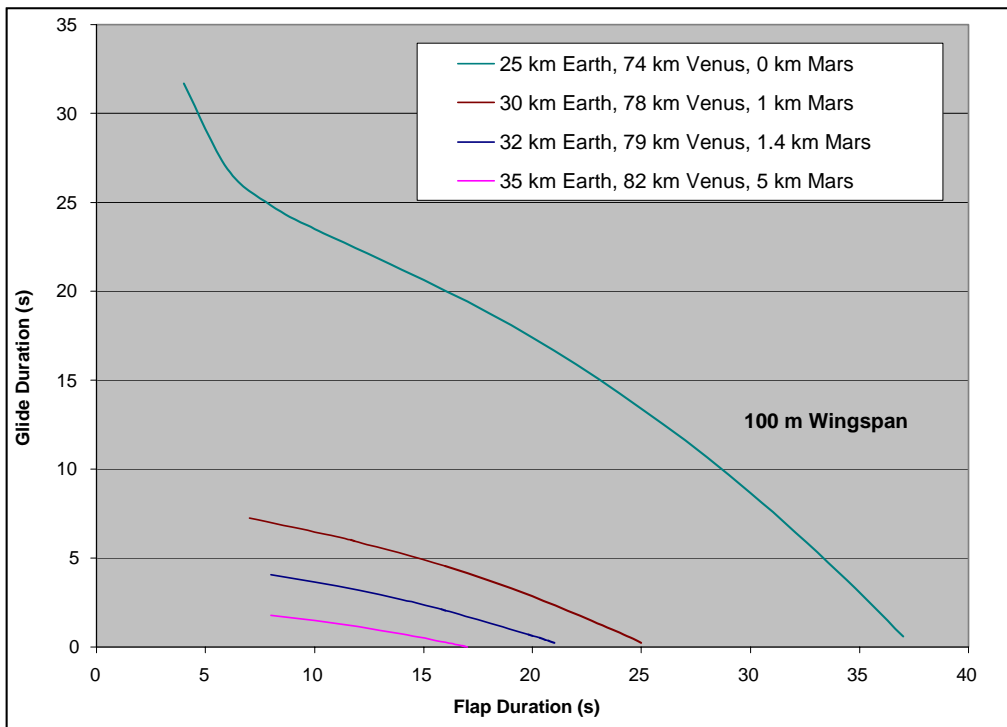


Figure 5-35: Glide duration vs. flap duration for a 100-m wingspan vehicle at various altitudes

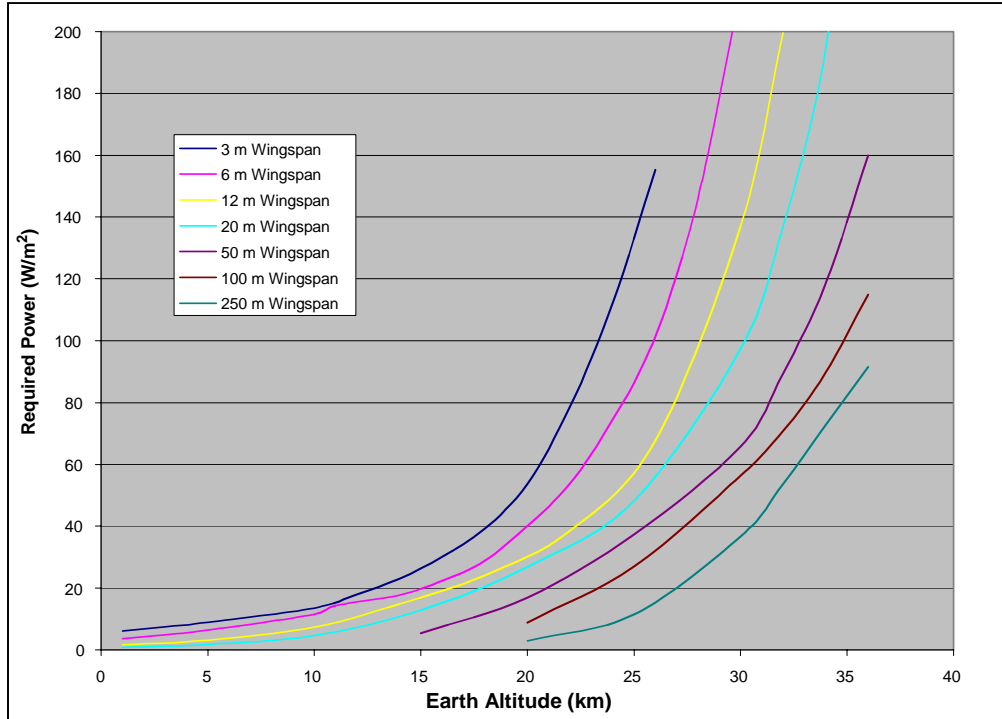


Figure 5-36: Minimum required power for various altitude-wingspan combinations

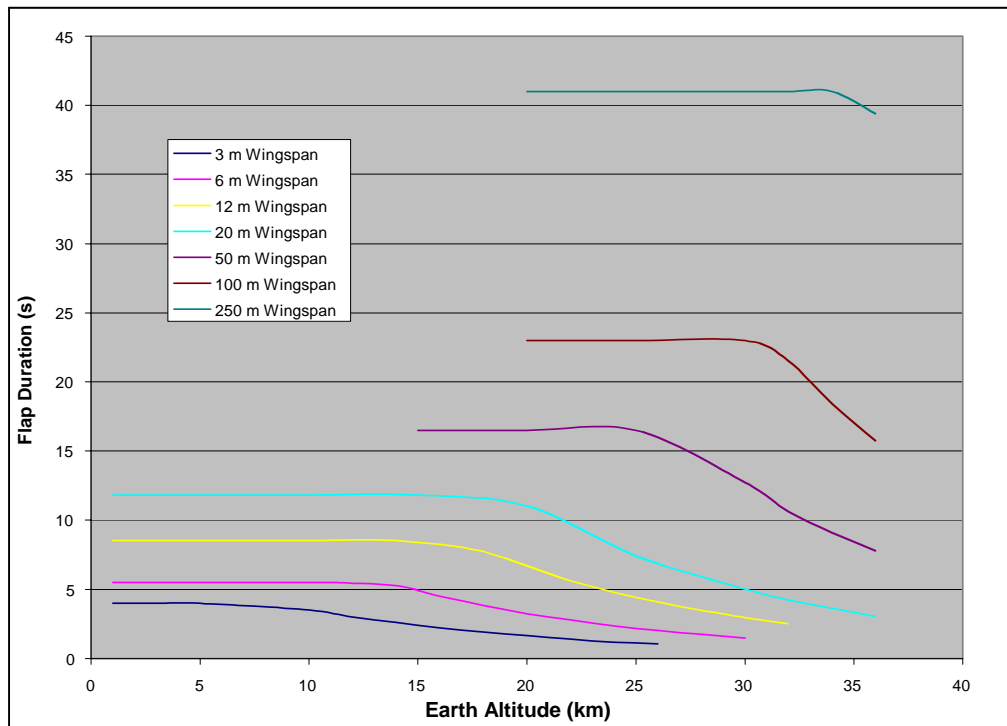


Figure 5-37: Flap duration for minimum required power at various altitudes and wingspans

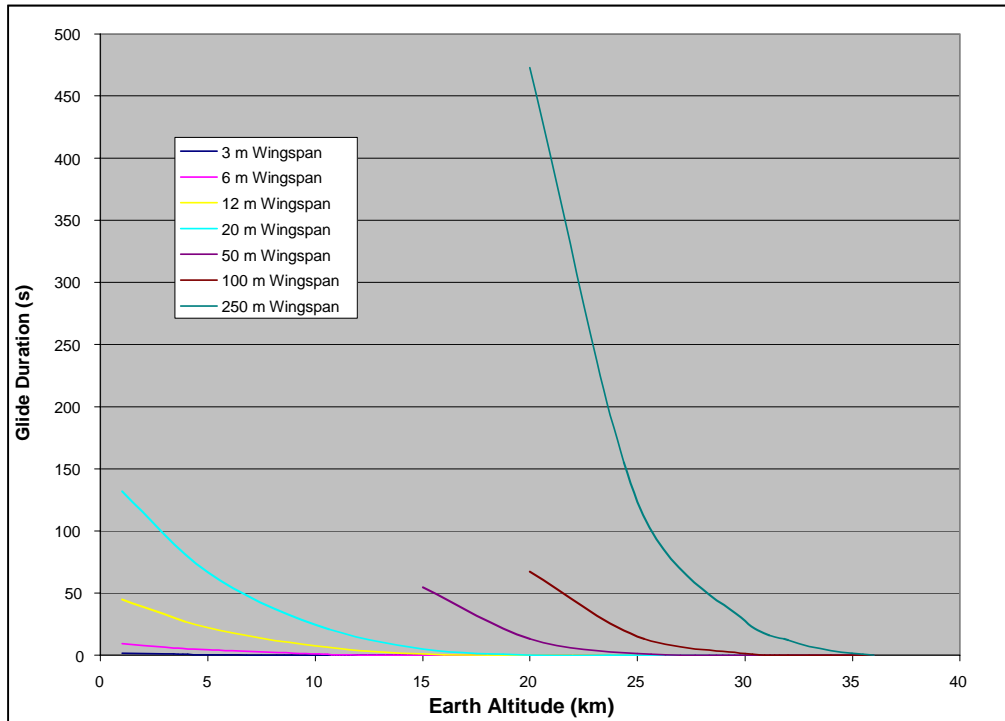


Figure 5-38: Glide duration for minimum required power at various altitudes and wingspans

Through this analysis, it was determined that the SSA has a fairly large range of operation. These results are summarized in Figure 5-39, which shows the maximum available power at each planetary location, and the required power for various sized SSAs. The required power is plotted as a function of altitude for each planet. This figure demonstrates that there is quite a significant range of vehicle sizes that could operate within the Venus and Earth environments. Sizes below the maximum power lines can operate on the planet at the corresponding altitude given along the X axis. For Mars, the SSA would have to be of significant size, on the order of a few hundred meters in length.

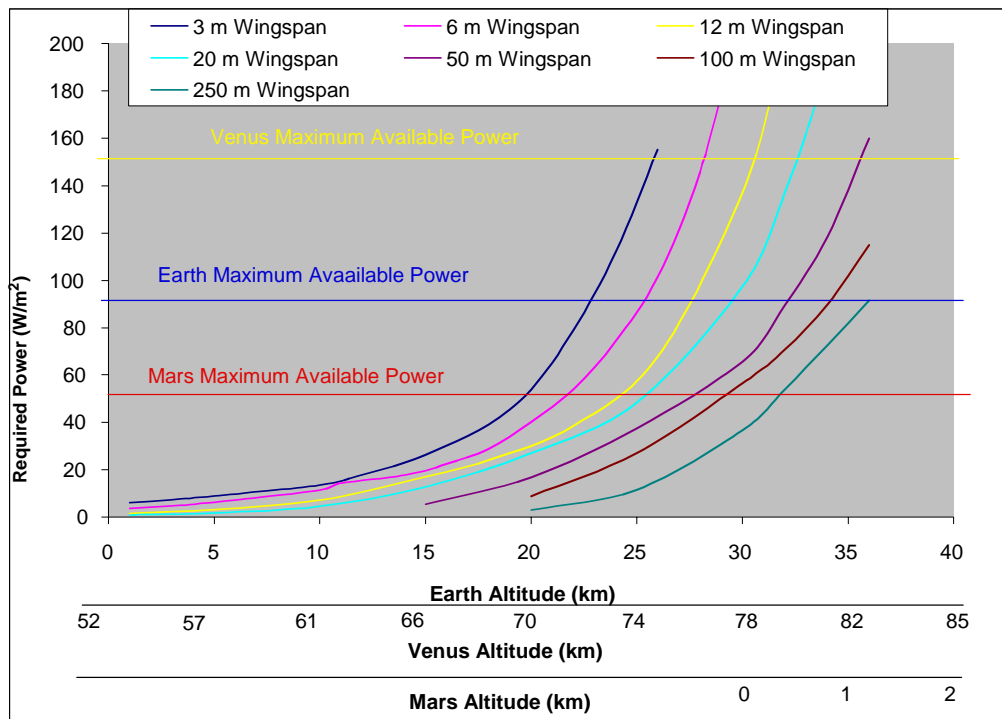


Figure 5-39: Power required and maximum available power at each planetary location

5.3 Example Design

The preceding sections map a parameter space for operating the SSA. Also considered in previous sections is the power available on various planets, at different latitudes and different seasons. It seems instructive at this point to consider a particular SSA configuration and compare power requirements with the power produced for a given mission to see if flight is feasible. Considered here is an SSA with a 100-m wingspan designed to fly at 25 km on Earth, on the equator during the summer, flying for a minimum of 8 hours. This design was chosen because it has the lowest power requirements and the greatest power available for a mission that could fly on Venus, Earth, or Mars. On Mars the flight altitude would be near the surface, and on Venus it would fly at 74 km.

The SSA described above requires 30 W/m^2 to maintain flight. On Earth and Mars, the solar arrays could produce in excess of 30 W/m^2 for approximately 8 hours. In both cases, there is excess power available during the 8-hour period that could be used to extend the mission past the 8-hour design. However, the excess power on Earth is considerably higher than on Mars, and the SSA could therefore stay in the air longer than the same aircraft on Mars. On Venus, the same SSA would have considerably more power available than on Earth. Even if we assume that the SSA would be carried by the high altitude winds of Venus, the power available would exceed 30 W/m^2 for nearly 24 hours. This example demonstrates that, even with current technology, it is feasible to power an SSA, for flight on Venus, Earth, or Mars.

Appendix A: List of References

1. Asada, A.; Oguro, K.; Nishimura, Y.; Misuhata, M.; and Takenaka, H., "Bending of Poly-electrolyte Membrane-Platinum Composites by Electric Stimuli, I. Response Characteristics to Various Wave Forms," *Polymer Journal*, 27, pp. 436-440, 1995.
2. Brawn, Robert (supplied by), NASA Langley Research Center for the Mars Aircraft Micor-mission Program, March, 1999.
3. Cruz, J., "Mars Dust Storms," Mars Airplane Package Document 0807-03-01A. October, 1999.
4. Cruz, J., Taylor, G., "Mars Airplane Package, Preliminary Baseline Mission Sites," Docu-ment 0867-02-01A, October, 1999.
5. de Gennes, P. G.; Okumura, K.; Shahinpoor, M.; and Kim, K. J., "Mechanoelectric Effects in Ionic Gels," *Europhysics Letters*, 50(4), pp. 513-518, 2000.
6. *Handbook of Tables for Applied Engineering Science*, 2nd edition, CRC Press, 1973.
7. Kerzhanovich, Victor V., personal correspondence, JPL, January 2000.
8. Landis, G. A.; Colozza, A.; and LaMarre, M. C., "Atmospheric Flight on Venus," NASA TM 2002-211467, June 2002.
9. McCormick, B. W., *Aerodynamics, Aeronautics and Flight Mechanics*, John Wiley & Sons, 1979.
10. Millet, P.; Pineri, M.; and Durand, R., "New Solid Polymer Electrolyte Composites for Water Electrolysis," *Journal of Applied Electrochemistry*, 19, pp. 162-166, 1989.
11. Oguro, K.; Asaka, K.; and Takenaka, H., "Actuator Element," U.S. Patent #5,268,082, 1993.
12. *Online Journey Through Astronomy*, Brooks/Cole Thompson Learning, <http://csep10.phys.utk.edu>, July, 2002.
13. Raymer, D. P., *Aircraft Design: A Conceptual Approach*, AIAA Educational Series, 1989.
14. Schofield, J. T.; Barnes, J. R.; Crisp, D.; Haberle, R. M.; Larsen, S.; Magalhaes, J. A.; Mur-phy, J. R.; Seiff, A., and Wilson, G., "The Mars Pathfinder Atmospheric Structuer Investiga-tion/Meteorology (ASI/MET) Experiment".
15. Shahinpoor, M.; Adolf, D.; Segalman, D.; and Witkowski, W., "Electrically Controlled Polymeric Gel Actuators," U.S. Patent #5,250,167, 1993.
16. Shahinpoor, M.; Bar-Cohen, M.; Simpon, J. O.; and Smith, J., "Ionic Polymer Metal Com-posites (IPMC) as Biomimetic Sensors and Structures: A Review," *Smart Materials and Structures*, 7, pp. 15-30, 1998.
17. Shahinpoor, M.; and Kim, K. J., "Ionic Polymer Metal Composites – I. Fundamentals," *Smart Materials and Structures Int. J.*, Vol. 10, pp. 819-833, 2001.
18. Shahinpoor, M.; and Kim, K. J., "Novel Ionic Polymer-Metal Composites Equipped with Physically-Loaded Particulate Electrode As Biomimetic Sensors, Actuators and Artificial Muscles," *Actuators and Sensors A, Physical*, A, 3163, pp. 1-8, 2002.
19. Shahinpoor, M.; and Kim, K. J., "The Effect of Surface-Electrode Resistance on the Perfor-mance of Ionic Polymer Metal Composites (IPMC) Artificial Muscles, *Smart Materials and Structures*, vol. 9, pp. 543-551, 2000.
20. Shahinpoor, M.; and Mojarrad, M., "Soft Actuators and Artificial Muscles," U.S. Patent, #6,109,852, 2000.

21. Shahinpoor, M.; Norris, I. D.; Mattes, B. R.; Kim, K. J.; and Sillerud, L. O., "Electroactive Polyacrylonitrile Nanofibers as Artificial Nano-Muscles," Proceedings of the 2002 SPIE Conference on Smart Materials and Structures, vol. 4695, No. 42, pp. 169-173, March 2002.
22. Space and Planetary Environment Criteria Guidelines for Use In Space Vehicle Development, 1982 Revision (Volume 1), NASA TM- 82478, January, 1983.
23. Strganac, T.W.; "Wind Study for High Altitude Platform Design," NASA Reference Publication 1044, December 1979.
24. Takenaka, H.; Torikai, E.; Kwami, Y.; and Wakabayshi, N., "Solid Polymer Electrolyte Water Electrolysis," *International Journal of Hydrogen Energy*, 7, pp. 397-403, 1982.
25. Von Mises, R., "Theory of Flight", Dover Publications, Inc., New York, 1959.
26. Windows to the Universe, at <http://www.windows.ucar.edu/>, University Corporation for Atmospheric Research, July 2002.